Cardiac fibroblast phenotype regulation in engineered connective tissues with a special focus on ER adaptation and stress

Doctoral thesis

In partial fulfillment of the requirements for the degree
"Doctor rerum naturalium (Dr.rer.nat.)"

within the Cardiovascular Science doctoral program
of the Georg-August University School of Science (GAUSS)
at the Georg-August University Göttingen

submitted by

Alisa Nicole DeGrave

born in Texas, USA

Göttingen, 2022

Thesis Committee Members (Examination Board)

First Reviewer:

Prof. Dr. Susanne Lutz

Institute of Pharmacology and Toxicology

University Medical Center, Georg-August University Göttingen

Robert-Koch-Straße 40, 37075 Göttingen

☏ +49 (0) 551 39 10665

susanne.lutz@med.uni-goettingen.de

Second Reviewer:

Prof. Dr. Ivan Bogeski

Institute of Cardiovascular Physiology

University Medical Center, Georg-August University Göttingen

Humboldtallee 23, 37073 Göttingen

☏ +49 (0) 551 39 65520

ivan.bogeski@med.uni-goettingen.de

Prof. Dr. med. Michael Zeisberg

Clinic for Nephrology and Rheumatology

University Medical Center, Georg-August University Göttingen

Robert-Koch-Straße 40, 37075 Göttingen

☏ +49 (0) 551 39 60400

michael.zeisberg@med.uni-goettingen.de

Extended Thesis Committee Members (Examination Board)

Prof. Dr. Ralf Dressel

Institute of Cellular and Molecular Immunology

University Medical Center, Georg-August University Göttingen

Humboldtallee 34, 37073 Göttingen

☏ +49 (0) 551 395884

rdresse@gwdg.de

Prof. Dr. mult. Thomas Meyer

Clinic for Molecular Psycho-Cardiology

University Medical Center, Georg-August University Göttingen

Waldweg 33, 37075 Göttingen

☏ +49 (0) 551 394940

thomas.meyer@med.uni-goettingen.de

Prof. Dr. Tiago F. Outeiro

Institute of Experimental Neurodegeneration

University Medical Center, Georg-August University Göttingen

Waldweg 33, 37075 Göttingen

☏ +49 (0) 551 3913544

tiago.outeiro@med.uni-goettingen.de

Date of Disputation: December 15, 2022

Affidavit

I hereby declare that the present thesis entitled “Cardiac fibroblast phenotype regulation in engineered connective tissues with a special focus on ER adaptation and stress” was independently written. Information gathered from other works according to wording or meaning has been indicated in every single case by the declaration of the source. Furthermore, I hereby state that I have produced my work according to the principles of good scientific practice in compliance with the valid “Richtlinien der Georg-August Universität Göttingen zur Sicherung guter wissenschaftlicher Praxis.”

Alisa N. DeGrave

Göttingen, November 10, 2022

List of Publications

Santos GL, Meyer T, Tiburcy M, **DeGrave A**, Zimmermann WH, and Lutz S (2021). Fibroblast Derived Human Engineered Connective Tissue for Screening Applications. *Journal of Visualized Experiments*, DOI: 10.3791/62700.

Santos GL* & **DeGrave AN***, Rehman A, Al Disi S, Xhaxho K, Schröder H, Bao G, Meyer T, Tiburcy M, Dworatzek E, Zimmermann WH, Lutz S (2022). Using different geometries to modulate the cardiac fibroblast phenotype and the biomechanical properties of engineered connective tissues. *Biomaterials Advances*, DOI: 10.1016/j.bioadv.2022.213041.
*shared first authorship

List of Oral Presentations

DeGrave A, Al Disi S, Weinbrenner S, Maestro Lavin D, Santos GL, and Lutz S. Cardiac fibroblasts follow their individual program in 3D cultures. 6th German Pharm-Tox Summit (GPTS) 2021, virtual.

DeGrave A, Doan T, Weinbrenner S, and Lutz S. Collagen expression in human cardiac fibroblasts is closely regulated by the unfolded protein response mediator PERK. 7th German Pharm-Tox Summit (DGPT) 2022, virtual.

List of Poster Presentations

DeGrave A, Santos GL, Schröder H, and Lutz S. Enhanced environmental stress augments the protein folding machinery in human cardiac fibroblasts. 5th German Pharm-Tox Summit (GPTS) 2020, Leipzig, Germany.

DeGrave A, Santos GL, Al Disi S, Weinbrenner S, and Lutz S. The heterogeneity of human healthy diseased commercial human cardiac fibroblasts in 2D and 3D cultures: Linked relationships and non-related parameters. 88th Annual Meeting of the German Society of Cardiology (DGK), Mannheim 2022, Germany.

Acknowledgments

It is a glorious yet surreal feeling to finally have the privilege to acknowledge and thank every individual who helped me complete my doctoral thesis, all to whom I owe this success.

First and foremost, I would like to thank Prof. Dr. Susanne Lutz for seeing my potential as a Master's student in the Cardiovascular Science program. Your scientific curiosity and ability to tackle challenges have genuinely inspired me over the years. Not only did you patiently guide me to learn how to critically think, but you also selflessly dedicated time and effort to encourage me to be my best in all stages of this process, and I am indescribably appreciative.

To my colleagues in the Lutz working group - Gabriela, Abdul, Thao, Bastian, Sarah, and Sophie - I would like to extend my appreciation for your unwavering support, both scientifically and personally, as we grew to be friends over the years.

To Prof. Dr. Ivan Bogeski and Prof. Dr. med. Michael Zeisberg, you both have my sincerest appreciation for dedicating your valuable time to serving on my thesis advisory committee.

This thesis would not have been possible without the International Research Training Group (IRTG) 1816, funded by the Deutsche Forschungsgemeinschaft, and the continuous administrative/academic coordination support provided by Dr. Christina M. Würtz, Fulya M. Ören, and Ulrike Fischer.

I also want to thank Prof. Dr. Wolfram-Hubertus Zimmermann for his leadership as the Institute of Pharmacology & Toxicology Director and every technician that helped me along the way. Of course, a thank you to all my colleagues in other working groups in the Institute of Pharmacology & Toxicology for showing me that work and fun can be mixed.

To my loving family, with every decision I have made throughout my life, you all have always been supportive, even when that meant I would be (very) far from home. Thank you so much for your support and love. To my friends, or should I say to my second family, you know who you are. Thank you for helping me "keep my eyes open" and reminding me to enjoy this phase of my life, regardless of the pressure and expectations.

Finally, I would like to express my utmost gratitude for Philo. Thank you for holding my hand through the good and the bad days. For being my soundboard and accepting that I do not always need you to fix something, but I need an open ear. Your constant encouragement pushed me through self-doubt and helped me realize that, indeed, I (we) can do this.

Table of Contents

List of Figures

List of Tables

List of Abbreviations

%	Percent
°C	Degree Celsius
α	Alpha
α-SMA	Alpha smooth muscle actin
Abbrev.	Abbreviation
ACTA2	Actin alpha 2, smooth muscle
ATF4	Activating transcription factor 4
ATF6	Activating transcription factor 6
AMG'44	AMG PERK 44
Ang II	Angiotensin II
APS	Ammonium persulfate
ATP	Adenosine triphosphate
β	Beta
Bcl-2	B-cell lymphoma-2
BiP	Binding immunoglobulin protein
Cilp	Cartilage intermediate layer protein
CCDC80	Coiled-coil domain containing 80
CD90	Cluster of differentiation 90 (*THY1*)
cDNA	Complimentary deoxyribonucleic acid
CF	Cardiac fibroblast
CHOP	CCAAT/-enhancer binding protein homologous protein
CO_2	Carbon dioxide
COL1A1	Collagen type I, alpha 1
COL3A1	Collagen type III, alpha 1
CSA	Cross-sectional area
Ct	Cycle threshold
CTGF	Connective tissue growth factor
CVD	Cardiovascular disease
DAPI	4', 6-diamidino-2-phenylindole dihydrochloride
DCM	Dilated cardiomyopathy
ddH_2O	Double distilled water
DCN	Decorin
DDIT3	DNA damage-inducible transcript 3 (CHOP)

DEG	Differentially expressed genes
DMEM	Dulbecco's modified eagle's medium
DMSO	Dimethyl sulfoxide
DNA	Deoxyribonucleic acid
DNAJB9	DnaJ heat shock protein family (Hsp40) subfamily B member 9
dNTP	Deoxyribonucleoside triphosphate
DPBS	Dulbecco's phosphate buffered saline
ECM	Extracellular matrix
ECT	Engineered connective tissue
EDTA	Ethylenediaminetetraacetic
eIF2α	Eukaryotic translation initiation factor 2 alpha
EIF2AK3	Eukaryotic translation initiation factor 2 alpha kinase 3
ER	Endoplasmic reticulum
ERAD	ER-associated protein degradation system
et al.	Latin: et alii/et aliae/et alia, "and others"
EtOH	Ethanol
F-actin	Filamentous actin
FAP	Fibroblast activation protein
FBS	Fetal bovine serum
FCS	Fetal calf serum
FDR	False discovery rate
F NF1	Female Normal Fibroblast 1
F NF2	Female Normal Fibroblast 2
F NF3	Female Normal Fibroblast 3
FGM-3	Fibroblast Growth Medium 3 with supplements
Fw	Forward primer
g	Gram
G-actin	Globular actin
GADD34	Growth arrest and DNA damage-inducible gene 34
GAPDH	Glyceraldehyde-3-phosphate dehydrogenase
GO	Gene ontology
GPCR	G-protein-coupled receptor
GSK'157	GSK-2656157
GTP	Guanosine triphosphate

GTPase	Guanine nucleotide-binding protein
GUSB	β-glucuronidase
h	Hour
hCF	Human cardiac fibroblast
HCl	Hydrochloric acid
HF	Heat failure
HK	Housekeeping
Hsp	Heat shock protein
HSP90B1	Heat shock protein 90 beta family member 1
HSPA1A	Heat shock protein family A (Hsp70) member 1A
HSPA5	Heat shock protein family A (Hsp70) member 5 (BiP)
ICM	Ischemic cardiomyopathy
ID	Identity domains
i.e.,	Latin: id est, “that is”
IgG	Immunoglobin G
IRE1	Inositol-requiring enzyme 1
kb	Kilobase pair
kDa	Kilo Dalton
KDEL	Lysine-Aspartic acid-Glutamic acid-Leucine
kPa	Kilo Pascal
KLD	Kinase, ligase, DpnI
L	Liter
LOX	Lysyl oxidase
Log2FC	Log 2-fold change
LUM	Lumican
LV	Left ventricular
µ	Micro (10^{-6})
M	Molar
m	Milli (10^{-3})
M DCM1	Male Dilated Cardiomyopathy 1
M DCM2	Male Dilated Cardiomyopathy 2
M ICM1	Male Ischemic Cardiomyopathy 1
M ICM2	Male Ischemic Cardiomyopathy 2
M NF1	Male Normal Fibroblast 1
M NF2	Male Normal Fibroblast 2

MI	Myocardial infarction
min	Minute
µm	Micrometer
mm	Millimeter
mol	Mole
mRNA	Messenger ribonucleic acid
MRTF	Myocardin-related transcription factor
n	Nano (10^{-9})
NaCl	Sodium chloride
NADPH	Nicotinamide adenine dinucleotide phosphate
NaOH	Sodium hydroxide
NBD	Nucleotide-binding domain
No.	Number
NU	Non-uniform
O_2	Oxygen
P	Passage
P/S	Penicillin/streptomycin
PAGE	Polyacrylamide gel electrophoresis
PCR	Polymerase chain reaction
PDGFRα	Platelet-derived growth factor receptor alpha
PDI	Protein disulfide isomerase
PERK	Protein kinase-like ER kinase
PFA	Paraformaldehyde
POSTN	Periostin
ProCol 1	Procollagen type 1
qRT-PCR	Quantitative real-time PCR
RIDD	Regulated IRE1-dependent decay
RIPK1	Receptor-interacting serine/threonine-protein kinase 1
RBD	Rho binding domain
RhoA	Ras homolog (gene) family member A
RNA	Ribonucleic acid
RNA-seq	RNA-sequencing
ROCK	Rho-associated kinase
ROX	5-carboxy-X-rhodamine
RPKM	Reads per Kilobase of transcript per million

RPM	Revolutions per minute
RT	Room temperature
Rv	Reverse primer
scRNA-seq	Single-cell RNA sequencing
SDS	Sodium dodecyl sulfate
sec	Second
SEM	Standard error of the mean
SERCA	Sarco/endoplasmic Ca^{2+}-ATPase pump
snRNA-seq	Single-nucleus RNA sequencing
SRF	Serum response factor
TAZ	Transcriptional coactivator with PDZ-binding motif
TBS	Tris-buffered saline
TBS-T	Tris-buffered saline with Tween 20
TCF21	Transcription factor 21
TEMED	Tetramethylethlenediamine
TGF-β	Transforming growth factor beta
TGN	Thapsigargin
THBS1	Thrombospondin 1
THBS4	Thrombospondin 4
THY1	Thymocyte differentiation antigen 1 (CD90)
Tris	Tris(hydroxymethyl)aminomethane
TUBB	Tubulin beta chain
U	Uniform
U	Unit
UPR	Unfolded protein response
UV	Ultraviolet
V	Volt
XBP1	X-box binding protein 1
xg	Times gravity
YAP	Yes-associated protein
2D	Two-dimensional
3D	Three-dimensional

Abstract

Cardiovascular diseases cause adverse myocardial remodeling due to cardiomyocyte loss and modifications to the extracellular matrix (ECM), which can ultimately lead to contractile dysfunction and pathological cardiac fibrosis. Cardiac fibroblasts (CF) are the main drivers of progressive cardiac fibrosis once they transition into myofibroblasts upon injury, in which they demonstrate an enhanced ECM secretory activity. Understanding the behavior of human CF is crucial for developing urgently needed anti-fibrotic drugs, and tissue engineering models represent a good compromise between complex *in vivo* models and simplified 2D cultures for the necessary investigations. In this context, our group has established a dynamic dual engineered connective tissue (ECT) model with the use of normal primary CF from one male donor and molds with different mechanical constraints as a result of their geometries (non-uniform and uniform). Thus, one primary aim was to further validate and identify differences between our dual ECT model with CF from different donors, including females and patients with end-stage heart failure. The obtained results demonstrated that the uniform geometry generates stiffer and less extensible ECT than the non-uniform geometry. Intriguingly, these two parameters showed a clear inverse regulation. ECT compaction was also closely linked to cell size, whereas ECT contraction was a highly individual parameter dependent upon each donor CF. For most CF, the uniform ECT also showed a higher expression of fibrosis-associated genes. Lastly, prolonged culture gave insight into the lack of a homeostatic steady state between the cellular phenotype and ECM organization. By characterizing these models with different CF, it was also possible to identify delicate regulations of the protein folding machinery. Therefore, the second aim was to unravel the role of ER adaptive processes in the phenotypic CF switch by interfering with the unfolded protein response (UPR). Based on the detected differential expression of RNA-like endoplasmic reticulum kinase (PERK) in non-uniform and uniform ECT, the effects of the PERK inhibitor GSK-2656157 (GSK'157) were investigated. GSK'157 reduced the contraction, compaction, and stiffness of non-uniform ECT and downregulated collagen I expression in ECT and 2D-cultured cells. Furthermore, it inhibited CF proliferation. Despite these anti-fibrotic effects, a paradoxical induction of the UPR was observed. Moreover, PERK inhibition restored collagen I expression after high ER stress induction. Taken together, our dual ECT model could be further validated as an advantageous way to modulate the phenotype of 3D-cultured CF and helped demonstrate that the UPR mediator PERK is an important regulator in ER adaptation and ER stress, as well as an effective regulator of collagen I.

1 Introduction

1.1 Cardiovascular diseases

Cardiovascular diseases (CVD) are the prevailing cause of death globally, estimating around 32% of deaths yearly (World Health Organization, 2021). CVD encompass a wide range of heart conditions that affect the physiological function of the heart or blood vessels. CVD can include coronary artery disease, ischemic heart disease, hypertensive heart disease, rheumatic heart disease, cardiomyopathies, congenital heart disease, valve disease, stroke, heart rhythm disorders, deep vein thrombosis, or pulmonary embolism. Cardiomyopathies can include dilated cardiomyopathy (DCM) and ischemic cardiomyopathy (ICM), both of which can result in pathological cardiac remodeling and heart failure (Vikhorev & Vikhoreva, 2018). Acute event symptoms, such as chest pain, shortness of breath upon light exercise, or heart palpitations, can give warning that hemodynamic stress is occurring, which can lead to myocardial infarction (MI) or, upon prolongation, can trigger heart failure. Heart failure is a complex multisystemic disorder that results in structural and functional changes to the myocardium that affect circulatory physiology. These adverse changes to the myocardial biology result from cardiomyocyte loss and modifications to the extracellular matrix (ECM), which can consequently cause contractile dysfunction and pathological cardiac fibrosis.

1.2 Cardiac fibrosis

The progression of CVD can lead to cardiac tissue remodeling, which often causes the detrimental accumulation of ECM in the heart, otherwise known as cardiac fibrosis. Cardiac fibrosis can be categorized into two distinct types: reparative and reactive (Anderson et al., 1979). Reparative fibrosis can occur after a MI to replace the necrotic tissue due to cardiomyocyte death with ECM to form a scar, which initially maintains the structural integrity of the heart but can also impair the contractile function of the heart (Porter & Turner, 2009). Furthermore, this can also prompt volume overload or eccentric hypertrophy. Reactive interstitial fibrosis can occur in the case of arterial hypertension, where a constant cardiac overload by activation of the renin angiotensin II aldosterone system induces the deposition of ECM between cardiomyocyte layers and around vessels (Weber, 1989). Upon prolongation, pressure overload, or concentric hypertrophy, can cause diastolic dysfunction (Kuwahara et al., 2002). An effective therapy to prevent or halt cardiac fibrosis is still lacking.

1.3 Cardiac cells

The mammalian heart is composed of a complex network of heterogeneous cells. In recent years, single-cell and single-nucleus RNA sequencing (scRNA-seq and snRNA-seq) have made it possible to gather more accurate and refined insight into the various cell type identities in the heart based on their respective gene signatures. The performed studies analyzed different collections of myocardial tissue from the ventricle and atrium, healthy and diseased hearts, as well as from male and female donors. Commonly identified cells in the human heart were cardiomyocytes, fibroblasts, endothelial cells, pericytes, smooth muscle cells, adipocytes, different types of immune cells, and neuronal cells (Koenig et al., 2022; Litviňuková et al., 2020; Tucker et al., 2020). In addition, other less abundant cells, such as mesothelial, lymphatic, epicardial, and endocardial cells, were found in individual studies (Koenig et al., 2022; Litviňuková et al., 2020).

Furthermore, all studies demonstrated that most of the different cell types comprise several distinguishable subpopulations in the healthy and diseased human heart, and that non-myocytes outnumber the myocyte population (Chaffin et al., 2022; Koenig et al., 2022; Litviňuková et al., 2020; Tucker et al., 2020). Although there are differences in the published proportions of the individual cardiac cells, as well as in the number of subpopulations, it is clear that cardiac fibroblasts (CF), which is the relevant cardiac cell investigated in this thesis, form a highly heterogeneous and abundant cell population both in the healthy and diseased heart. The complexity of CF begins with their origin and extends to their broad phenotypic heterogeneity, causing limitations in further elucidation of the fundamental dynamics and biology of these cells. Therefore, the following section describes the characteristics and complexities of the different subpopulations of CF in the healthy and diseased heart.

1.4 Cardiac fibroblasts in the healthy and diseased human heart

CF are essential mediators of the mechanical, structural, and electrical integrity of the heart, as they are the main contributor to the ECM by producing and degrading collagens, proteoglycans, and glycoproteins (Camelliti et al., 2005; Porter & Turner, 2009; Souders et al., 2009; Frangogiannis, 2012). In relation to their morphology, CF are flat, spindle-shaped cells with elongations that lack a basement membrane (Baudino et al., 2006; Chang et al., 2002). CF possess an extensive rough endoplasmic reticulum (ER) and a prominent Golgi apparatus that facilitate the secretion, synthesis, and degradation of ECM for normal tissue homeostasis.

As mentioned above, the proportion of fibroblasts in the healthy ventricle varied in the different studies, ranging from 15.5% to 32.4%, most likely dependent on experimental differences. In addition, Litviňuková et al. demonstrated that the CF proportion is higher in the atrium than in the ventricle, and Koenig et al. found that there is a significant increase in the overall number of CF in DCM (Koenig et al., 2022; Litviňuková et al., 2020). None of the studies identified differences between male and female samples. There were also considerable differences in the number of distinguishable CF subpopulations, which ranged between 4 and 9. Surprisingly, Litviňuková et al. identified three subpopulations that displayed signatures of activated or stressed CF in the healthy heart, which was not confirmed by Tucker et al. (Litviňuková et al., 2020; Tucker et al., 2020).

A comparison of the different transcriptomic data revealed that one common marker for all CF subpopulations is the proteoglycan decorin (*DCN* gene), which regulates collagen fibrillogenesis (Yan et al., 2009). CF subpopulations that were found to be increased in DCM display commonly higher transcript levels of ECM-related genes, including collagen I (*COL1A1*), periostin (*POSTN*), lumican (*LUM*), fibroblast activation protein (*FAP*), and thrombospondin-4 (*THBS4*) (Chaffin et al., 2022; Koenig et al., 2022). Koenig et al. further identified connective tissue growth factor (*CTGF*) as an upregulated transcript, which was investigated together with *COL1A1*, *POSTN*, and *LUM* in this thesis (Koenig et al., 2022).

Although these studies provide valuable insight into the differences between healthy and end-stage diseased CF populations, they offer limited information on earlier time points or temporal processes and potential transient mechanisms involved in cardiac fibrosis. Therefore, scRNA-seq of heart tissue from animal models are described in the following section to highlight the transcriptional plasticity of CF and how rapidly they can change their cellular landscape.

1.5 Time course of the phenotypic shift in cardiac fibroblasts

To give insight into the phenotypic shift of CF early after injury or with a temporal resolution, data from several mouse models are described in the following. In a mouse model of angiotensin II (Ang II)-induced cardiac fibrosis, large-scale scRNA-seq was performed to profile the cardiac cellulome after two weeks of treatment (McLellan et al., 2020). In this study, 14 different cardiac cell types were identified in total. For CF, 7 subpopulations were detected in the healthy heart and two additional subpopulations appeared after two weeks of Ang II treatment. Both subpopulations expressed *Postn* and could be distinguished by the presence of cartilage intermediate layer protein (*Cilp*) and *Thbs4*. Furthermore, both subpopulations

appeared to arise from resident CF and contributed predominately to ECM remodeling. Surprisingly, the *Cilp* and *Thbs4* subpopulations were negative for α-smooth muscle actin (α-SMA, *Acta2* gene), which is considered a general marker for myofibroblasts. In addition, this study describes extensive sexual dimorphism in the gene expression profiles of CF, which could be responsible for the lower degree of fibrosis in female hearts.

A study by Farbehi and colleagues performed scRNA-seq analysis on cardiac interstitial cells from male mouse ventricles at days 3 and 7 post-sham or MI surgery. They identified 9 different types of interstitial cells and the CF population could be further divided into 11 subpopulations: Fibroblast-Sca1-high (F-SH), Fibroblast-Sca1-low (F-SL), Fibroblast-Wnt expressing (F-WntX), Fibroblast-transitory (F-Trans), Myofibroblasts (Myo1 and Myo2), Fibroblast-activated (F-Act), Fibroblast-cycling (F-Cyc), Fibroblast-interferon stimulated (F-IFNS), and Fibroblast-cycling intermediate (F-CI) (Farbehi et al., 2019). The publication described the F-Act, F-Cyc, and Myo subpopulations arose during the course of disease. Approximately 80% of the cells in the F-Act subpopulation showed high expression of *Postn*, and around 28-35% expressed *Acta2*. However, this subpopulation showed much lower levels of *Acta2* expression when compared to the Myo subpopulations. The F-Act subpopulation also showed an upregulation of *Cilp*, which corroborates the previous study by McLellan et al. that this could be a subtype of CF that precedes myofibroblasts. Furthermore, the F-Cyc subpopulation was shown to be a group of proliferating cells, as characterized by the expression of several cell cycle genes. In addition, 88% of the cells in this subpopulation expressed *Postn* and 76% expressed *Acta2*. These descriptive gene signatures support the change of CF phenotypes during the course of heart disease.

Another study investigating the pathological progression of cardiac hypertrophy performed scRNA-seq for mouse hearts at different time points (0, 2, 5, 8, and 11 weeks) after transverse aortic constriction-induced pressure overload. They identified 6 major clusters of cardiac cells and 9 fibroblast subpopulations (Ren et al., 2020). Additionally, they demonstrated that there are complex temporal changes exist in the proportion of the different fibroblast subpopulations, which included transient and continuous increases and declines in number, as well as no changes. Likewise, alterations in the gene expression profile were complex, but it could be shown that *Postn* and *Acta2* expression increased during disease progression.

1.6 Extracellular matrix (ECM) organization

Comprising of a highly organized and dynamic network of non-cellular constituents, the ECM provides structural and regulatory support for tissue composition and cellular communication (Bonnans et al., 2014; Theocharis et al., 2016). The ECM actively responds to physiological and pathophysiological demands by modifying the structure of its non-cellular components via cross-linking. The remodeling process can be mediated through cell-cell and cell-ECM interactions, as well as CF-regulated synthesis and degradation to ensure that the integrity of the ECM is maintained (Bonnans et al., 2014). Major non-cellular constituents of the ECM include filamentous proteins, proteoglycans, and glycoproteins, as well as stored latent growth factors and proteases that may be needed upon injury. Large transmembrane ECM receptors called integrins are also involved in transduction of mechanosensitive signals important for interactions with cardiomyocytes and CF (Chen et al., 2016; Leask, 2013).

The most abundant structural proteins comprising the myocardial ECM are fibrillar collagens, consisting mainly of collagen type I (*COL1A1* and *COL1A2* genes) and collagen type III (*COL3A1* gene) (Bosman & Stamenkovic, 2003); however, other structural proteins include elastin, fibronectin, and laminins (Alberts et al., 2007). Collagen type I and type III fibers possess very different physical properties, allowing collagen type I fibers to support the tensile strength of the heart as they are thicker and stiffer, whereas the finer more compliant collagen type III fibers support the heart's distensibility (Bosman & Stamenkovic, 2003). A study inducing a hypertensive heart model showed that prolonged upregulation of collagen type I increases myocardial stiffness (Whittaker et al., 1989). Furthermore, a study quantifying the type I/type III collagen ratio in DCM hearts demonstrated that an enrichment of collagen type I fibers in the ECM resulted in reduced ventricular compliance (Marijianowski et al., 1995). It is known that collagen-secreting activated fibroblasts and myofibroblasts are the main mediators of the remodeling process due to their ability to exert tension on the matrix and produce a mature scar composed of cross-linked collagen fibers and other matrix components (Gurtner et al., 2008). Cross-linking of the matrix by enzymes, such as lysyl-oxidase (LOX), provides mechanical support for the heart (Adam et al., 2011; Woodiwiss et al., 2001; Zibadi et al., 2009), although extensive cross-linking of collagen fibers has shown to lead to diastolic dysfunction (López et al., 2012).

Additionally, non-structural proteins, or matricellular proteins, act as regulative facilitators that modulate cell function through cell-cell and cell-ECM interactions (Spinale, 2007). Expression of these proteins increases after injury as they bind to cytokines, growth factors, ECM

components, and cell surface receptors and have shown to be critical regulators of cardiac remodeling (Frangogiannis, 2012; Schellings et al., 2009). The already above mentioned matricellular protein POSTN is involved in cellular adhesion and the organization of collagen (Maruhashi et al., 2010; Takeshita et al., 1993). It has been shown that absence of the *Postn* gene in mice subjected to pressure overload and acute myocardial infarction resulted in improper CF function, as the CF were not able to form a proper scar after injury whereas the wild-type mice were normal (Oka et al., 2007; Shimazaki et al., 2008). Another matricellular protein investigated in this thesis, thrombospondin-1 (*THBS1* gene), has been shown to play a significant role in wound healing (Agah et al., 2002). The lack of thrombospondin-1 has also been shown to impair myofibroblast differentiation and result in reduced collagen expression in a mouse model with pressure overload (Xia et al., 2011). Furthermore, the matricellular protein CTGF has been associated with inflammation, cardiac remodeling, and cardiac fibrosis (Leask, 2010).

While proteoglycans may not contribute to the structural properties of the ECM, they play a pivotal role in forming hydrogel complexes that provides the tissue with the proper hydration and swelling capabilities it needs to bear compressive forces, as well as bind to growth factors that mediate cell-cell interactions (Ruoslahti & Yamaguchi, 1991). One example also previously mentioned is lumican, a small leucine-rich proteoglycan (SLRP) family member with a well-documented role in the correct assembly and cross-linking of collagen fibers in the ECM. In a study looking at chronic and acute liver injury in mice, the absence of lumican showed to be protective against hepatic fibrosis by impairing collagen fibrillogenesis (Krishnan et al., 2012). Furthermore, a study evaluating the role of lumican in a mouse model of the heart showed that lumican-deficient mice resulted in collagen fibers with increased fibril diameters and an alteration in fibril assembly (Dupuis et al., 2015).

1.7 Mechanosensitive signaling pathways involved in cardiac fibroblast transdifferentiation

A physiological response to CVD is activation of reparative mechanisms involving myofibroblasts, as they secrete an abundance of structural ECM proteins and release proteases and protease inhibitors for a coordinated tissue repair (Cleutjens et al., 1995). Although dependent upon the nature of the injury, myofibroblast activation can be mediated through pro-fibrotic cytokines, growth factors, neurohumoral mediators, or changes in ECM composition and mechanics (Hinz et al., 2007), e.g., a change in the mechanical strain is sufficient to induce

fibroblast transdifferentiation (Tomasek et al., 2002). To detect external mechanical forces, fibroblasts possess an array of mechanoresponsive receptors, such as G-protein coupled receptors, growth factor receptors, ion channels, and integrins, to elicit intracellular signaling cascades necessary for effective repair (Barnes et al., 2018).

However, prolonged mechanical stress can lead to a pro-fibrotic feed-forward loop. Previous studies have shown that abnormal mechanical conditions, such as increased ECM stiffness, stimulate constant myofibroblast activation and further increase pathological cardiac remodeling, ultimately leading to cardiac fibrosis and maladaptive changes in the structure of the myocardium (Parker et al., 2014; Yong et al., 2015). Therefore, it is necessary to understand these mechanosensitive signaling cascades involved in the transdifferentiation of fibroblasts into myofibroblasts.

There are two main mechanosignaling pathways known to be involved in cardiac fibrosis. One involves the activation of the RhoA-Rho-associated coiled-coil containing kinase (ROCK) pathway, which is essential for the formation of contractile stress fibers (Sandbo et al., 2011). This allows the activated CF to adhere to and contract the surrounding ECM. The GTPase activity of small GTP-binding protein, RhoA, acts downstream of many receptors, including integrins (Loirand et al., 2013), and induces the polymerization of actin fibers. ROCK supports the formation of stress fibers by activating myosin. Consequently, an enhanced RhoA activation lowers the pool of globular actin (G-actin) by building up new actin fibers (Hill et al., 1995; Miralles et al., 2003). This dislodges the myocardin-related transcription factor (MRTF) from G-actin and allows its transport into the nucleus (Cen et al., 2004; Guettler et al., 2008; Miralles et al., 2003). Nuclear accumulation of MRTF allows for interaction with the serum response factor (SRF) and the transcription of important fibrosis-associated genes, including *ACTA2*, *LOX*, and *CTGF* (Cen et al., 2003, 2004; Johnson et al., 2014; Joy et al., 2017; Miralles et al., 2003; Norman et al., 1988; Olson & Nordheim, 2010; Wang et al., 2001). The importance of this pathway in organ fibrosis has been proven by several groups (Bond et al., 2011; Satoh et al., 2003; Shimizu et al., 2001), including our group (Jatho et al., 2015; Ongherth et al., 2015; Santos et al., 2019).

The second mechanosensitive pathway involves Yes-associated protein (YAP)/ transcriptional coactivator with PDZ-binding motif (TAZ) signaling, which is regulated by the upstream Hippo cascade (Zhao et al., 2007). Inactivation of the Hippo pathway by growth-promoting signals dephosphorylates YAP and TAZ, which then translocate into the nucleus where they bind to the TEA DNA-binding domain (TEAD) transcription factors that are known to mediate

the expression of a broad spectrum of genes associated with the cytoskeleton and the ECM (Esnault et al., 2014; Liu et al., 2015; H. Zhang et al., 2009; Zhao et al., 2008). Moreover, in response to mechanical stress, such as ECM rigidity or strain, the YAP/TAZ signaling cascade is regulated by Hippo-independent mechanisms involving the actin cytoskeleton and Rho GTPases (Aragona et al., 2013; Dupont et al., 2011; Elosegui-Artola et al., 2016; Yu et al., 2012). There are indications that YAP/TAZ signaling is involved in cardiac fibrosis. First, uncoupling of the inhibitory Hippo cascade from YAP/TAZ resulted in spontaneous myofibroblast activation and self-sustaining cardiac fibrosis (Xiao et al., 2019). Second, YAP depletion in cardiac fibroblasts attenuated the progression of cardiac fibrosis after MI. Interestingly, a key mechanism in this context is the YAP-dependent upregulation of MRTF, indicating that both mechanical pathways are closely linked together (Francisco et al., 2020).

1.8 Endoplasmic reticulum quality control system

Exclusively found in eukaryotic cells, the ER is an organelle formed by a complex network of tubular membranes and located in the cytoplasm (Alberts et al., 2002). The ER has many cellular functions, including intracellular calcium homeostasis (Krebs et al., 2011), as well as secretory and transmembrane protein synthesis as it is the first compartment of the secretory pathway, and delivery of these properly folded proteins to their target site of action (Stefan et al., 2011). Once the mRNAs for secretory proteins are translated on membrane-bound ribosomes and discharged across the ER membrane from the cytosol, the ER must foster an environment suitable for protein processing, which includes protein folding, maturation, and post-translation modifications involving N-linked glycosylation, single peptide removal, disulfide bond formation, to allow for properly folded proteins to be formed and transported to the Golgi apparatus (Aebi et al., 2010; Braakman & Bulleid, 2011; Hebert & Molinari, 2007; Wallis & Freedman, 2011).

In the case of misfolded or unfolded proteins, the ER initiates a quality control system to correct the conformation of these proteins or to degrade the proteins that cannot be corrected and may become detrimental to cellular function (Trombetta & Parodi, 2003). This quality control system involves sensor molecules, or molecular chaperones, which are abundant in the ER and are capable of deciphering whether proteins have obtained a native confirmation (Ellis & Van der Vies, 1991). These chaperones are able to signal the protein folding and degradation machinery to either assist the folding process or destroy the proteins.

Two major chaperone systems coincide in the ER, the first being the classical chaperone system. The classical chaperone system is found in all cellular compartments (Braakman & Hebert, 2013). This system includes the heat-shock protein (Hsp) 70 and 90 families, which are classified by their molecular weight (i.e., Hsp70 is 70 kDa) (Ellgaard & Helenius, 2003). These chaperones are involved in many processes of cellular proteostasis, including protein assembly/folding, protein transfer into organelles, refolding, and disaggregation of proteins (Bukau et al., 2006; Mayer & Gierasch, 2019; Young, 2010). Specifically, the classical chaperones bind to and release adenosine 5'-triphosphate (ATP)-dependent hydrophobic protein segments through their C-terminal substrate-binding domain (SBD), which is regulated by the N-terminal nucleotide-binding domain (NBD) (Jiang et al., 2005; Mayer & Bukau, 2005). Hsp70 family members typically identify unfolded or misfolded proteins in the early stages of quality control. Binding immunoglobulin protein (BiP, GRP78; or heat shock protein A5 *HSPA5* gene) is the main protein of the Hsp70 family and plays an essential role in many aspects of the quality control system in the ER, such as sensing misfolded or unfolded protein accumulation and using ATP to fold proteins (Otero et al., 2010). However, these chaperones do not act alone. These functions are only successful with the help of functional classes of co-chaperones, such as the Hsp40 family (or DnaJ as they contain a luminally exposed J-domain), which regulate the ATPase activity of the Hsp70 members (Cyr et al., 1992; Tsai & Douglas, 1996). Hsp70 chaperones and Hsp40 co-chaperones then transfer proteins downstream to the Hsp90 chaperone family later during the quality control process (Melnick et al., 1994).

The second quality control system is referred to as the ER-specific carbohydrate-binding chaperone system and involves two lectin chaperones, calnexin and calreticulin, that promote the assembly of glycoproteins (Helenius & Aebi, 2004). Calnexin and calreticulin are also calcium-binding chaperones that can interact with and modify glycoproteins via their lectin-like glycan-binding domain and a P-domain (Chevet et al., 2010; Fliegel et al., 1989; Wada et al., 1991). These hydrophilic (N-linked) glycan modifications occur through interactions with folding enzymes, such as glucosidases and transferases, to recruit factors needed for the maturation, folding, and quality control of proteins in the ER (Hebert et al., 2005; Pearse & Hebert, 2010).

1.8.1 Endoplasmic reticulum stress

Although the ER is a highly specialized organelle with systems to facilitate proper protein synthesis and processing, an imbalance between protein folding demand and the folding capacity of the ER can still occur. This disruption of ER homeostasis is otherwise known as ER stress. ER stress can occur due to depleted ER calcium, disruption in protein folding, chaperone mutations, redox imbalances, and altered protein glycosylation (Senft & Ronai, 2015), as well as through treatment with pharmacological agents (i.e., thapsigargin (TGN), tunicamycin, and brefeldin A) (Oslowski & Urano, 2011). Specifically for this thesis, TGN, a non-competitive inhibitor that modifies the sarco/endoplasmic Ca^{2+}-ATPase pump (SERCA) irreversibly, was used to induce ER stress. Prolonged or unresolved activation of the protein folding machinery due to an accumulation of misfolded or unfolded proteins triggers pro-survival and pro-apoptotic responses, such as the unfolded protein response (UPR) and the ER-associated protein degradation (ERAD) system. However, it should be stated that the UPR and the ERAD systems are very much dependent upon one another (Horimoto et al., 2013; Hwang & Qi, 2018; Sun et al., 2015).

1.8.2 Unfolded protein response (UPR)

In response to mild ER stress, cells employ the UPR to restore ER homeostasis and maintain cell viability (Glembotski, 2008; Schröder & Kaufman, 2005). The UPR attempts to resolve ER stress by halting protein synthesis, increasing the production of chaperones to assist in protein folding, and initiating the ERAD system to resolve the unfolded or misfolded proteins (Lenna & Trojanowska, 2012). However, upon exceedance of the ER stress threshold, activation of pro-apoptotic signaling pathways involving the transcription factor CCAAT/-enhancer binding protein homologous protein (CHOP) can ultimately lead to apoptosis (Zinszner et al., 1998).

The UPR performs these functions through three major ER-anchored receptors, including two type-I transmembrane protein kinases, inositol-requiring enzyme 1 (IRE1) and protein kinase RNA-like endoplasmic reticulum kinase (PERK), as well as a type II transmembrane protein, the activating transcription factor 6 (ATF6) (Schröder & Kaufman, 2005). The ER chaperone, BiP, binds to the ER luminal domains of all three receptors to maintain an inactive status under physiological conditions (Bertolotti et al., 2000). ER stress ensues upon an accumulation of misfolded or unfolded proteins, and BiP is needed to assist these proteins, so it dissociates from the ATPase luminal domains of the three transducers and induces their signaling cascades

(Figure 1) (Hetz, 2012). All three UPR branches increase chaperone production and are interrelated (Li et al., 2014; Zhang et al., 2019).

After BiP dissociates and attends to the misfolded and unfolded proteins, dimerization and autophosphorylation of PERK occur, which activates its kinase activity and transphosphorylation (Bertolotti et al., 2000; Liu et al., 2000). In this state, PERK leads to the phosphorylation of the eukaryotic translation initiation factor 2α (eIF2α), which ceases protein translation (Harding et al., 1999; Prostko et al., 1993; Ron, 2002; Y. Shi et al., 1998). The attenuation of global protein translation helps to reduce the ER load and regain homeostasis. Additionally, phosphorylated eIF2α promotes the translation of selective mRNAs, such as activating transcription factor 4 (ATF4) (Harding et al., 2000, 2003). Under mild ER stress conditions, where adaptation can take place, ATF4 upregulates the expression of genes involved in oxidative stress resistance and amino acid transport (Lu et al., 2004), as well as the stress-induced phosphatase growth arrest and DNA damage-inducible gene 34 (GADD34), which then assists translational recovery by dephosphorylating eIF2α during the ER stress response (Novoa et al., 2001; Ron, 2002). In response to prolonged or acute ER stress, in which the cell is not able to restore ER homeostasis, ATF4 induces a pro-apoptotic pathway that activates CHOP and can influence anti- and pro-apoptotic proteins of the B-cell lymphoma-2 (Bcl-2) family (McCullough et al., 2001; Rao et al., 2004; Rozpędek-Kamińska et al., 2020). PERK inhibition by the ATP-competitive inhibitor GSK-2656157 (GSK'157) was used in this thesis. The IC_{50} of GSK'157 is between 10-30 nmol/L in cells and shows a decrease in phosphorylated-eIF2α, ATF4, and CHOP downstream substrates of the PERK signaling cascade (Atkins et al., 2013).

Upon BiP dissociation, IRE1α becomes activated by autophosphorylation and then dimerizes, which leads to transphosphorylation and activation of the IRE1α ribonuclease (RNase) domain (Shamu & Walter, 1996; Sidrauski & Walter, 1997). IRE1α RNase induces the splicing of specific mRNAs, such as X-box binding protein 1 (XBP1), which acts as an active transcription factor for ER stress response genes encoding proteins for protein folding, ERAD, and protein quality control (Calfon et al., 2002). Additionally, the IRE1α RNase can become unspecific and result in the degradation of mRNAs through regulated IRE1-dependent decay (RIDD) (Han et al., 2009; Hollien et al., 2009; Hollien & Weissman, 2006). RIDD provides the ER with another way to relieve the cargo problem by reducing protein translation and import into the ER. In study using mouse embryonic fibroblasts expressing mutant variants of IRE1α, a microarray-based approach led to the identification that upon ER stress induction, collagen IV

is a RIDD target (Hollien et al., 2009). In this thesis, 4μ8C was used as a selective inhibitor of RIDD activity and XBP1 splicing, as it has been shown to bind to the IRE1α endoribonuclease domain (Cross et al., 2012). The IC_{50} of 4μ8C is between 3-7 μM in cell-based assays for XBP1 and RIDD targets (Cross et al., 2012; Rong et al., 2015).

Finally, once BiP is sequestered away from ATF6, it translocates to the Golgi apparatus, where it is cleaved by site 1 and site 2 serine proteases (S1P and S2P) to produce the active form (Chen et al., 2002). The cleaved ATF6 then translocates to the nucleus and induces transcriptional activation of ER chaperones promoting ER protein folding, leading to cell survival or proteins involved in the ERAD system (Yoshida et al., 2001; Lee et al., 2003). The ERAD system selectively identifies fatally misfolded proteins and transports them across the ER membrane to the cytosol, where proteasomes degrade them via the ubiquitin-proteasome degradation machinery (Römisch, 2005).

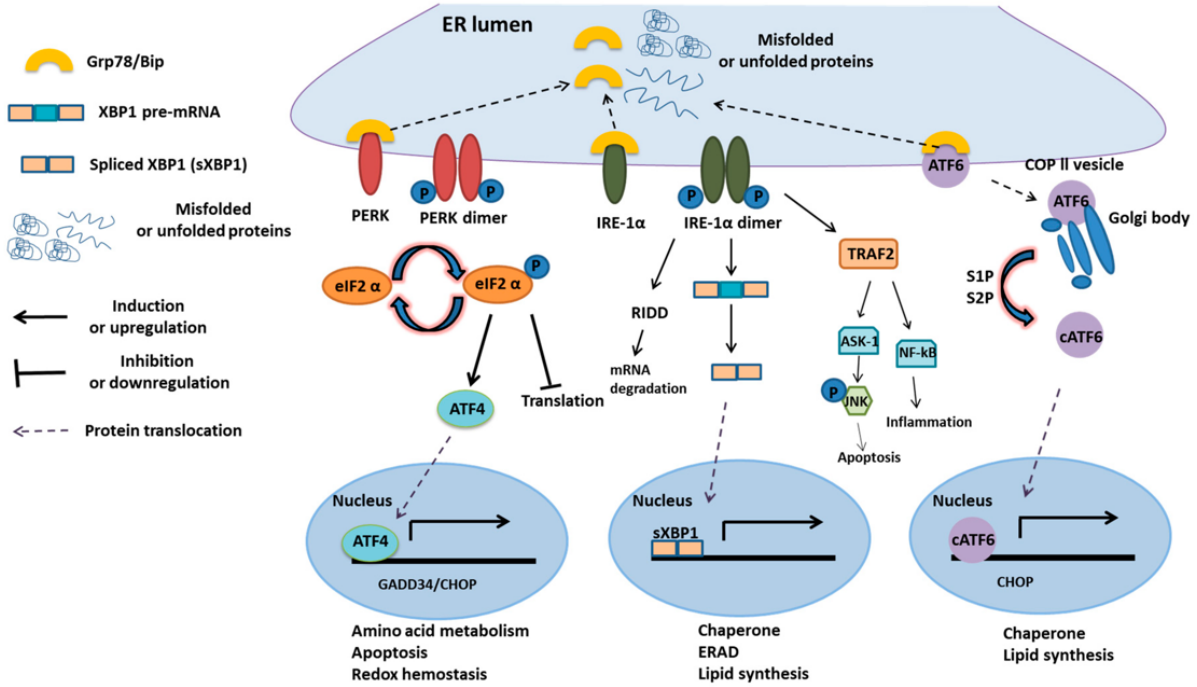

Figure 1. The unfolded protein response signaling cascades. When misfolded or unfolded proteins accumulate in the ER lumen, the cell experiences ER stress. BiP dissociates from the three ER-membrane transducers, protein kinase RNA-like endoplasmic reticulum kinase (PERK), inositol-requiring enzyme 1 (IRE1), and activating transcription factor 6 (ATF6), and activates their downstream signaling cascades. Mild ER stress conditions result in PERK phosphorylation of eIF2α, which stops protein translation. Under high ER stress conditions, the translation of ATF4 is increased, resulting in the upregulation of UPR-related genes. Activation of IRE1α ribonuclease (RNase) domain can splice the mRNA encoding XBP1 and the translationally active XBP1 induces UPR-related genes, or the RNase domain can degrade mRNAs through IRE1-dependent decay (RIDD). ATF6 translocates to the Golgi apparatus and is proteolytically cleaved by S1P and S2P. Cleaved ATF6 induces a subset of the UPR-related genes. All three branches of the UPR increase UPR-related genes encoding ER chaperones and protein folding enzymes. (Taken from Hsu et al., 2019, doi:10.3390/ijms20102518, published under the license CC BY 4.0).

1.8.3 UPR activation in heart disease and cardiac fibrosis

In the context of heart disease, UPR activation in response to ER stress has been implicated in several cases, such as ischemia/reperfusion, pressure overload, and cardiac hypertrophy/heart failure (Minamino et al., 2010; Spitler & Webb, 2014). Furthermore, ER stress and the activation of the UPR have been associated with cardiac remodeling and fibrosis, which is relevant to this thesis. It must be considered that the sensitivity of cardiac cells, such as cardiomyocytes and CF, to ER stress may vary with respect to transcriptional activity leading to a protective role involved in adaptation or a pathological role leading to apoptosis.

In relation to cardiac hypertrophy, it has often been associated with an increase in myocardial stiffness due to an accumulation of fibrillar collagen in the interstitial space of the left ventricle (Morisco et al., 2003). In a study that performed transverse aortic constriction on global CHOP-deficient mice, it was shown that the knockout of CHOP resulted in mice with reduced cardiac hypertrophy, fibrosis, and cardiac dysfunction, as well reduced ER-stress induced apoptosis of cardiomyocytes (Fu et al., 2010). Further work by Yao and colleagues have demonstrated that the *Aggf1* gene specifically plays a role in the regulation of a non-canonical signaling pathway involving CHOP that blocks ER stress-induced cardiomyocyte apoptosis, cardiac hypertrophy, and heart failure (Yao et al., 2017). Therefore, it has been speculated that CHOP may be involved in the detrimental transition from cardiac hypertrophy to heart failure. Additionally, in the hearts of CHOP-deficient mice, enhanced phosphorylation of eIF2α was seen. As mentioned previously, phosphorylation of eIF2α leads to reduced protein translation and Fu et al. has argued that this translation inhibition in CHOP-deficient mice is what facilitated reduced cardiac hypertrophy (Fu et al., 2010).

The UPR ER-membrane transducer, PERK, has also been shown to play a role in the heart. In a cardiomyocyte-specific PERK knockout mouse model where chronic transverse aortic constriction was performed, the expression of CHOP, as well as left ventricular fibrosis and cardiomyocyte hypertrophy were exacerbated compared to control mice (Liu et al., 2014).

In a model of cardiac fibrosis in male mice induced by Ang II, induction of ER stress was shown by the upregulation of ATF4, phosphorylated eIF2α, and CHOP, as well as increased levels of collagen I expression. These effects were attenuated with the chemical chaperone 4-phenylbutyric acid (4-PBA), as shown by no expression of the UPR mediators, decreased cardiac fibrosis, and a decrease in cardiomyocyte size and apoptosis (Kassan et al., 2012).

Similar results were also found in a cardiac fibrosis rat model after subcutaneously injecting isoproterenol, where 4-PBA subsequently decreased collagen deposition (Ayala et al., 2012).

In a study investigating the effect of protein folding demand outweighing the ER's capacity, pressure overload was induced in mice with a mutated Lysine-Aspartic acid-Glutamic acid-Leucine (KDEL) receptor, which is needed by ER chaperones in the early stages of quality control. Results from this study showed that cardiomyocytes from mice with the mutated KDEL receptor were highly susceptible to ER stress, which ultimately led to the development of DCM with congestive heart failure and interstitial fibrosis. Specifically, a significant upregulation of CHOP was found in the mutant hearts, as well as apoptosis of the cardiomyocytes upon activation of the unfolded protein response due to an accumulation of misfolded proteins in the sarcoplasmic reticulum from pressure overload (Hamada et al., 2004).

Furthermore, in a mouse model of cardiac ischemia/reperfusion, all three branches of the UPR and their downstream targets were activated; however, selective pharmacologic activation of the ATF6 branch in cardiomyocytes resulted in transcriptional reprogramming of genes involved in proteostasis to reduce damage to the heart after 24 h, and after 7 days, ATF6 activation acted to preserve cardiac function (Blackwood et al., 2019).

As described above, prolonged or acute ER stress has been shown to lead to cardiomyocyte apoptosis. Based on the single-cell and single-nucleus RNA seq data that was previously introduced and paralleled, the heterogeneity of CF in the course of heart disease results in an ECM gene signature. With respect to cardiac fibrosis and UPR activation, a study published in 2012 by Baek et al. was the first group to provide evidence of the active role of the UPR in fibroblast transdifferentiation in mouse and human lung fibroblasts, in which they demonstrated that the UPR has a pro-fibrotic effect as seen by an increase in α-SMA and collagen type I expression (Baek et al., 2012). Since then, a study looking at adult murine ventricular fibroblasts has found that one UPR signaling transducer, ATF6, also plays a pivotal role in fibroblast to myofibroblast transdifferentiation in response to the transforming growth factor-ß (TGF-ß), as shown by a suppressed induction of α-SMA and fibroblast contraction (Stauffer et al., 2020). Additionally, a mouse model of heart failure-induced UPR activation by calreticulin overexpression resulted in extensive cardiac fibrosis. However, early pharmacological inhibition of the UPR IRE1α pathway by tauroursodeoxycholic acid (TUDCA) prevented cardiac fibrosis (Groenendyk et al., 2016).

There have also been publications describing changes seen in the protein folding machinery of CF as an adaptative mechanism towards an ECM-producing cell to resolve ER stress. For instance, Xiao et al. (2019) demonstrated that genetic deletion of upstream kinases LATS1/2 in the Hippo signaling cascade, which is activated by mechanical cues and regulates ECM genes, leads to spontaneous myofibroblast activation associated with an upregulation of genes related to ER stress and UPR activation. The myofibroblast-like subpopulations that the publication described were associated with *ATF4* expression, which progressively increased in relation to *XBP1* and *DDIT3* (CHOP) expression, indicating a potential role of the Hippo pathway in cardiac ECM homeostasis by adaptation of the protein folding machinery (Xiao et al., 2019).

For the previously described scRNA-seq study demonstrated by McLellan and colleagues (2020), a mouse model of Ang II-induced cardiac fibrosis showed sexual dimorphic correlations. Upon comparing the distribution of cell proportions between male and female in sham- and Ang II-treated hearts, the subpopulation Fibroblast-*Thbs4* was shown to contribute to ECM remodeling but did not express α-SMA and was approximately 2-fold higher in abundance in females than in males. This data is in line with the gene ontology (GO) enrichment analysis of sexually dimorphic genes, where females showed an upregulation of genes enriched in ECM organization and males showed an upregulation of genes related to protein folding and response to ER stress (McLellan et al., 2020).

This data indicates that adaption of the protein folding machinery of CF allows for enhanced ECM production, whereas ER stress leads to a proteotoxic trigger in cardiomyocytes for cell death. Research investigating the link between mild ER stress and CF adaptation that allows for enhanced ECM production should be further pursued, and therefore, was a main aim of this thesis.

1.9 3D-cultured fibroblasts

The mammalian heart is a highly dynamic organ that facilitates a stringent connection between 3D structure and function, with the cardiac ECM playing both a fundamentally active and passive role. For more than 40 years, tissue engineering has aimed to mimic the architecture and function of what physiologically occurs *in vivo* to further study disease propagation and progression, as well as drug discovery for those diseases. CF-based tissue models have been used for some time now to better understand their role in the development of pathological cardiac remodeling. The microenvironment, including both ECM composition and stiffness, as

well as the geometry of a mold in which CF are cultured plays an important role in understanding the heterogeneity of these cells. Several 3D models are available which allow for the further study of the different stages related to cardiac fibrosis and various CF subtypes, such as spheroids and rings. These models can be discriminated between matrix-free, non-dynamic, and dynamic systems.

For instance, in a collagen-free model, a study seeded isolated CF on ultra-low attachment plates, where the cells aggregated and formed spheres within 24 h. This was done to investigate how topological states of CF affect phenotypic cellular changes between 2D- and 3D-culture conditions, and it was demonstrated that 3D-cultured fibroblast gene expression correlates with adverse ventricular remodeling, as well as conditioned medium from these 3D-cultured fibroblasts increased hypertrophy of cardiomyocytes (Yu et al., 2018).

In non-dynamic models, fibroblasts are often seeded on or into predefined hydrogels or polymers and their reaction to the substrate stiffness is investigated (Perera et al., 2019). These models can further be combined with topological investigations, as well as stretch analyses (Al-Haque et al., 2012; Ao et al., 2015). A major drawback of these methods is the lack of matrix remodeling by the cells; therefore, dynamic interactions between fibroblasts and ECM cannot be studied. Moreover, when printed substrates and stretching devices are used, this typically requires complex technical equipment.

Lastly, dynamic models enable studies on the interaction between cells and ECM, as the cells are usually combined with the non-polymerized matrix at the beginning. Therefore, tissue formation relies on the compaction and remodeling activity of the embedded cells. The simplest version of this model is the collagen gel contraction assay (Burgess et al., 1994; Tomasek & Hay, 1984). For this assay, no special equipment or molds are required, but rather the use of a typical cell culture well-plate in which the cell-collagen matrix is poured, and a disc is formed after a short time. An advantage of the collagen gel contraction model is that it allows, to a certain extent, the comparison between constrained and unconstrained tissues (Dallon & Ehrlich, 2008; Mikami et al., 2016). The main parameter measured is the “shrinking” of the collagen-cell disc (Jonas & Duschl, 2010), which reflects the cells’ ability to compact and contract ECM, mimicking processes involved in wound healing (Tingstrom et al., 1992). The discs can also be used for secondary experiments, like protein and mRNA expression analyses. However, it is not possible to measure the biomechanical tissue parameters. In comparison, ring-shaped models in which the tissues form around a fixed central rod or two fixed poles

allow for isotropic morphology and the measurement of biomechanical properties (Elson & Genin, 2016; Wille et al., 2006).

Therefore, our group has established and utilized ring-shaped engineered connective tissue (ECT) models. For instance, Dworatzek et al. investigated the role of 17ß-Estradiol (E2) in 2D- and 3D-cultured rat CF, demonstrating that both *COL1A1* and *COL3A1* expression are downregulated in 2D-cultured female rat CF and upregulated in 2D-cultured male rat CF. In addition, treatment with E2 led to impaired compaction of 3D ECT female rat CF but increased compaction and stiffness in 3D ECT male rat CF (Dworatzek et al., 2019). Additionally, our models were used to study the role of the RhoA-ROCK signal pathways in rat and human CF (Jatho et al., 2015; Ongherth et al., 2015; Santos et al., 2019, 2022).

2 Preliminary results and aims of doctoral thesis

Our group has established ECT models with different geometries, which can be used to differentially influence the human cardiac fibroblast (hCF) phenotype and the biomechanical properties of the tissues (Santos, 2021). In brief, ECT were generated with hCF from a normal human heart either around a central rod (uniform model) or two flexible poles (non-uniform model). Dynamic mechanical analysis revealed that uniform ECT were stiffer and stronger, as well as less elastic and less extensible than non-uniform ECT.

RNA sequencing analysis allowed for a closer look at the phenotypical differences of the embedded cells from non-uniform and uniform ECT after 1 and 5 days of culture. An unbiased principal component analysis mainly identified a clear diversion between the uniform and non-uniform ECT after day 5 (Figure 2A). Furthermore, differences in regulation for fibroblast and myofibroblast genes were compared between the models. Amongst the upregulated genes in uniform ECT at day 5 were typical myofibroblast markers, such as *ACTA2*, *COL1A1*, and *POSTN* (Figure 2B). qPCR analysis also revealed that on the RNA level, correlations with the RNA sequencing analysis could be established (data not shown). When subjecting the differentially expressed genes (DEG) between non-uniform and uniform ECT after day 5 to further analysis of known and predicted protein-protein interactions determined by the online STRING database, three main clusters related to ECM organization, protein folding, and the UPR were identified (Figure 2C).

Therefore, the aims of this thesis were two-fold. Firstly, to further validate and identify differences between non-uniform and uniform ECT with hCF from different donors, including females and patients with end-stage heart failure. Secondly, to unravel the role of ER adaptive processes in the phenotypic hCF switch by interfering with the UPR and protein folding machinery.

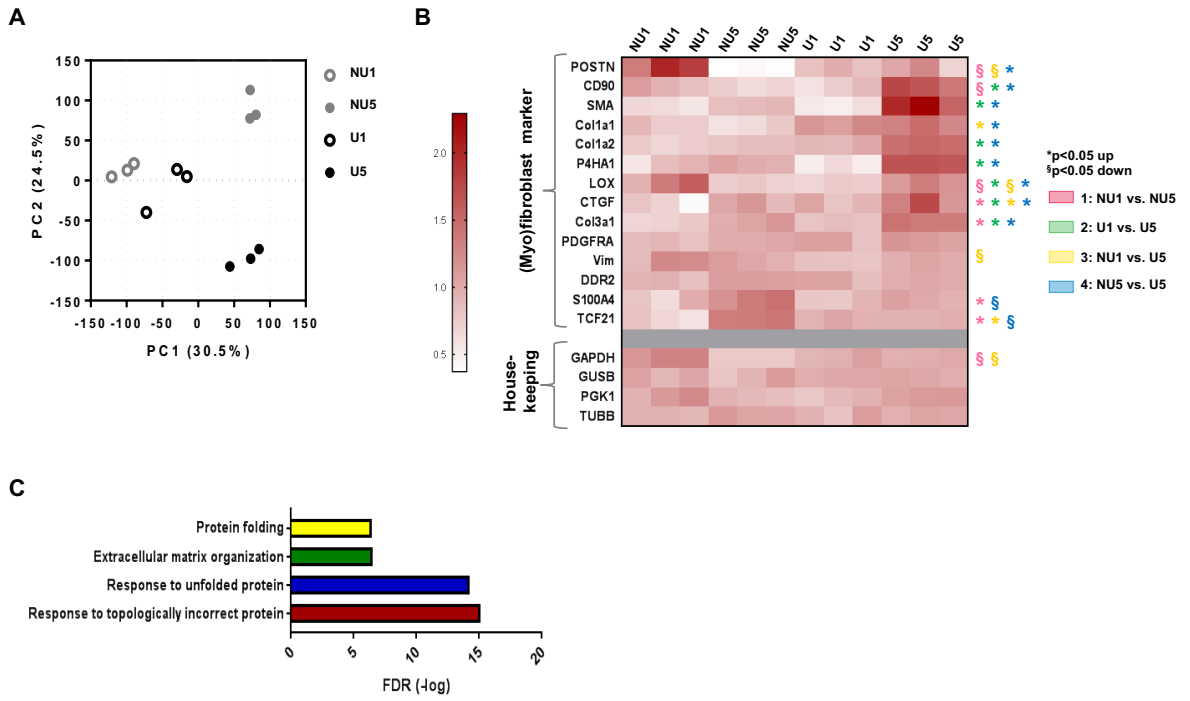

Figure 2. Uniform geometry elicits an upregulation of protein folding genes in ECT after 5 days. 2D-cultured hCF from M NF1 and bovine collagen I were used to generate 3D human engineered connective tissues (ECT) and cast in non-uniform (NU) or uniform (U) molds, then cultured for 1 or 5 days. RNA was isolated and sequencing was performed for 3 independent experiments. **A**) Principal component analysis depicting the regulated genes in NU and U ECT after 1 and 5 days (determined by ClustVis, Reads Per Kilobase Million (RPKM) value under 1). **B**) A heat map representing the relative gene expression of fibroblast and myofibroblast markers is shown, $^{*}p<0.05$ upregulated (up) and $^{\S}p<0.05$ downregulated (down) assessed by 1-way-ANOVA with Tukey's *post hoc* multiple comparisons test. **C**) Differentially expressed genes (DEG) between NU and U ECT after day 5 were used to identify protein-protein interactions determined by the STRING online database (false discovery rate (FDR) ≤0.03, log 2-fold change (Log2FC) ≥1).

3 Materials

3.1 Primary cell lines

Information regarding primary cell donor lines used for all experiments are described in Table 1. Human ventricular cardiac fibroblasts (hCF) obtained from normal (NF) and diseased Caucasian male or female donors were purchased from Lonza (Lonza Walkersville Inc., Walkersville, MD, USA) or PromoCell (PromoCell GmbH, Heidelberg, Germany). The diseased hCF were isolated from explanted hearts with end-stage heart failure - either ischemic cardiomyopathy (ICM) or dilated cardiomyopathy (DCM).

Table 1. Commercially available human ventricular cardiac fibroblasts from Caucasian male or female donors

Abbrev.	Company	Origin	Gender	Age	Health Status	Comorbidity	Lot No.
M NF1	Lonza	Human; ventricular	Male	52	Normal	-	0000421712
M NF2	Lonza	Human; ventricular	Male	46	Normal	-	19TL210281
F NF1	Lonza	Human; ventricular	Female	60	Normal	-	0000565615
F NF2	Lonza	Human; ventricular	Female	32	Normal	-	0000401462
F NF3	Lonza	Human; ventricular	Female	31	Normal	-	0000402836
M ICM1	PromoCell	Human; ventricular	Male	55	Ischemic cardiomyopathy	Diabetes mellitus type 2; hypertension	437Z012.4
M ICM2	PromoCell	Human; ventricular	Male	58	Ischemic cardiomyopathy	Diabetes mellitus type 2; hypertension	411Z027.4
M DCM1	PromoCell	Human; ventricular	Male	48	Dilated cardiomyopathy	-	421Z006.1
M DCM2	PromoCell	Human; ventricular	Male	56	Dilated cardiomyopathy	Hypertension	460Z001.1

3.2 Cell culture medium and supplements

Purchased cell culture medium, supplements, and additional solutions are described in Table 2. The combined components for Fibroblast Growth Medium 3 (FGM-3) needed for the cultivation of hCF, freezing medium for the storage of hCF, Accutase mix needed for the dissociation of hCF, 10x and 2x DMEM needed for the generation of human engineered connective tissue (ECT), and collagenase solution needed for ECT digestion are shown in Table 3.

Table 2. Cell culture medium, supplements, buffers, and reagents

Product	Manufacturer	Catalog No.
Accutase cell dissociation solution	Merck Millipore	SCR005
Casy ton buffer	CASY OLS	5651808
Collagen type I (bovine)	LLC Collagen solutions	CB-024
Collagenase I	Sigma-Aldrich	SCR-103
Dimethyl sulfoxide (DMSO)	Sigma-Aldrich	D2650
Dulbecco's Modified Eagle Medium (DMEM) powder, high glucose	Gibco	52100-039
DNase I	Calbiochem	260913
Dulbecco's phosphate-buffered saline (DPBS), pH 7.2, with Ca^{2+}, Mg^{2+}	Gibco	14040-091
Dulbecco's phosphate-buffered saline (DPBS), pH 7.2, without Ca^{2+}, Mg^{2+}	Gibco	14190-094
Fetal bovine serum (FBS)	Gibco	10270-106
Fibroblast Growth Medium 3 kit (FGM-3)	PromoCell	C-23130
Penicillin (10000 U/mL)/Streptomycin (10000 µg/mL) (P/S)	Gibco	15140-122
TrypLE Express	Gibco	12604-013
Trypsin (2.5%)	Gibco	15090-046

Table 3. Cell culture medium components, supplements, and additional solutions

Method	Medium/Solution	Components
Cultivation of hCF	FGM-3	500 mL FGM-3 basal medium 3
		10% Fetal calf serum (FCS)
		1 ng/mL Basic fibroblast growth factor
		5 µg/mL Insulin
		1% P/S (v/v)
Dissociation of hCF	Accutase mix	100 mL Accutase cell dissociation solution
		0.3 mL Trypsin (2.5%)
		2 mL DNase I solution (1 mg/mL)
Freezing of hCF	Freezing medium	8 mL supplemented FGM-3
		1 mL FCS
		1 mL DMSO
Generation of ECT	10x DMEM	1.34 g DMEM powder
		10 mL ddH_2O
	2x DMEM	2 mL DMEM 10x
		2 mL FCS
		200 U/mL/200 µg/mL P/S
		5.8 mL ddH_2O
Digestion of ECT	Collagenase solution	500 mg Collagenase I
		20 mL FBS
		200 mL DPBS (with Ca^{2+}, Mg^{2+})
	10% FBS in DPBS	50 mL FBS
		450 mL DPBS (without Ca^{2+}, Mg^{2+})

3.3 Chemicals and reagents

A list of chemicals and reagents used in this thesis is shown in Table 4.

Table 4. Chemicals and reagents

Product	Manufacturer	Catalog No.
Acetic acid	Carl Roth	KK62.1
Agarose	peqGOLD Universal Agarose	35-1020
Ammonium persulfate (APS)	PanReac AppliChem	A1142, 0500
β-mercaptoethanol	PanReac AppliChem	A1108, 0100
Bromophenol blue	Sigma-Aldrich	B8026
cOmplete protease inhibitor cocktail tablets (EDTA-free)	Roche	04 693 159 001
CytoBuster protein extraction reagent	Merck Millipore	71009
Ethylenediaminetetraacetic (EDTA)	PanReac AppliChem	A2937, 1000
Ethanol	Carl Roth	5054.4
Glycerol	PanReac AppliChem	A0970
Glycine	PanReac AppliChem	A3707
Hydrochloric acid (HCl)	Sigma-Aldrich	H1758
HOT FIREPol EvaGreen qPCR Mix Plus 5x (ROX)	Solis Biodyne	08-24-00020
Isopropanol	Carl Roth	CP41.5
Lumi-Light^{PLUS}	Roche	12 015 196 001
Methanol	Carl Roth	8388.6
Nuclease-free water	Carl Roth	T143.3
PhosSTOP phosphatase inhibitor cocktail tablets	Roche	04 906 837 001
Ponceau S	Sigma-Aldrich	P3504
Roti-Block 10x (blocking reagent)	Carl Roth	A151.2
Roti-Histofix, 4% PFA (fixative reagent)	Carl Roth	P087.1
Roti-ImmunoBlock 10x (blocking reagent)	Carl Roth	T144.1
Roti-Mark STANDARD (protein marker)	Carl Roth	T851.2
Roti-Mark TRICOLOR (protein marker)	Carl Roth	827.1
Rotiphorese Gel 30 (Acrylamide solution)	Carl Roth	3029.1
Sodium chloride (NaCl)	Carl Roth	9265.2
Sodium dodecyl sulfate (SDS)	PanReac AppliChem	A7249, 1000
Sodium hydroxide (NaOH)	Sigma-Aldrich	30970
SuperSignal West Femto	Thermo Fisher Scientific	34095
Tetramethylethylenediamine (TEMED)	Merck Millipore	1.10732.0100
Tris(hydroxymethyl)aminomethan (Tris)	PanReac AppliChem	A1086
Tris-base	Sigma-Aldrich	T1503
Tris-hydrochloride (Tris-HCl)	Carl Roth	9090.3
Triton X-100	Carl Roth	3051.2
Tween-20	Carl Roth	9127

3.4 Buffers and solutions

A list of buffers and solutions needed for proliferation assays, protein extraction of 2D and 3D samples, lysate sample denaturation, SDS-PAGE, and immunoblotting are provided in Table 5.

Table 5. Buffers and solutions needed for cell biological and protein biochemical methods

Method	Buffer/Solution	Components
Proliferation assay	Permeabilization buffer	19.96 mL 1x DPBS 0.04 µL Triton X-100
	Blocking buffer	18 mL 1x DPBS 2 mL 10x ImmunoRoti-Block
Protein extraction	Lysis buffer	10 mL CytoBuster reagent 1 tablet cOmplete protease inhibitor cocktail 1 tablet PhosSTOP phosphatase inhibitor cocktail
Sample denaturation	4x Loading buffer for SDS-PAGE	50 mL Glycerol 10 mL β-mercaptoethanol 3.6 g Tris 5.7 g SDS 0.2 g Bromophenol blue ddH_2O to 100 mL, pH 7.4 with HCl
SDS-PAGE and immunoblotting	10% APS	1 g APS ddH_2O to 10 mL
	10% SDS	10 g SDS ddH_2O to 100 mL
	1 M Tris solution (pH 6.8)	121.14 g Tris ddH_2O to 1 L, pH 6.8 with HCl
	1.5 M Tris solution (pH 8.8)	181.65 g Tris ddH_2O to 1 L, pH 8.8 with HCl
	10x SDS-PAGE running buffer	60.4 g Tris 28.8 g Glycine 20 g SDS ddH_2O to 2 L, pH 8.3 with HCl
	1x SDS-PAGE running buffer	200 mL 10x SDS-PAGE running buffer ddH_2O to 2 L
	10x transfer buffer	60.57 g Tris 285.3 g Glycine ddH_2O to 2 L, pH 8.4 with HCl
	1x transfer buffer	200 mL 10x transfer buffer 400 mL Methanol ddH_2O to 2 L
	10x Tris-buffered saline (TBS)	48.6 g Tris 175.3 g NaCl ddH_2O to 2 L, pH 7.4 with HCl
	1x TBS with Tween-20 (TBS-T)	200 mL 10x TBS 2 mL Tween-20 ddH_2O to 2 L
	Ponceau S solution	0.2 g Ponceau S 3 mL Acetic acid ddH_2O to 100 mL
	Blocking buffer	5 mL 10x Roti-Block 45 mL ddH_2O

3.5 Biologically active compounds

Purchased biologically active compounds used for 2D and 3D experiments are described in Table 6. All biologically active compounds were dissolved in DMSO with a stock concentration of 10 mM.

Table 6. Biologically active compounds

Biologically active compound	Working concentrations	Manufacturer	Catalog No.
4μ8C	1.7, 5, 17 μM	MedChemExpress	HY-19707
AMG PERK 44 (AMG'44)	0.05, 0.5, 5 μM	MedChemExpress	HY-12661A
GSK-2656157 (GSK'157)	0.03, 0.3, 3 μM	Cayman Chemical	Cay17372-5
Thapsigargin (TGN)	0.3 μM	Cayman Chemical	Cay10522-1

3.6 Antibodies/Fluorescent conjugates

Primary and secondary antibodies/fluorescent conjugates used for immunoblotting or staining are listed in Table 7-9. Antibodies/fluorescent conjugates were diluted according to supplier's instructions. Stock solutions were diluted in 1x TBS-T for immunoblotting or 1x DPBS for staining before they were used for detection.

Table 7. Origin, properties, and dilution of primary antibodies used for immunoblotting

Antibody	Origin/Clone	Dilution	Manufacturer	Catalog No.
α-Tubulin	Mouse/monoclonal	1:2000	Sigma Aldrich	T5168
BiP (C50B12)	Rabbit/monoclonal	1:1000	Cell Signaling	3177
CHOP	Rabbit/polyclonal	1:1000	Proteintech	15204-1-AP
Collagen type I	Rabbit/polyclonal	1:3000	Proteintech	14695-1-AP
GAPDH	Mouse/monoclonal	1:5000	Zytomed Systems	RGM2-6C5
GAPDH	Mouse/monoclonal	1:10000	Proteintech	60004-1-lg
IRE1 (14C10)	Rabbit/monoclonal	1:1000	Cell Signaling	3294
PERK (D11A8)	Rabbit/monoclonal	1:1000	Cell Signaling	5683
Pro-Collagen I	Rabbit/polyclonal	1:1000	Rockland	600-401-D19

Table 8. Origin, properties, and dilution of secondary antibodies used for immunoblotting

Antibody	Origin/Clone	Dilution	Manufacturer	Catalog No.
anti-Mouse IgG-Peroxidase	Rabbit/polyclonal	1:10000	Sigma-Aldrich	A9044
anti-Rabbit IgG-Peroxidase	Goat/polyclonal	1:10000	Sigma-Aldrich	A9169

Table 9. Origin, properties, and dilution of conjugated fluorescent probes used for staining

Fluorescent conjugate	Dilution	Manufacturer	Catalog No.
4', 6-diamidino-2-phenylindole dihydrochloride (DAPI)	1:1000	Roche	10236276001

3.7 Kits

Commercially available kits used are listed in Table 10.

Table 10. Kits

Kit	Manufacturer	Catalog No.
innuPREP DNA/RNA Mini Kit	Analytik Jena	845-KS-2080050
RNeasy Mini Kit	Qiagen	74106
RevertAid First Strand cDNA Synthesis Kit	Thermo Fisher Scientific	K1621

3.8 qRT-PCR specific oligonucleotides

Primer pairs in Table 11 were designed specifically for *Homo sapiens* and purchased from Eurofins Genomics.

Table 11. Forward and reverse primer sequences for qRT-PCR gene analysis

Gene	Forward (Fw) primer (5'-3')	Reverse (Rv) primer (5'-3')
ACTA2	AGAACATGGCATCATCACCA	GCGTCCAGAGGCATAGAGAG
CCDC80	TCCCTGGAGAACTTCCTATCC	AGCAGAGATCACCAGCAACC
CD90 (THY1)	GAAGGTCCTCTACTTATCCGCC	TGCCCTCACACTTGACCAG
COL1A1	GTTCAGCTTTGTGGACCTCC	TGTACGCAGGTGATTGGTGG
CTGF	GGTTACCAATGACAACGCCTC	GTACGGATGCACTTTTTGCC
DDIT3	AAGGCACTGAGCGTATCATGT	TGAAGATACACTTCCTTCTTGAACAC
DNAJB9	CATGAAGTACCACCCTGACAAA	CATCTGAGAGTGTTTCATATGCTTC
EIF2AK3	CCAGCCTTAGCAAACCAGAG	TCTTGGTCCCACTGGAAGAG
GUSB	CGCCCTGCCTATCTGTATTC	TCCCCACAGGGAGTGTGTAG
HSP90AA1	TGACCATTCCATTATTGAGACCT	CAGATCCTTCACAGACTTGTCG
HSP90B1	CTGGAAATGAGGAACTAACAGTCA	TCTTCTCTGGTCATTCCTACACC
HSPA1A	AAGGACCGAGCTCTTCTCG	GGTTCCCTGCTCTCTGTCG
HSPA5	TGTTACAATCAAGGTCTATGAAGGTG	CAAAGGTGACTTCAATCTGTGG
LUM	CGAAAGCAGTGTCAAGACAGTAA	GGCCACTGGTACCACCAA
PDGFRA	GCTCTTTACTCCATGTGTGGGA	ATTAGGCTCAGCCCTGTGAGA
POSTN	GAACCAAAAATTAAAGTGATTGAAGG	TGACTTTTGTTAGTGTGGGTCCT
TCF21	AACGACAAATACGAGAACGGGT	CTCCAGGTACCAAACTCCAAGG
THBS1	GGTGCTGCAGAATGTGAGGT	ACCACGTTGTTGTCAAGGGT
TUBB	ATACCTTGAGGCGAGCAAAA	TCACTGATCACCTCCCAGAAC

ACTA2, Actin alpha 2, smooth muscle; *CCDC80*, Coiled-coil domain containing 80; *CD90*, Cluster of differentiation 90; *COL1A1*, collagen type I, alpha 1; *CTGF*, Connective tissue growth factor; *DDIT3*, DNA damage-inducible transcript 3; *DNAJB9*, DnaJ Heat Shock Protein Family (Hsp40) Member B9; *EIF2AK3*, Eukaryotic Translation Initiation Factor 2 Alpha Kinase 3; *GUSB*, β-glucuronidase; *HSP90AA1*, Heat shock protein 90 alpha class A family member 1; *HSP90B1*, Heat shock protein 90 beta family member 1; *HSPA1A*, Heat shock protein family A (Hsp70) member 1A; *HSPA5*, Heat shock protein family A (Hsp70) member 5; *LUM*, Lumican; *PDGFRA*, Platelet-derived growth factor receptor alpha; *POSTN*, Periostin; *TCF21*, Transcription factor 21; *THBS1*, Thrombospondin 1; *TUBB*, Tubulin beta chain.

3.9 Consumables

Common laboratory consumables that were used during experiments are listed in Table 12.

Table 12. Consumables

Product	Manufacturer	Catalog No.
Cell culture flasks (T-75)	Sarstedt	83.3911.002
Cell culture plates (6-, 12-, 24-multiwell)	Greiner Bio-One	657160 665180 662160
Cell scraper (25 cm, 2-position blade)	Sarstedt	83.1832
Cryotubes Nunc (1.8 mL)	Thermo Fisher Scientific	377267
MicroAmp Optical 384-well reaction plate	Applied Biosystems	4343370
MicroAmp Optical Adhesive Film	Applied Biosystems	4311971
Microcentrifuge tubes (0.5, 1.5, 2.0 mL)	Sarstedt	72.699 72.690.001 72.691
Mini-PROTEAN TGX Stain-Free Gels (12-well, 4-20%)	Bio-Rad Laboratories	456-8095

Table continued on next page

Multiflex pipette tips	Sorenson BioScience	28480
Multipipette tips (2.5 mL)	Eppendorf	0030089650
Nitrocellulose membrane Amersham Protran (pore size 0.2 µm)	GE Healthcare Life Sciences	GE10600001
Parafilm "M"	Bemis Company, Inc.	9170002
Pasteur pipettes (230 mm)	Labsolute	7 691 061
PCR reaction tubes (8-strip, 0.2 mL)	Starlab	I1402-2908
Pipette filter tips (TipOne 10/20, 100, 1000 µL)	Starlab	S1120-3710 S1123-1740 S1122-1730
Pipette tips (10, 100/200 µL)	Sarstedt	70.1130 70.760.002
Pipette tips (TipOne 1000 µL)	Starlab	S1112-1020
Polypropylene tubes (15, 50 mL)	Greiner Bio-One	188271 227261
RNaseZap	Invitrogen	AM9780
Serological pipettes, sterile (2, 5, 10, 25 mL)	Sarstedt	86.1252.001 86.1253.001 86.1254.001 86.1685.001
Strainer (pore size 0.2 µm)	Sarstedt	83.1826.001
Syringe, BD Discardit II 20 mL	BD Biosciences	300296
Tissue culture plate (48-multiwell, TM5)	myriamed GmbH	myrPlate-uniform
Whatmann paper (3 mm)	Sigma-Aldrich	WHA3030917

3.10 Laboratory equipment

Laboratory devices used are listed in Table 13.

Table 13. Laboratory equipment

Device	Type	Manufacturer
Autoclave	VX-150	Systec
Blotting chamber	Mini Trans-Blot Cell	Bio-Rad Laboratories
Camera	AxioCam MRc	Zeiss
Cell counter and analyzer	CASY Model TTC	OMNI Life Science
Cell imaging system	CELLAVISTA	Synentec
Centrifuges	Centrifuge 5417R	Eppendorf
	Centrifuge 5804R	Eppendorf
	Megafuge 40R	Thermo Fisher Scientific
Chemiluminescence imager	ChemiDoc MP	Bio-Rad Laboratories
Gel electrophoresis chamber	Mini-PROTEAN Tetra	Bio-Rad Laboratories
Heating block	Thermomixer comfort	Eppendorf
Incubator	C200	Labotect
Micropipette	Microman	Gilson
Microscopes	Lumar.V12	Zeiss
	CQ1	Yokogawa
pH-meter	inoLab pH Level 1	WTW
Power supply	PowerPac HC	Bio-Rad Laboratories
Rheometer	RSA-G2	TA Instruments
Scales	AX224	Sartorius
	AZ2101	Sartorius
Shaker	Vibramax 100	Heidolph
	27505	Heidolph
Spectrophotometer	NanoDrop	Peqlab Biotechnologie GmbH
Table centrifuge	Centrifuge 5415D	Eppendorf

Table continued on next page

Thermal cyclers	Mastercyler gradient	Eppendorf
	7900HT Fast Real-Time PCR System	Applied Biosystems
Tissue lyser	TissueLyser II	Qiagen
Ultra-pure water system	Milli-Q	Merck
Vacuum pump	Laboport	KNF
Vortexer	VF2 W	Krannich

3.11 Software

Software programs needed for various analyses are listed in Table 14.

Table 14. Software programs

Software	**Version**	**Manufacturer**
Arduino	1.8.5	Arduino
AxioVision	4.8.2	Carl Zeiss
CELLAVISTA	2.2	SynenTec
YT-Software		SynenTec
GraphPad Prism	8 & 9	GraphPad Software Inc.
ImageJ	1.51g	National Institute of Health
Image Lab	6.1	Bio-Rad Laboratories
microDisplay	5.4.1.2	Silicon Software
Microsoft Office	16.64	Microsoft Corporation
ND-1000	V3.8.1	NanoDrop Technologies
Quantity One	4.6.5	Bio-Rad Laboratories
ABI 7900HT	SDS 2.4	Applied Biosystems
Soft Max Pro	5.4	Molecular Devices
Trios		TA Instruments

4 Methods

4.1 Cell biological methods

4.1.1 Passaging and cultivation of human cardiac fibroblasts (CF)

Human CF were purchased from Lonza or PromoCell. Details regarding the donor hCF characteristics can be found in Table 1. The cells were obtained from the left ventricle of adult males and females ranging from 31-60 years of age. hCF were cultured in FGM-3 supplemented with 10% fetal calf serum (FCS), 1 ng/mL basic fibroblast growth factor, 5 µg/mL insulin, and 1% v/v Penicillin/Streptomycin (P/S) (Table 3) under normal oxygen conditions in a humidified incubator with 5% CO_2 at 37°C. For all experiments, cells were used between passages (P) 4-8. All cell cultures were expanded in T75 culture flasks and passaged when reaching optimal confluency (80-90%). When subculture was necessary, the old medium was aspirated from the cell monolayer and rinsed with 10 mL of pre-warmed 1x DPBS. Following this step, the cells were incubated with 3 mL of pre-warmed Accutase mix for 30 min at 37°C to facilitate cell detachment. The dissociation reaction was deactivated with the addition of an equal volume of FGM-3, in which the cells were thoroughly resuspended into a single-cell suspension. Cells were counted using a CASY TTC cell counter system and then pelleted at 300 xg for 5 min. Afterwards, cells were resuspended in new FGM-3 and seeded at the required density onto new non-coated culture flasks or frozen down for later use.

4.1.2 Freezing and thawing of human CF

hCF were harvested as close to 80-90% confluency as possible. Cells were frozen down to create stock aliquots from which subsequent cultures of the donor cell line could occur. Cell monolayers were detached from the culture vessel with the previously stated dissociation process (4.1.1) and counted using a CASY TTC cell counter. Following this step, the cells were centrifuged for 5 min at 300 xg to pellet the cell suspension, and 1-2x10^6 cells/mL were gently resuspended in freezing medium (FGM-3, 20% FCS, and 1% DMSO) (Table 3). Cells were then transferred into cryovials (1 mL/vial) and immediately placed into an isopropanol insulated container which was stored overnight at -80°C to ensure the cells reduced their temperature at a rate of 1°C/min to maintain viability. After 24 h, the cells were removed from the isopropanol insulated container and transferred to a -152°C freezer for long-term storage.

During the process of thawing frozen aliquots of cell lines to begin a new culture, cryovials were thawed as quickly as possible by placing them into a 37°C water bath. Thawed cells were immediately transferred into polypropylene tubes containing 50 mL FGM-3 and distributed into T75 flasks for subsequent experiments.

4.1.3 Cell count, size, and viability measurements

Cell number, diameter, volume, and viability measurements from single-cell suspensions were assessed using a CASY Model TTC cell counter and analyzer, according to the manufacturer's instructions.

4.1.4 Proliferation assay

Passage 4 hCF were subcultured in a 24-well plate with a cell density of 5,000 cells/well. Cells were incubated with FGM-3 without any treatment for 24 h to allow cells to attach to the surface. After 24 h, cells were incubated with and without GSK'157 in FGM-3 over the course of 6 days (refer to Table 6 for working concentrations). Medium with and without GSK'157 was changed every second day, and the cells were fixed at days 0, 2, 4, and 6. For fixation of the cells at the respective time points, cells were washed two times with 1x DPBS (500 µL/well), then incubated with 250 µL Histofix for 5-10 min at room temperature (RT) and washed two times again with 1x DPBS. For nuclear staining and the subsequent cell quantification, the cells were first permeabilized with 0.2% Triton X-100 diluted in 1x DPBS over a maximum duration of 3 min. Following this step, the cells were washed two times with 1x DPBS and blocked with 1x ImmunoRoti-Block (250 µL/well) for 1 h at RT. After, DAPI (1 µg/mL) diluted in 1x DPBS was applied to the fixed cells for 1 h at RT on a mechanical shaker and covered with aluminum foil for protection from light. The cells were washed twice with 1x DPBS, and 250 µL 1x DPBS was added to each well. Subsequently, the stained cell nuclei were counted automatically using the CELLAVISTA cell imager system. Imaging was performed with a 10x objective. Quantification of relative changes in cell number between conditions was calculated based on the estimated cell number measured at day 0. For long-term storage of fixed and stained cells, 1 mL of 1x DPBS was added to each well, sealed with a flexible film around the opening of the plate, and stored at 4ºC.

4.2 3D human engineered connective tissue (ECT) methods

4.2.1 Generation of ECT

2D-cultured hCF from normal and diseased male or female donors together with bovine collagen I were used to generate ECT in different casting molds described in 4.2.2. All steps were performed on ice to ensure that the integrity of the collagen was not compromised. 10x DMEM and 2x DMEM were prepared according to Table 3. The 2x DMEM was filtered using a 0.2 µM sterile syringe filter to guarantee sterility. Depending on the respective experiment, hCF were cultured to P 4 or P 7 and harvested according to the description in 4.1.1. Once the hCF were collected in a single-cell suspension, the cells were counted using a CASY TTC cell counter system.

For the generation of a single ECT, a master mix consisting of 0.3 mg acid-solubilized bovine collagen type I, 2x DMEM, NaOH, and $0.75x10^6$ cell suspension in FGM-3 was used. Refer to Table 15 for the specific volumes of each component based on the stock concentration of bovine collagen type I. The calculated cell fraction needed for the respective number of ECT ($0.75x10^6$/ECT) was then pelleted at 300 xg for 5 min, and the cell pellet was resuspended in the respective volume of fresh supplemented FGM-3 and kept on ice until incorporation into the master mix. For the master mix, 2x DMEM was mixed with bovine collagen type I in a clean polypropylene tube and gently mixed. Following, 0.2 M NaOH was added slowly to neutralize the pH of the master mix. The cell suspension was then carefully added to the master mix in a circular motion to mix and avoid bubbles. The final volume for a single ECT was 180 µL. When many ECT were required, a master mix of all components for the calculated number of ECT was prepared.

Table 15. Volume of each component for the generation of a single ECT

Component				
Stock concentration of bovine collagen type (mg/mL)	5.61	6.4	6.5	6.84
	Volume per single ECT (180 µL) (based on stock concentration of collagen)			
0.3 mg/ECT bovine collagen type I	53.5	46.5	46.2	43.9
2x DMEM (v/v, bovine collagen/2x DMEM)	53.5	46.5	46.2	43.9
0.2 M NaOH	4	4	4	4
$0.75x10^6$ cells/ECT	69	83	83.6	88.2

4.2.2 Casting molds for ECT generation

The master mix provided in 4.2.1 was then used to cast into two different types of molds, dependent upon the specifics of the individual experiment. For this project, ECT were

generated in either 48-well mold plates with two flexible poles (myriamed; #myrPlate uniform) or molds prepared manually in glass Petri dishes lined with polydimethylsiloxane. The commercially available 48-well mold plates with two flexible poles allowed for passive longitudinal contraction, which is further described in 4.2.3. The ECT generated in the 48-well mold plates with two flexible poles are referred to as non-uniform ECT. As an extra control for the non-uniform model, an insert with two poles that contained a spacer and did not allow for the passive longitudinal contraction of the ECT was printed from MED610 material which replaced the original flexible poles. For the self-prepared molds, a silicone cord supported the insertable central rods made from several different material properties. In most cases, a versilic rod was used, but when stated, the central versilic rod was exchanged with a rod made from Z-dupe (Henry Schein dental, termed silicone A15) or 0.75% agarose in 1x DPBS. The ECT generated using the self-prepared molds with different materials are referred to as uniform ECT. The material properties and shore values (referring to the hardness) of the poles and rods used for the different casting molds can be found in Table 16. The shore value of the agarose rod in the uniform model was based on verification from two publications investigating how to imitate soft tissues to measure their reaction forces and mechanical properties (Oflaz & Baran, 2014; Tejo-Otero et al., 2022).

Table 16. Material properties of ECT casting molds

Mold/Material	Geometry of ECT	Shore value	Bending stiffness (mN/mm)
TM5MED	Non-uniform	A 46	1.70
MED610	Non-uniform	D 83-86	-
Versilic silicone	Uniform	A 62	-
Z-dupe (silicone A15)	Uniform	A 15	-
0.75% agarose	Uniform	00 15-25	-

Once the ECT were generated and cast into the different molds, the ECT were placed in an incubator for 30 min - 1 h for condensation before pre-warmed FGM-3 (Table 3) was added to each well or casting dish.

For data referring to the characterization of the non-uniform and uniform ECT models generated with different hCF donors, ECT were cultured for 5 or 13 days. For data referring to non-uniform and uniform ECT treated with or without GSK'157 (refer to Table 6 for working concentrations), the ECT were cultured for 5 days. FGM-3 with or without treatment was changed every second day.

4.2.3 Passive deflection of the poles for non-uniform ECT

The non-uniform ECT cast in the 48-well mold plates with two flexible poles allowed for the passive longitudinal contraction of the ECT. The poles integrated an optical fluorescent brightener which could be seen when exposed to UVA light, and contraction could be measured based on the deflection of the poles over the culture period. The distance between the poles was measured using ImageJ, and the changes in pole deflection were always presented as a percentage relative to day 0.

4.2.4 Compaction assessment of ECT

The cells' ability to compact the collagen matrix after 5 and 13 days in culture was assessed by estimating the cross-sectional areas (CSA) of the ECT. The CSA of each ECT were also used to normalize the individual biomechanical property measurements described in 4.2.5. For non-uniform ECT, macroscopic images of the top view were taken while the poles were upright and in their original place within the mold. Images of the side view were taken once the poles were removed from their upright position and placed on their side within the well (Figure 3A). Uniform ECT were first removed from the mold, and macroscopic images were taken from the side view. The central rod allowed for the top view to also be measured while placed on the side within the well (Figure 3B). All images were taken using the AxioCam mRc on the Lumar V12 stereo microscope. The diameter of each ECT was measured in several positions for both the top and side views using ImageJ, and the averages were used to estimate the CSA in mm^2 based on an elliptical shape for non-uniform and uniform ECT (Figure 3C).

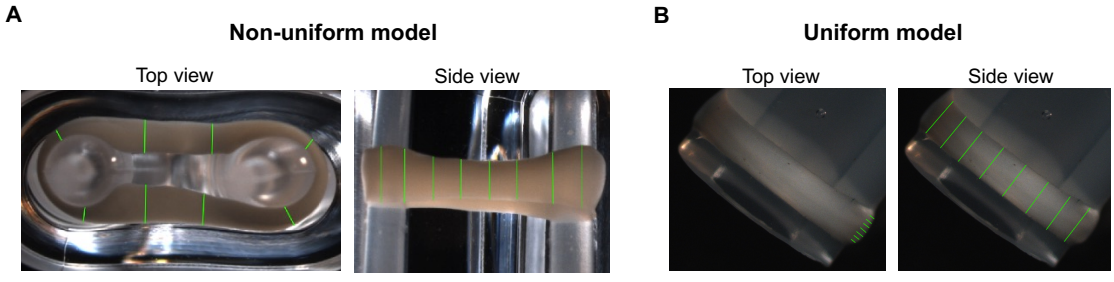

Figure 3. Compaction assessment of non-uniform and uniform ECT. Macroscopic images of the top and side views of ECT were taken to estimate the cross-sectional areas (CSA) and determine compaction over time. Representative images of **A**) non-uniform and **B**) uniform ECT are shown. The green lines indicate the positions where the diameters were measured for the top and side views. **C**) The averages for the diameter of the top view ($d_{average\ top\ view}$) and side view ($d_{average\ side\ view}$) were used to estimate the CSA based on an elliptical shape.

4.2.5 Biomechanical property measurements

Destructive tensile strength measurements were performed to assess the biomechanical properties of the ECT. This was done via a dynamic mechanical approach using a RSA-G2 rheometer, which involves applying a uniaxial tension force that stretches the ECT at a constant linear rate of 0.03 mm/s until rupture. The rheometer consists of two parallel arms, with a lower arm that is static and an upper arm that is attached to a transducer. The lower arm is also equipped with an organ bath containing 1x DPBS in which the ECT is submerged and kept at a constant temperature of 37ºC during measurements. The lower and upper arms both have hooks that are aligned, where the ECT can be carefully mounted. Before measurements, the upper arm is raised up to a position that allows for a gap between the top and bottom of the ECT. This is referred to as the initial gap, or L_0, and is critical information when plotting the stress-strain curve. The initial force was always set to zero before beginning the measurements. ECT were then stretched until rupture, and the total gap, L_{total}, was recorded alongside the force and strain at each time point. The data were extracted and normalized by dividing the measured forces by the CSA (4.2.4) of each respective ECT to calculate the stress (kPa) values. The stress values were then plotted against the strain values with the equation $(L_{total}-L_0)/L_0$ and converted into a stress-strain curve (Figure 4).

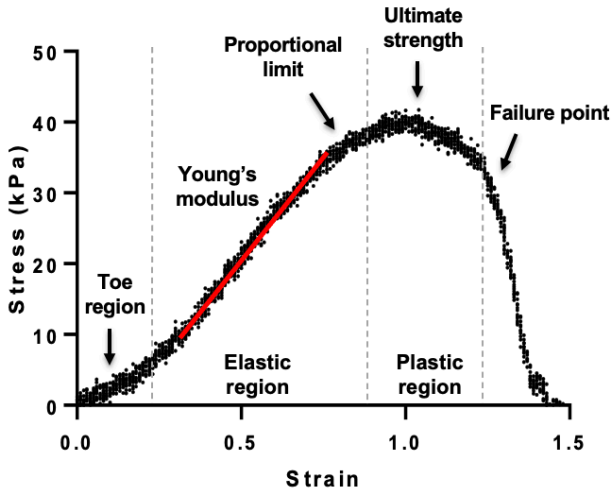

Figure 4. Representative stress-strain curve from destructive tensile force measurement of ECT. ECT were subjected to dynamic mechanical analysis in which a uniaxial tension force was applied at a constant linear rate (0.03 mm/s) until rupture. The values were converted to a stress-strain curve that is divided into three main regions: toe, elastic, and plastic. The toe region indicates the initial fiber alignment in the direction of the stress that is applied once the ECT begins to stretch. Once the ECT stretches further, the stress then becomes proportional to the strain and the elastic region begins. Within the elastic region, the slope can be defined and is referred to as the Young's modulus or stiffness of the ECT. The slope is no longer constant after the stress reaches the proportional limit. Further stress beyond this limit will cause irreversible deformation to the ECT. The highest

point of the stress-strain curve is referred to as the ultimate strength, and stress beyond the ultimate strength leads to rupture or the failure point of the ECT.

Several parameters were identified manually from the stress-strain curve. The first part of the stress-strain curve is referred to as the toe region and represents a small stress that causes the fibers in the ECT to begin to align in the direction of the stress. This re-alignment provides additional length. Following the toe region, the elastic region begins where the fibrils themselves are stretched and the strain becomes proportional to the stress, which is otherwise known as the linear region or slope. The slope of the linear region is the Young's modulus, or the stiffness, as it defines the relationship between stress (force/unit area) and strain (proportional deformation). In order to determine the Young's modulus, a linear regression analysis was performed.

After the stress reaches the proportional limit, the slope is no longer constant and the plastic region beings. Stress beyond the proportional limit will cause permanent deformation of the ECT. The strain at the proportional limit gives an indication of the elasticity of the ECT. The highest point on the stress-strain curve is referred to as the ultimate strength and indicates the onset of failure toward ECT rupture. Stress beyond the ultimate strength will cause rupture of the ECT. Upon rupture, or the failure point, of the ECT, the ultimate strain can be determined and gives important information regarding the extensibility of the ECT.

4.2.6 Dissociation of ECT

To assess the viability of isolated 3D-cultured hCF, ECT were enzymatically dissociated after 5 days. First, ECT were washed with 1x DPBS and then transferred to a 24-well plate. Following this step, ECT were incubated in 500 µL pre-warmed collagenase solution containing 2 mg/mL collagenase type I and 20% FBS in 1x DPBS with Ca^{2+} and Mg^{2+} (Table 3) for 2 h at 37°C to ensure the breakdown of collagen. The supernatants were then collected into polypropylene tubes and placed on ice. The remaining ECT were washed with pre-warmed 1x DPBS without Ca^{2+} and Mg^{2+}. Afterwards, the ECT were incubated in 500 µL pre-warmed Accutase mix containing Accutase cell dissociation solution, 0.025% Trypsin, and 20 µg/mL DNase I solution (Table 3) for 30 min at 37°C to ensure dissociation of the matrix. Once the ECT were incubated in the Accutase mix, the cells were gently resuspended to allow for mechanical dispersion and complete dissociation. The cell suspensions were then transferred to the polypropylene tubes and kept on ice. Then, 1 mL of 1x DPBS without Ca^{2+} and Mg^{2+}

but containing 5% FBS was added to the cell suspensions. Subsequently, the cell suspensions were centrifuged at 100 xg for 10 min at 4°C and the cell pellets were once again resuspended in pre-chilled 1 mL 1x DPBS containing 5% FBS. The cells were counted using a CASY TTC cell counter system and their viability, diameter, and volume were recorded.

4.3 Protein biochemical methods

All buffer components needed for protein analysis can be found in Table 5.

4.3.1 Protein extraction from 2D-cultured hCF and 3D ECT

hCF were seeded onto 6- or 12-well plates at a density between 55,000- 400,000 cells/well and cultured in FGM-3 with or without treatment (refer to Table 6 for biologically active compounds and working concentrations) for the indicated amount of time. 3D ECT were generated with hCF and bovine collagen and cultured in FGM-3 with or without treatment for the indicated amount of time. FGM-3 with or without treatment was changed every second day. In the case of 2D-cultured hCF with or without treatment, the medium was also collected on day 4 of culture when indicated.

For protein extraction from 2D-cultured hCF and 3D ECT, all steps of protein lysate preparation were performed on ice. Before extraction, 2D-cultured cells were washed with 1 mL of 1x DPBS/well, whereas a pool of two to three 3D ECT were previously washed with 1x DPBS before being placed into liquid nitrogen (snap-freezing) on the day of harvest. 2D-cultured cells (200 µL/well in 6-well plates or 100 µL/well in 12-well plates) and pooled 3D ECT (450 µL/3 ECT) were lysed with CytoBuster protein extraction reagent supplemented with both cOmplete protease and PhosSTOP phosphatase inhibitor cocktails for 5-10 min. 2D-cultured cell lysates were detached via scraping with a cell scraper, and samples were gently resuspended several times for complete homogenization. Triplicates were transferred to a 1.5 mL microcentrifuge tube. For the pooled 3D ECT, one stainless steel bead was placed into the microcentrifuge tubes and a tissue lyser was used at 30 Hz for 90 sec to allow for complete mechanical disruption of the ECT to yield high amounts of protein. The bead was carefully removed and the cell/ECT homogenates were centrifuged for 30 min at 12,000 xg at 4°C to remove all cell debris. The supernatant containing the cell/ECT lysates were transferred to a new 1.5 mL microcentrifuge tube. Cell/ECT lysates were stored at -80°C unless directly processed for sodium dodecyl sulfate polyacrylamide gel electrophoresis (SDS-PAGE). For SDS-PAGE cell/ECT lysates, a 3:1 ratio of 4x Laemmli loading buffer containing SDS and

β-mercaptoethanol was added to the lysate fraction and incubated for 5 min at 95°C in a heating block to allow for protein denaturation. Samples that were not heated were stored at -80°C for later use.

4.3.2 SDS-PAGE

For analysis of protein expression in total cell/ECT lysates, SDS-PAGE was performed under denaturing conditions to separate protein samples according to their molecular weight. The discontinuous gel system consisted of both the stacking and resolving polyacrylamide gels, where proteins are loaded and separated electrophoretically. For this project, a 5% stacking gel and 6%, 8%, 10%, or 15% resolving gels were used based on the molecular weight of the protein of interest. The components for a single SDS-PAGE stacking gel (3 mL) and for a single 6%, 8%, 10%, or 15% resolving gel (5 mL) can be found in Table 17. The Roti-Mark STANDARD or TRICOLOR protein ladder was used for protein size determination. Separation of proteins was performed with 1x SDS-PAGE running buffer (Table 5) at 200 V for 45-50 min.

Table 17. Components for a single SDS-PAGE stacking gel and a single resolving polyacrylamide gel

Component	**Stacking gel (mL)**	**Resolving gel (mL)**			
	5%	6%	8%	10%	15%
ddH_2O	2.1	2.6	2.3	1.9	1.1
Acrylamide solution	0.5	1.0	1.3	1.7	2.5
1.5 M Tris/HCl (pH 8.8)	-	1.3	1.3	1.3	1.3
1.0 M Tris/HCl (pH 6.8)	0.38	-	-	-	-
10% SDS	0.03	0.05	0.05	0.05	0.05
10% APS	0.03	0.05	0.05	0.05	0.05
TEMED	0.003	0.004	0.003	0.002	0.002
Total	3 mL	5 mL	5 mL	5 mL	5 mL

4.3.3 Immunoblotting

After SDS-PAGE (4.3.2), the resolving gel was then electrotransferred onto a nitrocellulose membrane using 1x transfer buffer (Table 5) and a transfer apparatus. The transfer apparatus consisted of an assembled cassette: fiber pad, two filter papers, resolving gel, nitrocellulose membrane, two filter papers, and fiber pad. The transfer was performed with ice cold transfer buffer and an ice pack at 100 V for 1 h.

Subsequently, the membrane was stained with Ponceau S and imaged to verify the quality of the transfer. All membrane blots were blocked with 1x Roti-block blocking solution diluted in ddH_2O on a mechanical shaker for 1 h at RT to prevent unspecific binding during detection.

The membranes were incubated with primary antibodies diluted in TBS-T buffer as indicated in Table 7 on a mechanical shaker overnight at 4°C. Membranes were washed three times with 1x TBS-T for 10 min and incubated with diluted anti-mouse IgG-peroxidase secondary antibody or anti-rabbit IgG-peroxidase secondary antibody as indicated in Table 8 on a mechanical shaker for 1 h at RT. Blots were washed three times with 1x TBS-T and proteins of interest were detected and visualized with the SuperSignal West Femto Maximum Sensitive Substrate or Lumi-Light^{PLUS} chemiluminescent reagent substrate solution, which allowed the signals to be detected using the ChemiDoc MP Imaging System according to the manufacturer's instructions. Semi-quantitative image analysis was performed with ImageLab software v6.1.

4.4 Molecular biology methods

Specific kit information needed for RNA/DNA isolation and complementary DNA (cDNA) synthesis can be found in Table 10.

4.4.1 RNA/DNA isolation of 2D-cultured hCF and 3D ECT

hCF were seeded onto 6- or 12-well plates at a density between 55,000-400,000 cells/well and cultured in FGM-3 with or without treatment (refer to Table 6 for biologically active compounds and working concentrations) for the indicated amount of time. 3D ECT were generated with hCF and bovine collagen and cultured in FGM-3 with or without treatment for the indicated amount of time. FGM-3 with or without treatment was changed every second day.

Before isolation, 2D-cultured cells were washed with 1 mL of 1x DPBS, whereas a pool of two to three ECT were previously washed with 1x DPBS before snap-freezing on the day of harvest. The lysis solution provided in the RNA/DNA kit was applied to the 2D-cultured cells (200 µL/well in 6-well plates or 100 µL/well in 12-well plates) or the pooled ECT (450 µL/3 ECT). Multiple wells of the same condition for 2D-cultured cells were detached via scraping with a cell scraper and pooled together in a 2.0 mL microcentrifuge tube. One stainless steel bead was then placed into the microcentrifuge tubes for both 2D-cultured cells and pooled 3D ECT, and a tissue lyser was used at 30 Hz for 90 sec to allow for complete disruption of the samples to yield high amounts of DNA and RNA. The bead was then carefully removed.

Following these preparation steps, total RNA and/or DNA was isolated from 2D-cultured hCF and 3D ECT using the RNeasy Mini Kit (Qiagen) or innuPREP DNA/RNA Mini Kit (Analytik

Jena) as specified by the manufacturer. Total RNA was eluted in RNase-free water and the DNA was eluted in elution buffer. The concentration (ng/µL) and purity (ratio of absorbance at 260 nm and 280 nm) was assessed with a NanoDrop 1000 spectrophotometer. RNA samples were then used directly for complementary DNA (cDNA) synthesis or stored at -80°C. DNA samples were stored at -20°C.

4.4.2 cDNA synthesis

Isolated RNA served as a template for cDNA synthesis using the RevertAid First Strand cDNA Synthesis Kit according to the manufacturer's instructions. For all 2D experiments, cDNA was synthesized from 1000 ng of isolated RNA. Due to a lower RNA yield, cDNA from 3D ECT samples was synthesized in a range between 330 – 1000 ng RNA. To begin cDNA synthesis, template RNA was diluted with varying amounts of nuclease-free water calculated up to 11 µL based on the RNA concentration obtained after isolation. To initiate reverse transcription, 1 µL oligo dT_{18} primer was added and incubated for 5 min at 65°C in a PCR thermocycler. Following this step, the 8 µL reaction mix (Table 18) was added to the samples (20 µL total), gently mixed, centrifuged, and then incubated for 60 min at 42°C to allow for reverse transcription. Subsequently, samples were incubated for 5 min at 70°C to stop enzymatic activity. As a result, mRNA was amplified, and reverse transcribed into cDNA. Samples were used for quantitative real-time PCR or stored at -20°C until further use.

Table 18. cDNA synthesis reaction mix

Component	Volume of master mix per single reaction (20 µL)
5x Reaction Buffer	4
RiboLock RNase Inhibitor (20U/µl)	1
10mM dNTP Mix	2
RevertAid M-MuLV RT (200U/µl)	1
Total	8

4.4.3 Quantitative real-time PCR (qRT-PCR)

For gene expression quantification, quantitative real-time polymerase chain reaction (qRT-PCR) was performed. For all qRT-PCR experiments, a master mix (10 µL) containing the 5x HOT FIREPol EvaGreen qPCR supermix was prepared for each primer pair representing a different gene of interest (Table 19). The genes of interest and their respective Forward (Fw) and Reverse (Rv) sequences are listed in Table 11. Before use, the primer stocks (pmol/µL) were diluted in a 1:10 ratio in nuclease-free water. cDNA samples were also diluted according

to the initial amount of RNA. All sample reactions were performed in triplicates in a 384-well plate format.

Table 19. Component volumes for a one qRT-PCR reaction

Component	Volume of master mix per single reaction (10 µL)
HOT FIREPol EvaGreen qPCR Supermix	2
Fw primer (1:10)	0.25
Rv primer (1:10)	0.25
Nuclease-free water	7
DNA template (diluted)	0.5

Diluted cDNA samples (2.5 µL/well) were pipetted into a 384-well reaction plate on ice, followed by the addition of the primer pair master mix (7.5 µL/well). Two to three negative controls with nuclease-free water and no cDNA template were included for each gene. A standard curve was also prepared and pipetted for each primer pair by pooling cDNA from all respective samples. Following, the 384-well plate was sealed with an adhesive film and centrifuged at 4°C for 2 min at 2000 rpm. qPCR amplification was then performed using the 7900HT Real-Time PCR System with the settings shown in Table 20 to result in cycle threshold (Ct) values. SYBR was chosen as the detector and ROX (5-carboxy-X-rhodamine) as the passive reference.

Table 20. Standard thermal cycler settings for qRT-PCR analysis

Step		Temperature	Time	No. of cycles
Holding stage	Initial Denaturation	95°C	15 min	1
Cycling stage	Denaturation	95°C	15 sec	40
	Annealing	58°C	20 sec	
	Elongation	72°C	40 sec	
Dissociation stage		95°C	15 sec	1
		60°C	15 sec	
		95°C	15 sec	

Ct values depict when a reaction has reached fluorescent intensity. The Sequence Detection System 7900HT v2.4 software was used to quantify the significant increase in SYBR fluorescence which correlates to the amount of copied DNA templates. The number of copies of the respective RNAs were quantified relative to the number of RNA copies of the housekeeping genes encoding for tubulin beta chain (*TUBB*) and/or β-glucuronidase (*GUSB*).

4.5 Bioinformatics

4.5.1 RNA sequencing

The generation of day 1 and day 5 non-uniform and uniform ECT with Male NF1 hCF for three independent experiments and the subsequent RNA isolation from these ECT was performed by Dr. Gabriela L. Santos before the start of this doctoral project. RNA sequencing was performed by the Transcriptome and Genome Analysis Lab (TAL) in Göttingen, Germany. Upon starting my Ph.D., I contributed significantly to the validation of the RNA sequencing results by performing qPCR for the identified genes between the non-uniform and uniform ECT models.

4.5.2 ECT data adaptation

RNA sequencing data identified 20,847 identity domains (ID) or transcripts between the non-uniform and uniform ECT, including relatively low expressed genes, non-coding RNAs, and pseudogenes. Initial data adaptation was then implemented to identify the differentially expressed genes (DEG) between non-uniform and uniform ECT at day 5. Transcripts that were very low expressed (with a Reads Per Kilobase Million (RPKM) value under 1) were excluded as those would not be seen in a bulk analysis of the heart. The remaining 12,284 ID were adapted similarly to the adaptation of the published data of interest by excluding all non-protein coding RNAs (non-coding RNAs, microRNA, anti-sense) as this set of transcripts might lead to a misinterpretation if it were to remain in the ECT data set. This resulted in 10,588 ID with an RPKM value above one and all protein coding. From these transcripts, the threshold was then adapted to an adjusted p-value or a false discovery rate (FDR) below 0.05 and a log 2-fold change (Log2FC) of ±0.58. With this data adaptation, 1,618 DEG between non-uniform and uniform ECT at day 5 were identified. Stringent unbiased gene ontology (GO) term enrichment was performed using the online analysis tool PANTHER. Representative enriched GO terms, including 100-500 members, were indicated.

4.5.3 ECT data comparison to bulk analysis of diseased human heart data

Following, the 10,588 ID (RPKM≥1, protein-coding) for the ECT data was compared to published transcriptome data sets for normal and diseased human hearts. First, the ECT data was compared to a publication that compared the transcriptomic differences between 7 hypertrophic cardiomyopathy samples and 8 normal heart samples (Ren et al., 2020). This data set was referred to as “hypertrophy” and contained 15,497 ID. From the overlap, 10,079

transcripts were identified. After the statistical thresholds were applied (FDR<0.05, Log2FC±0.58), 1,655 hypertrophy DEG were identified. Additionally, the ECT data was compared to another meta-analysis of 16 comprehensive transcriptomic studies that compared healthy and failing human hearts (Flores et al., 2021). This data set was referred to as "heart failure" and contained 14,041 transcripts. From the overlap, 9,871 transcripts were identified. After the statistical thresholds were applied (FDR<0.05, Log2FC±0.5), 3,129 heart failure DEG were identified. The overlap in DEG between the three groups was assessed, and stringent unbiased GO term enrichment was performed using PANTHER.

4.5.4 ECT data adaptation for comparison to single-cell RNA sequencing of MI mice models

The ECT data was additionally compared to published single-cell sequencing data of a MI model in mice (Farbehi et al., 2019), which is further described in the Introduction (1.5). As single-cell sequencing is very different from bulk RNA sequencing, initial data adaptation was once again adjusted to a lower Log2FC to allow for the identification of highly expressed genes between both types, as the sequencing depth of single-cell sequencing is between 1,000-4,000 genes, whereas bulk RNA sequencing has a depth of apporximately10,000 genes. Therefore, the 10,588 ID (RPKM≥1, protein-coding) from the ECT data set was adapted to an FDR below 0.05 and a Log2FC of ±0.5. After data adaptation, 2,164 DEG between non-uniform and uniform ECT at day 5 were identified. The DEG for all fibroblast subpopulations that the publication described versus Fibroblast-Sca1-low (F-SL) and Fibroblast-Sca1-high (F-SH) resulted in 965 DEG. When the same statistical threshold (FDR<0.05, Log2FC±0.5) was applied, 277 DEG were identified for the MI models in mice. Following, the overlap between individual fibroblast subpopulations described in the publication (Fibroblast-activated; F-Act, Fibroblast-cycling; F-Cyc, and Myofibroblast; F-Myo) was compared with the ECT data set and enriched GO terms were identified using PANTHER.

4.6 Statistical analysis

Data are presented as mean ± SEM. Statistical analysis was performed using 1- or 2-way ANOVA assessed by Tukey's and Dunnett's *post hoc* multiple comparison tests when comparing more than two groups. Otherwise, pairwise group comparison was performed using two-tailed unpaired t-test assuming normal distribution. A value of $p<0.05$ was considered statistically significant. Statistical calculations were performed with GraphPad Prism v8 or 9.

5 Results

5.1 Validation and identification of differences between non-uniform and uniform ECT with hCF from different donors

The interplay between cardiac fibroblast phenotype adaptation and mechanical stress in the course of heart disease is still poorly understood. As previously mentioned, our group has established ECT models with different geometries to further elucidate this interplay. However, the models were established and characterized with hCF from only one male donor who died from a different cause other than cardiovascular disease (Male Normal Fibroblast 1; Male NF1). Therefore, one primary aim of this thesis was to validate the models with hCF from different donors with and without heart disease and of different sex. Moreover, by using different donors, shared relationships between different analyzed parameters should be established, which helps to gain more insight into the biology of hCF. Therefore, hCF from 9 different donors (Male NF1, Male Normal Fibroblast 2; Male NF2, Female Normal Fibroblast 1; Female NF1, Female Normal Fibroblast 2; Female NF2, Female Normal Fibroblast 3; Female NF3, Male Ischemic Cardiomyopathy 1; Male ICM1, Male Ischemic Cardiomyopathy 2; Male ICM2, Male Dilated Cardiomyopathy 1; Male DCM1, and Male Dilated Cardiomyopathy 2; Male DCM2) were included in this detailed analysis. All donors were Caucasian, and their ages ranged from 31 to 60 years. Included were hCF from three female and two male donors without heart disease and four male donors with end-stage heart failure, two with ICM and two with DCM (Figure 5A).

5.1.1 2D-cultured hCF from diseased hearts show a slower proliferation and larger cell size

An initial basal analysis of the 2D-cultured hCF from normal and diseased hearts was performed based on cell size, doubling times, and age of donor to better understand parameter correlations. hCF from diseased hearts appeared to be bigger and proliferated slower, independent of the donor age (Figure 5B, C). Accordingly, when analyzed according to their cell diameters in suspension versus their doubling times, hCF from healthy and diseased hearts formed two distinct clusters (Figure 5D). As the doubling times for each donor cell line were given by the different companies, proliferation assays were also performed for hCF from Male NF1, Male NF2, Female NF1, Female NF2, Female NF3, Male ICM1, and Male DCM1 to ensure that information aligns with the precise handling during the experiments presented in

this thesis. In line with the information provided by the companies, the diseased cells proliferated slower (Figure 5E).

A

Caucasian primary hCF donors			
Health Status	Abbreviation	Company	Age
Male Normal Fibroblast 1	**M NF1**	Lonza	52
Male Normal Fibroblast 2	**M NF2**	Lonza	46
Female Normal Fibroblast 1	**F NF1**	Lonza	60
Female Normal Fibroblast 2	**F NF2**	Lonza	32
Female Normal Fibroblast 3	**F NF3**	Lonza	31
Male Ischemic Cardiomyopathy 1*	**M ICM1**	PromoCell	55
Male Ischemic Cardiomyopathy 2*	**M ICM2**	PromoCell	58
Male Dilated Cardiomyopathy 1	**M DCM1**	PromoCell	48
Male Dilated Cardiomyopathy 2#	**M DCM2**	PromoCell	56

*comorbidities: Diabetes mellitus type 2, hypertension
#comorbidity: hypertension

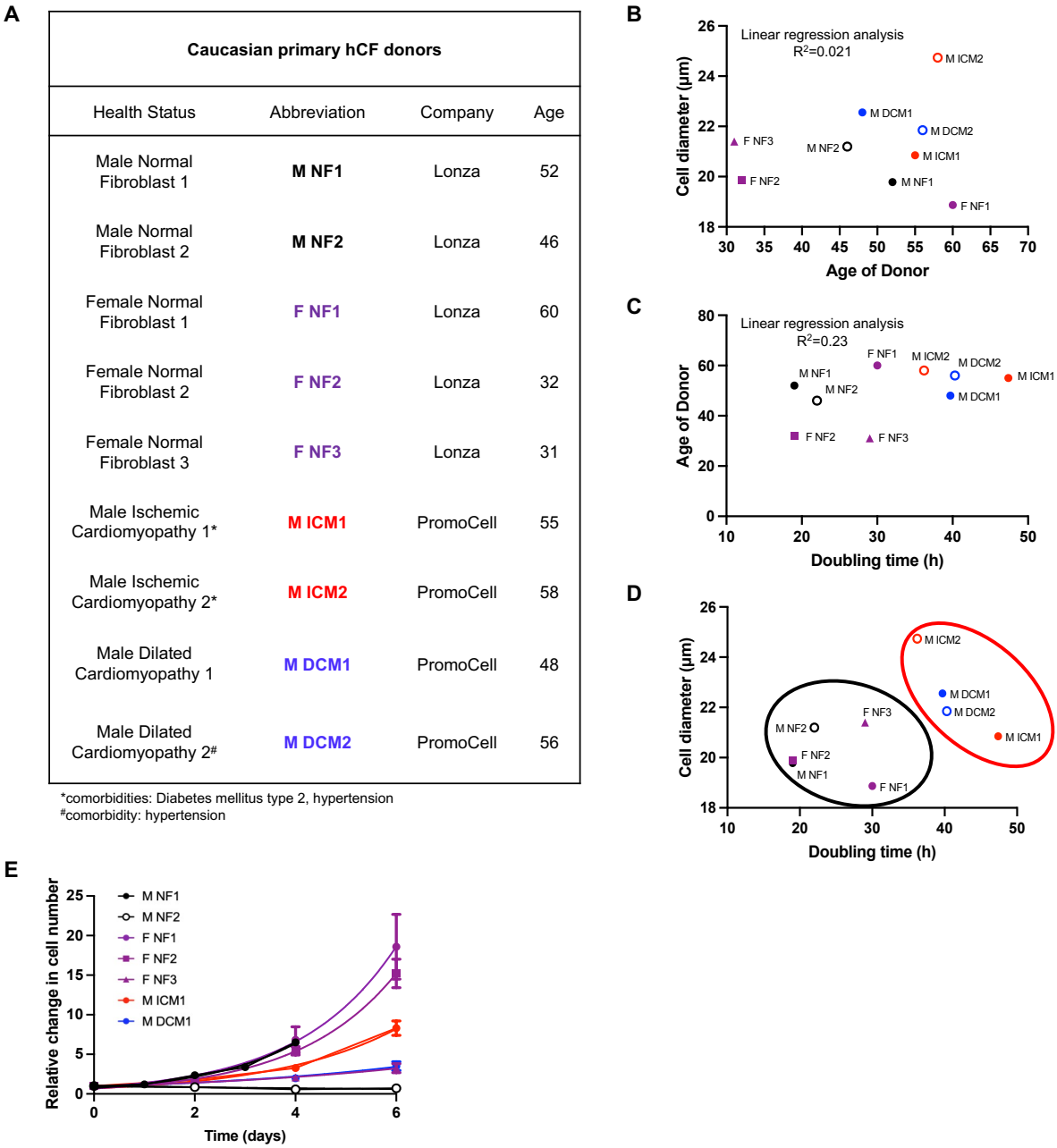

Figure 5. Characterization of 2D-cultured hCF from normal and diseased hearts. A) Human ventricular cardiac fibroblasts (hCF) from 9 different donors in total (age 31-60 years, all Caucasian), including two from normal male hearts; M NF1, M NF2, three from normal female hearts; F NF1, F NF2, F NF3, and four from explanted male hearts with end-stage heart failure; M ICM1, M ICM2 and M DCM1, M DCM2, were cultured in 2D. All cells were purchased from Lonza or PromoCell, cultured in FGM-3 medium (PromoCell), and usually expanded up to passage 4. Linear correlation analyses between **B**) cell diameter and age of donor, **C**) age of donor and doubling time, and **D**) cell diameter and doubling time are shown. **E**) hCF from M NF1, M NF2, F NF1, F NF2, F NF3, M ICM1, and M DCM1 were cultured for up to 4 or 6 days in 2D. Cell proliferation was assessed by automated counting of DAPI-stained nuclei and baseline-corrected from at least 3 independent experiments in 4 technical replicates each, means±SEM.

5.1.2 Characterization of ECT generated with normal and diseased hCF after 5 days in culture

5.1.2.1 Cell size of hCF negatively correlates to ECT compaction

As demonstrated by Dr. Santos and described in the Preliminary results (2), ECT with distinct morphometric and biomechanical properties could be obtained by using different mold geometries. One observed difference was related to the compaction of the ECT reflected by the CSA. In the uniform model, ECT compaction was more pronounced than in the non-uniform model when hCF from the male donor without heart disease (Male NF1) were used.

In this thesis, non-uniform and uniform ECT were generated with hCF from all nine donors under comparable conditions, and the CSA were determined after 5 days in culture. In all donors besides Male ICM2, ECT generated with the uniform model were significantly more compact than in the non-uniform model (Figure 6A). Furthermore, the CSA for both non-uniform and uniform ECT from all donors showed a linear correlation with the cell size, which was especially prominent in the non-uniform model (non-uniform: R^2=0.87, uniform R^2=0.69) (Figure 6B, C).

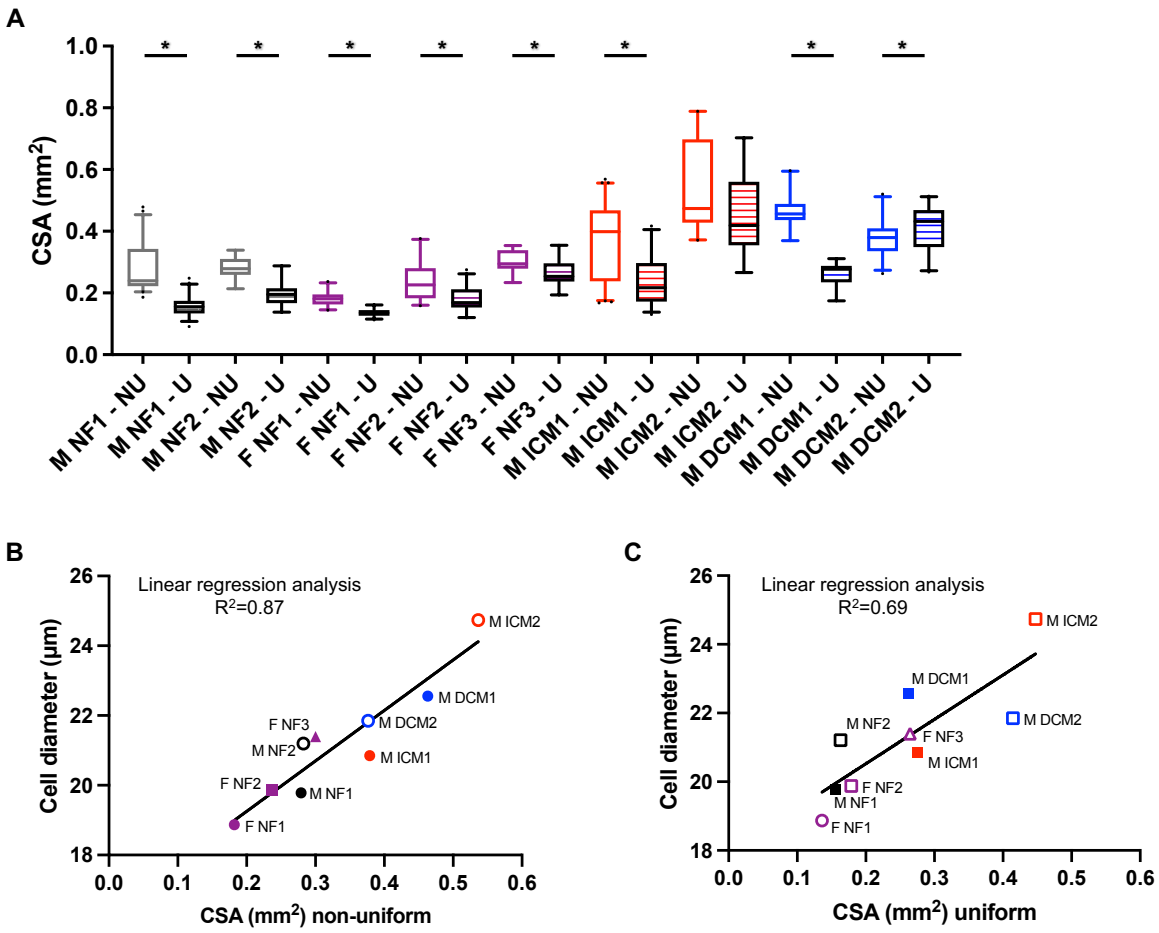

Figure 6. The geometry of the mold influences the morphometrical properties of ECT. 2D-cultured hCF from M NF1, M NF2, F NF1, F NF2, F NF3, M ICM1, M ICM2, M DCM1, and M DCM2 were used to generate non-uniform (NU) and uniform (U) ECT, then cultured for 5 days. **A**) Macroscopic images were used to estimate the cross-sectional areas (CSA) of the non-uniform and uniform ECT. The values are presented as box plots with 5-95 percentile whiskers, n=15-44 from at least 3 independent experiments, $^{*}p<0.05$ assessed by unpaired t-test. Cell diameters were determined in passage 4 using electronic current exclusion and pulse field analysis for each donor before ECT generation. Linear correlation analyses of the cell diameters and CSA are shown for **B**) non-uniform and **C**) uniform ECT.

5.1.2.2 Longitudinal contraction of non-uniform ECT is highly individual and does not correlate to cell size or ECT compaction

Longitudinal ECT contraction was assessed by measuring the pole deflection of non-uniform ECT. Surprisingly, contraction between the donors showed no common contractile properties and ranged from almost no contraction with 2% (Male DCM2) to 22.25% (Female NF1) over the course of 5 days. High variance in pole deflection was seen, especially for ECT generated with the normal female cells (2.2-22.25%), whereas the two normal male donor cells produced ECT with almost identical ECT contraction with 8.6% (Male NF1) and 8.1% (Male NF2). The most significant variance compared to the control was observed in the male cohort for Male ICM2 (17.5%) and Male DCM2 (1.9%) ECT (Figure 7A).

Although tissue compaction and contraction are both actin-dependent processes, and cell size was strongly correlated to ECT compaction for almost all hCF donors, there was no significant correlation between cell size and ECT contraction (R^2=0.0017) (Figure 7B). Accordingly, compaction of the non-uniform ECT did not correlate with ECT contraction at day 5 (R^2=0.00043) (Figure 7C).

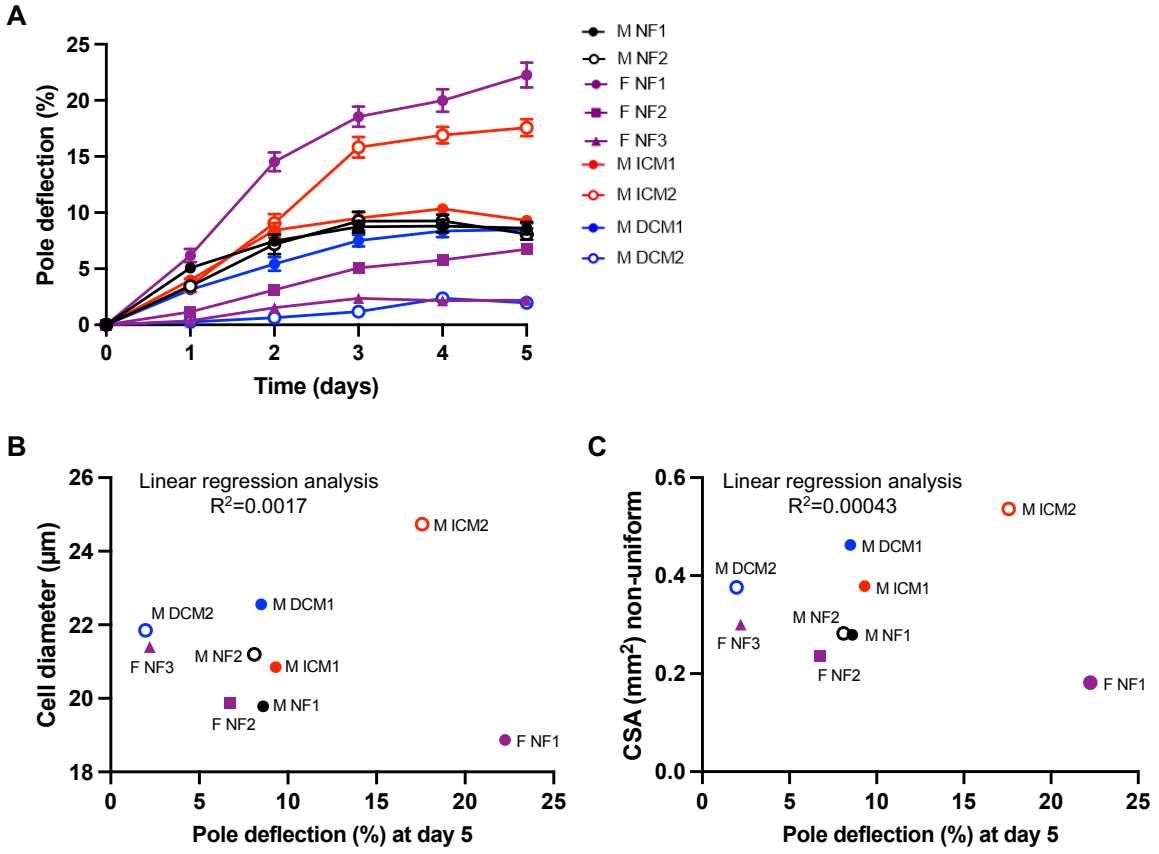

Figure 7. Variance in ECT contractile behavior regardless of normal or diseased cell state. 2D-cultured hCF from M NF1, M NF2, F NF1, F NF2, F NF3, M ICM1, M ICM2, M DCM1, and M DCM2 were used to

generate non-uniform ECT. **A**) Pole deflection was measured over the course of 5 days, n=21-104 from 3 independent experiments, means±SEM. Non-linear correlations between **B**) the cell diameter and pole deflection at day 5 and **C**) the CSA of non-uniform ECT and pole deflection at day 5 are shown.

5.1.2.3 Negative linear correlation between ECT stiffness and extensibility

Biomechanical properties were measured by a dynamic mechanical approach. Several important parameters could be identified from the obtained stress-strain curves. First, the Young's modulus, which defines the stiffness of the ECT, was compared. The data showed that all cells reacted to the geometry of the uniform model by producing significantly stiffer ECT than in the non-uniform model (Figure 8A). The mean difference in stiffness for non-uniform ECT ranged from 14-45 kPa, while uniform ECT ranged from 47-124 kPa. To compare the absolute mean stiffness between conditions, data for ECT with similar donor cells were combined (Male NF: Male NF1 and Male NF2; Female NF: Female NF1, Female NF2, and Female NF3; Male ICM: Male ICM1 and Male ICM2; Male DCM: Male DCM1 and Male DCM2). With respect to the absolute mean stiffness between similar conditions, non-uniform and uniform Male ICM ECT were less stiff when compared to non-uniform and uniform of both Male NF and Male DCM ECT. Furthermore, non-uniform Male NF ECT were less stiff than non-uniform Female NF ECT (Figure 8B).

Another informative parameter that was extracted from the stress-strain curve is extensibility, referring to the ultimate strain in which the ECT can endure before rupture. All cells also reacted to the geometry of the uniform model by producing significantly less extensible ECT when compared to their respective non-uniform ECT (Figure 8C). When combining data for ECT with similar donor cells and comparing the absolute mean extensibility, non-uniform Male DCM ECT were less extensible than Male NF and Male ICM ECT. Uniform Male DCM ECT were less extensible when compared to Male ICM ECT; however, Male ICM ECT were more extensible than Male NF ECT. There was no change in extensibility between Male NF and Female NF ECT (Figure 8D). A semi-logarithmic correlation was found when comparing the stiffness of all ECT with their extensibility (Figure 8E), indicating that stiffness and extensibility are clearly negatively correlated. Therefore, the stiffer the ECT are, the less strain resistant they are.

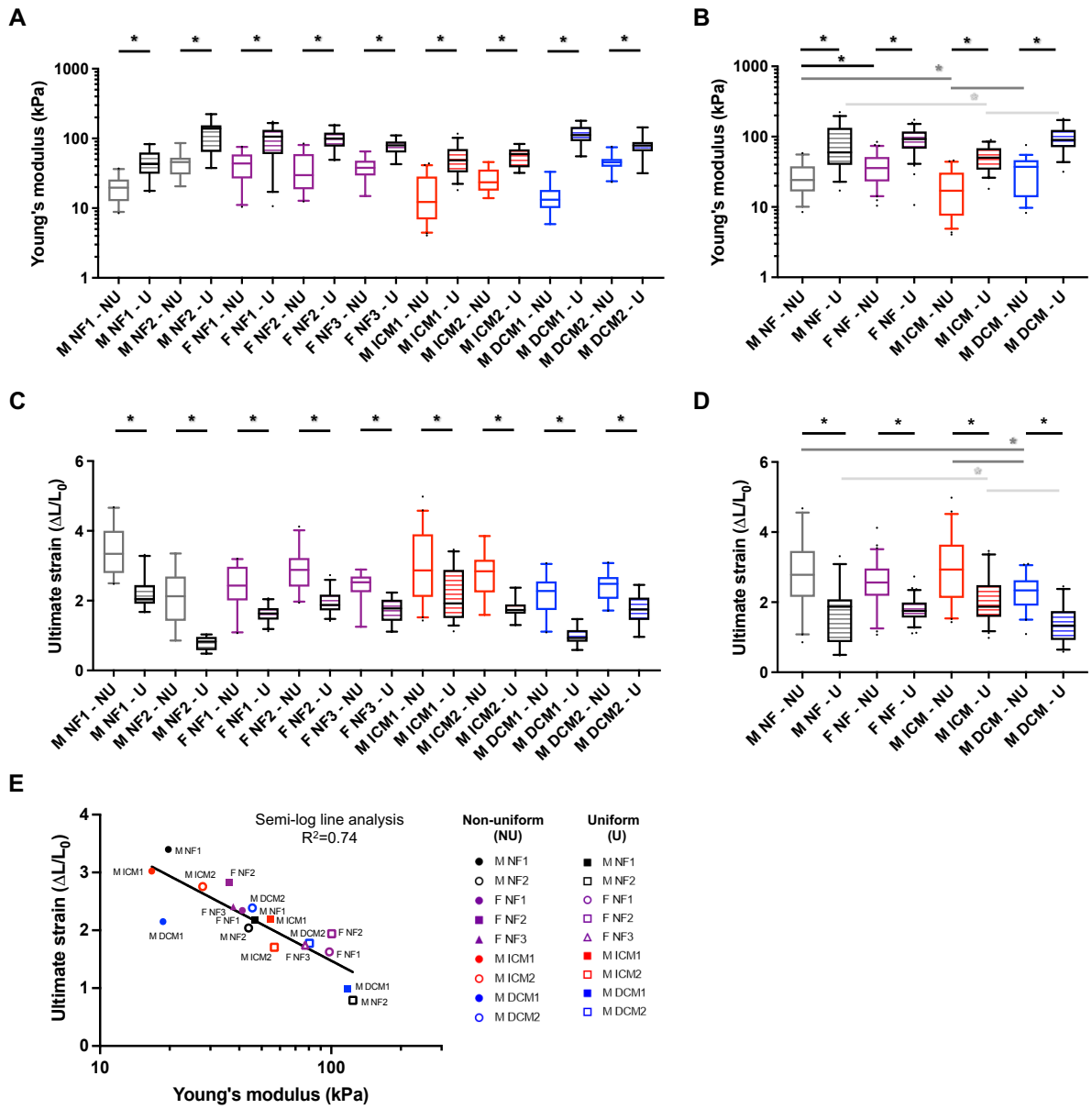

Figure 8. The geometry of the mold dictates the biomechanical properties of the ECT. 2D-cultured hCF from M NF1, M NF2, F NF1, F NF2, F NF3, M ICM1, M ICM2, M DCM1, and M DCM2 were used to generate non-uniform (NU) or uniform (U) ECT. Biomechanical properties were determined by dynamic mechanical analysis after 5 days of culture. **A**) The individual Young's moduli values for each donor (n=15-42) or **B**) combined Young's moduli values for similar donors (n=33-71) are shown. The values are presented as box plots with 5-95 percentile whiskers from at least 3 independent experiments, *p<0.05 assessed by unpaired t-test (black) or by group-wise (NU - dark gray) or (U - light gray) 1-way-ANOVA with Tukey's *post hoc* multiple comparisons test. **C**) Likewise, the individual ultimate strain values for each donor (n=14-42) or **D**) combined ultimate strain values for similar donors (n=33-71) are shown. The values are presented as box plots with 5-95 percentile whiskers from at least 3 independent experiments, *p<0.05 assessed by unpaired t-test (black) or by group-wise (NU - dark gray, U - light gray) 1-way-ANOVA with Tukey's *post hoc* multiple comparisons test. **E**) A semi-logarithmic correlation between the Young's moduli and the ultimate strains is shown.

5.1.3 Mold geometry dictates morphological and biomechanical properties of ECT

Distinct differences between the non-uniform and uniform ECT after 5 days have been identified above. To better understand if the mold's geometry or the material properties' hardness influences the morphological and biomechanical properties of the ECT, materials with varying characteristics (Table 16) for both models were compared for the Female NF1 donor. Our group has also shown this comparison for the Male NF1 donor with similar results (Santos et al., 2022). For non-uniform ECT, a 48-well plate was used either with an insert containing two flexible poles (TM5, shore value A 46) that allowed for passive contraction or a self-printed insert containing two stiff poles with a spacer (MED610 with spacer, shore value D 83-86) that did not allow for passive contraction. For uniform ECT, self-prepared molds were used with inserts of central rods made from versilic (shore value A 62), Z-dupe silicone (shore value A 15), or 0.75% agarose (shore value 00 15-25). After 5 days in culture, ECT compaction showed no difference between the non-uniform ECT generated from the same geometry but different material properties. Both non-uniform TM5 and non-uniform MED610 with spacer were less compact than uniform 0.75% agarose and uniform A62. However, only non-uniform TM5 was less compact than uniform silicone A15. Uniform silicone A15 ECT were less compact when compared to uniform 0.75% agarose and uniform A62 (Figure 9A). Regarding ECT stiffness, both non-uniform TM5 and MED610 with spacer ECT were significantly less stiff when compared to all uniform ECT. There were no differences in stiffness between the different uniform ECT (Figure 9B). Taken together, the geometry of the mold, rather than the hardness of the materials properties, strongly influenced the morphological and biomechanical properties of the ECT.

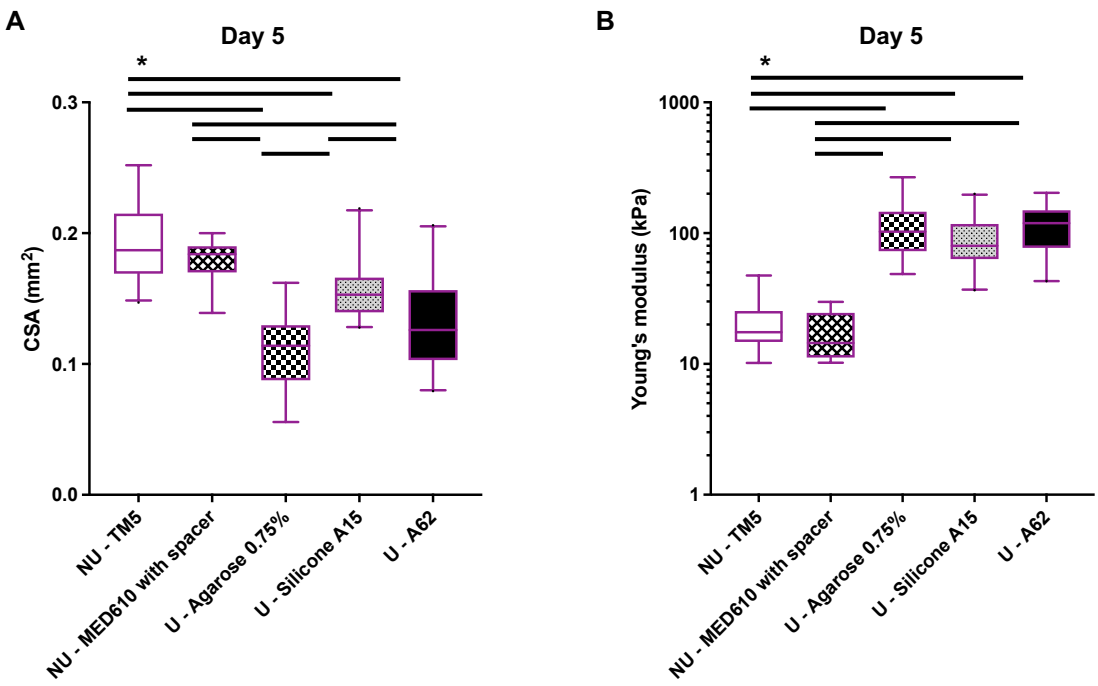

Figure 9. Geometry of molds dictates morphological and biomechanical properties of ECT. 2D-cultured hCF from F NF1 were used to generate non-uniform (NU) or uniform (U) ECT. NU ECT were generated by using molds with two flexible poles (TM5) or two stiff poles with a spacer (MED610 with spacer). U ECT were generated by using molds with a single central rod made of 0.75% agarose (Agarose 0.75%), soft silicone with a shore value of A15 (silicone A15), or silicone with a shore value of A62 (A62). **A**) The CSA of the ECT were estimated and the values are presented as box plots with 5-95 percentile whiskers, n=15-27 from 1-3 independent experiments, $^{*}p<0.05$ assessed by 1-way-ANOVA with Tukey's *post hoc* multiple comparisons test. **B)** Biomechanical properties were determined, and the Young's moduli values are presented as box plots with 5-95 percentile whiskers, n=10-20 from 1-3 independent experiments, $^{*}p<0.05$ assessed by 1-way-ANOVA with Tukey's *post hoc* multiple comparisons test.

5.1.4 Replicative exhaustion exemplifies the effect of biological age on ECT properties

As substantial differences were seen between Female NF1 and Female NF3 donors regarding cell size, proliferation, and ECT contraction, the effect of a cell's biological age on these parameters was investigated by replicative exhaustion. Cells in higher passages, or senescent cells, have been shown to be bigger in size (Muggleton-Harris & Hayflick, 1976; Yang et al., 2011). When culturing the 2D cells to passage 4 (P 4), cells from Female NF1 were smaller than Female NF3 cells. Therefore, replicative exhaustion demonstrated that Female NF1 cells in P 8 were required to reach the size of Female NF3 cells in P 4 (Figure 10A). After replicating the Female NF1 cells to exhaustion by P 8, the cells were used to generate non-uniform ECT to assess compaction and contraction after 5 days. Female NF1 ECT generated with P 8 cells were significantly less compact than Female NF1 ECT generated with P 4 cells (Figure 10B). In line with this data, the reduction in compaction of Female NF1 ECT generated with P 8 cells

was similar to Female NF3 ECT generated with P 4 cells. Pole deflection analysis showed that Female NF1 - P 8 ECT still contracted similarly to Female NF1 - P 4 ECT until day 4, with a significant decrease in contraction at day 5. However, contraction of Female NF1 - P 8 ECT never reached a similar level as Female NF3 - P 4 ECT (Figure 10C). Additionally, gene expression of thymocyte differentiation antigen 1 (*THY1* gene) was investigated after 5 days in culture, as it has been shown to be a myofibroblast marker (Rao et al., 2021). *THY1* expression in Female NF3 - P 4 ECT was higher than Female NF1 ECT from both P 4 and P 8 cells (Figure 10D). In sum, the biological age of the cell does play a role in ECT compaction; however, replicative exhaustion was not sufficient to significantly effect ECT contraction or *THY1* expression.

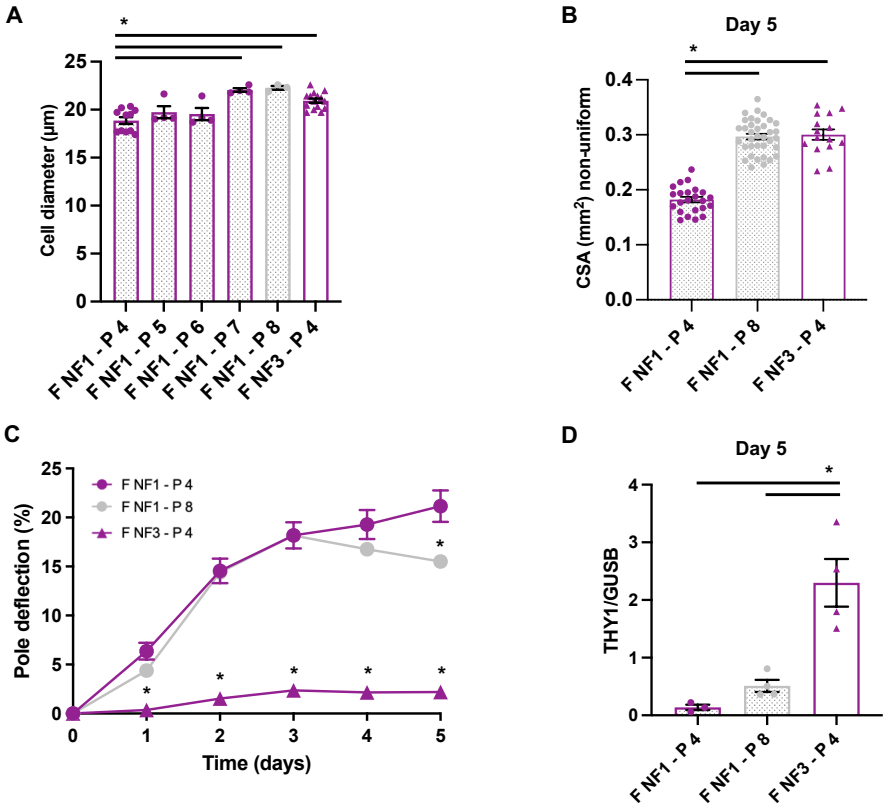

Figure 10. Influence of the replicative age of hCF on ECT properties. A) Cell diameter was determined in passage 4-8 by using electronic current exclusion and pulse field analysis before ECT generation. Cell diameter at passage 4 and passage 8 are shown, n=3-15 from 3 independent experiments, means±SEM, *p<0.05 by 1-way-ANOVA with Tukey's *post hoc* multiple comparisons test. **B)** CSA of non-uniform ECT generated with hCF in passage 4 and passage 8 are shown, n=15-33 from 3 independent experiments, means±SEM, *p<0.05 by 1-way-ANOVA with Tukey's *post hoc* multiple comparisons test. **C)** Pole deflection was measured for non-uniform ECT casted with hCF in passage 4 and passage 8 over the course of 5 days, n=36-62 from at least 3 independent experiments, means±SEM, *p<0.05 by 2-way-ANOVA with Tukey's *post hoc* multiple comparisons test. **D)** RNA was isolated from F NF1 or F NF3 non-uniform ECT generated with passage 4 or passage 8 hCF. qPCR analysis of *THY1* was performed for 3-4 individual experiments for each donor. All qPCR values were normalized to the mean of the housekeeping gene *GUSB*, means±SEM, *p<0.05 by 1-way-ANOVA with Tukey's *post hoc* multiple comparisons test.

5.1.5 Characterization of ECT generated with normal and diseased hCF after 13 days in culture

As previously shown, ECT generated with hCF from different donors and cast in non-uniform or uniform molds showed a linear correlation between ECT compaction and cell size, and a negative correlation between stiffness and extensibility after 5 days in culture. Therefore, these correlations were also investigated for hCF from 6 of the 9 different donors (Male NF2, Female NF1, Female NF2, Male ICM1, Male DCM1, and Male DCM2) after culturing the ECT for up to 13 days.

5.1.5.1 Prolonged culture allows for further compaction of ECT and consistent correlation with cell size

In all investigated donors, ECT generated with the uniform model were significantly more compact than in the non-uniform model (Figure 11A). In line with the day 5 data, a linear correlation between cell diameter and compaction of the ECT was still seen even after 13 days in culture. However, the correlation between these parameters was not as strong as after 5 days (non-uniform: R^2=0.74, uniform R^2=0.49) (Figure 6B, C; Figure 11B, C).

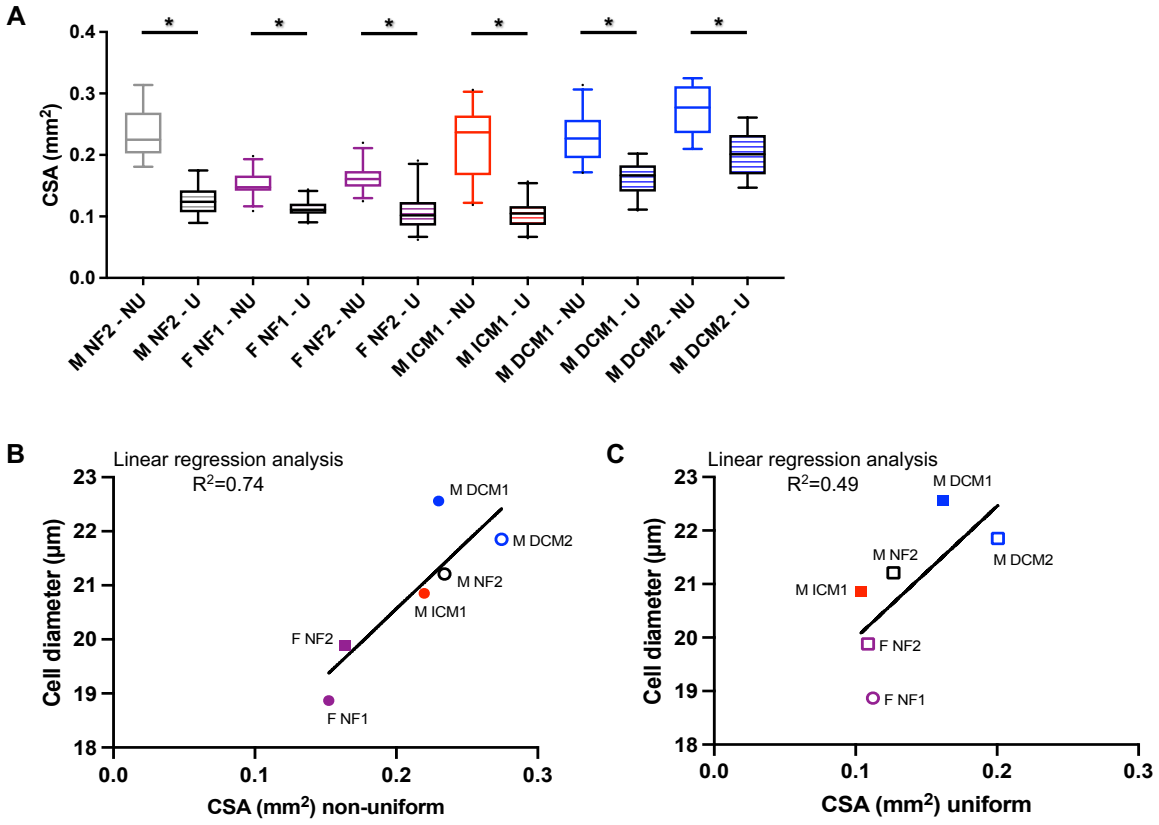

Figure 11. Further compaction of ECT upon prolonged culture. 2D-cultured hCF from M NF2, F NF1, F NF2, M ICM1, M DCM1, and M DCM2 were used for generation of ECT and casted in non-uniform (NU) or

uniform molds (U), then cultured for 13 days. **A)** Macroscopic images were used to estimate the CSA of the NU and U ECT. The values are presented as box plots with 5-95 percentile whiskers, n=5-34 from 1-3 independent experiments, $^{*}p<0.05$ assessed by unpaired t-test. Cell diameter was determined in passage 4 using electronic current exclusion and pulse field analysis for each donor before ECT generation. Linear correlation analyses of the cell diameter and CSA are shown for **B)** non-uniform and **C)** uniform ECT.

5.1.5.2 Longitudinal contraction of non-uniform ECT demonstrates that there is no steady state reached after prolonged culture

Pole deflection of non-uniform ECT was measured over the course of 13 days. Both normal and diseased male ECT peaked between days 3-4 and subsequently showed a slight decline in contraction between days 4-5. After day 5, most normal and diseased male ECT contraction remained consistent throughout the remainder of the culture period. However, Male ICM1 behaved quite differently after day 7 (9.34%), with inducing contraction more than twice by day 13 (23.58%). Female NF2 increased contraction gradually over the duration of culture. In contrast, Female NF1 showed a sharp increase in contraction within the first 3 days and continued to increase contraction consistently until day 13 (Figure 12A).

Interestingly, cell size and ECT contraction (R^2=0.41), as well as compaction of non-uniform ECT and contraction (R^2=0.27), showed a stronger correlation after 13 days when compared to day 5 (Figure 7B, C; Figure 12B, C).

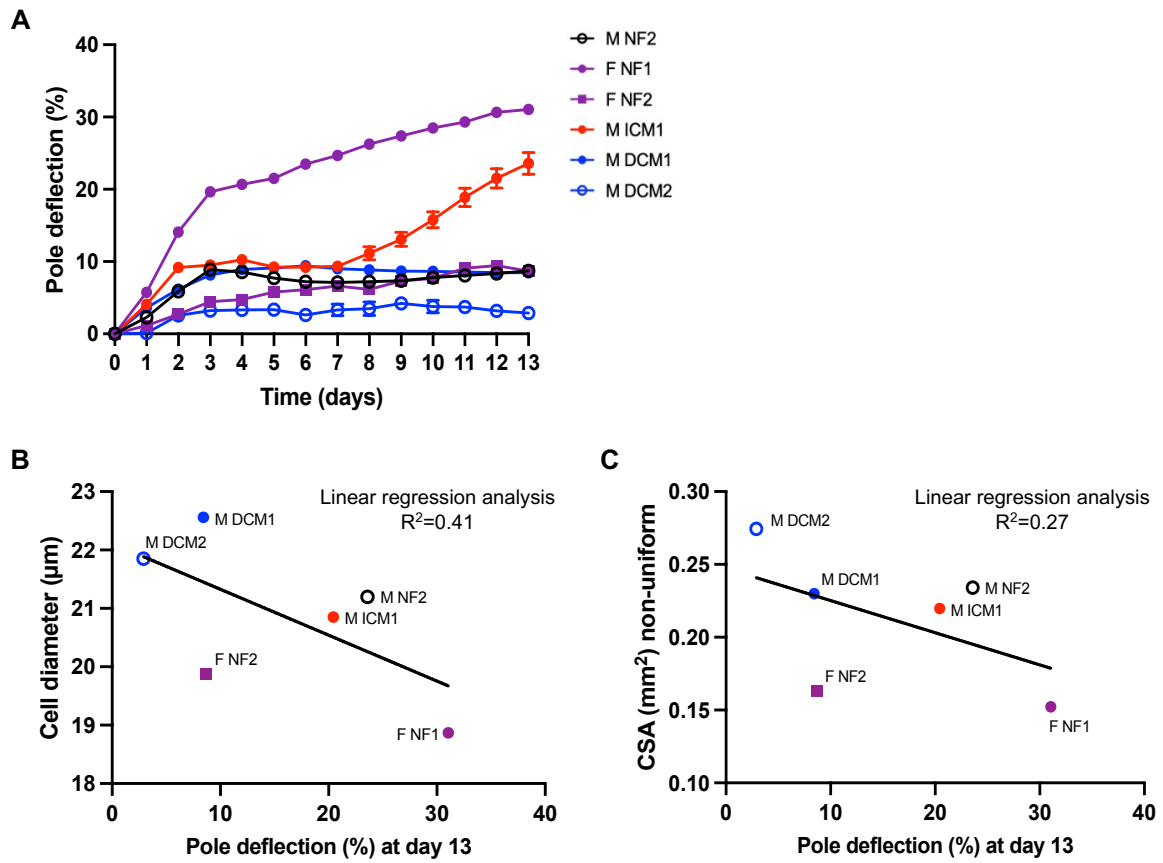

Figure 12. No steady state in ECT reached upon prolonged culture. 2D-cultured hCF from M NF2, F NF1, F NF2, M ICM1, M DCM1, and M DCM2 were used to generate non-uniform ECT. **A)** Pole deflection was measured over the course of 13 days, n=6-80 from 1-3 independent experiments, means±SEM. Linear correlations between **B)** the cell diameter and pole deflection at day 13 and **C)** the CSA of non-uniform ECT and pole deflection at day 13 are shown.

5.1.5.3 Prolonged culture of non-uniform and uniform ECT results in increased stiffness and lower extensibility

In line with the day 5 data, all cells once again reacted to the geometry of the uniform model by producing significantly stiffer ECT than in the non-uniform model within 13 days (Figure 13A). The final stiffnesses of all ECT were higher when compared to day 5. The mean difference in stiffness for non-uniform ECT ranged from 37-126 kPa, while uniform ECT ranged from 88-300 kPa. Absolute mean stiffness between conditions (Male NF2; Female NF: Female NF1, Female NF2, and Female NF3; Male ICM1, and Male DCM: Male DCM1 and Male DCM2) showed that non-uniform Male ICM1 and Male DCM ECT were less stiff when compared to non-uniform Male NF2 ECT. Uniform Male DCM ECT were less stiff when compared to uniform Male NF2 and Male ICM1 ECT. Non-uniform and uniform Female NF ECT were stiffer than Male NF2 ECT in both cases (Figure 13B).

Regarding extensibility, the influence of the geometry was preserved over the 13 days, resulting in lower extensibility of uniform ECT when compared to their respective non-uniform counterparts. Overall, all conditions showed less extensible ECT after 13 days when compared to day 5 ECT (Figure 13C). Uniform Male ICM1 ECT were less extensible than Male DCM ECT. In line with the stiffness data, non-uniform and uniform F NF ECT were also less extensible than Male NF2 ECT (Figure 13D).

After 13 days, a semi-logarithmic correlation was also found when comparing the stiffness of all ECT with their extensibility (Figure 13E).

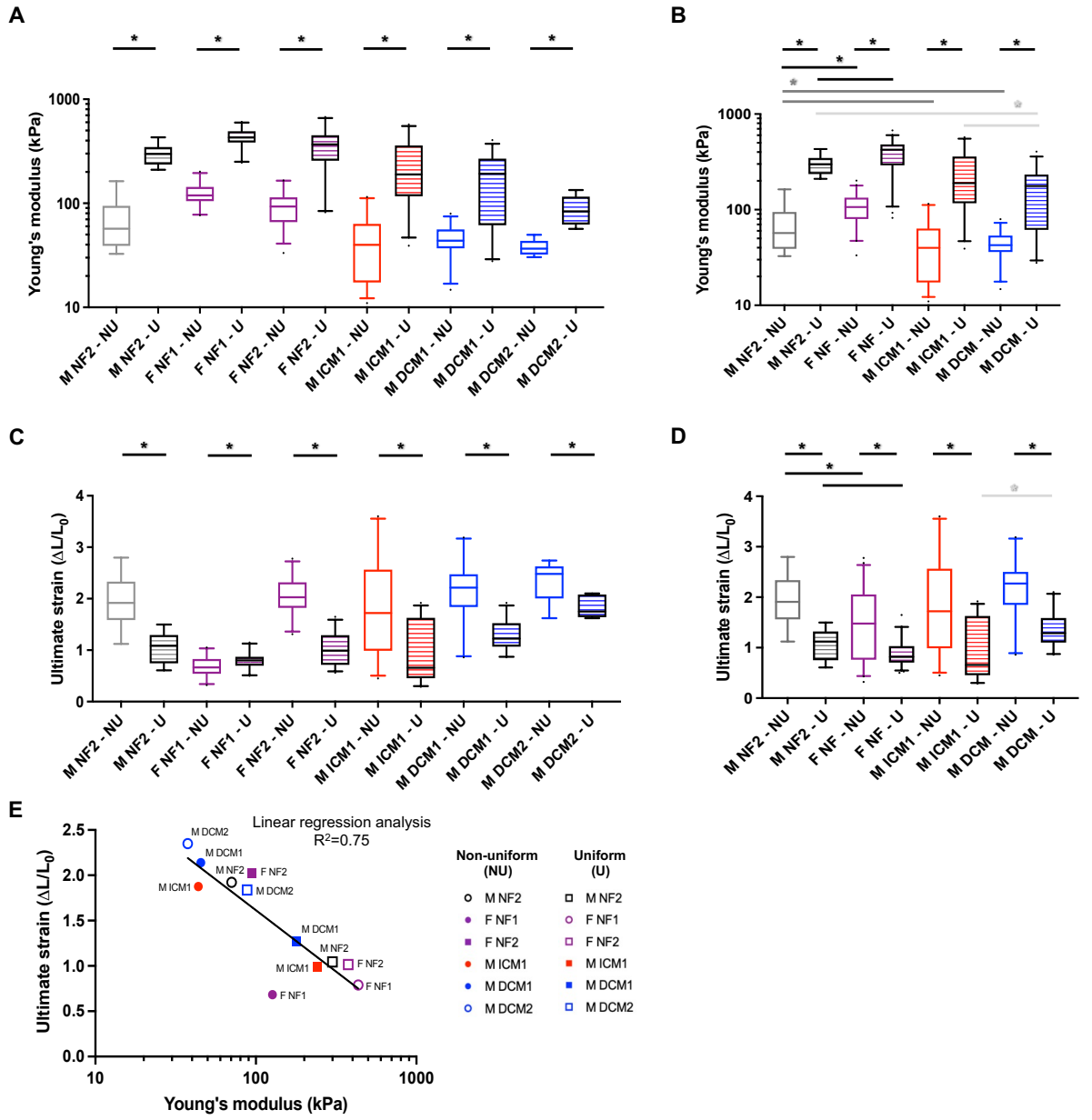

Figure 13. Increased stiffness and lower extensibility of ECT upon prolonged culture. 2D-cultured hCF from M NF2, F NF1, F NF2, M ICM1, M DCM1, and M DCM2 were used to generate non-uniform (NU) or uniform (U) ECT. Biomechanical properties were determined by a dynamic mechanical analysis after 13 days of

culture. **A)** The individual Young's moduli values for each donor (n=5-32) or **B)** combined Young's moduli for similar donors (n=18-55) are shown. The values are presented as box plots with 5-95 percentile whiskers from 1-3 independent experiments, $^{*}p<0.05$ assessed by unpaired t-test (black) or by group-wise (NU - dark gray) or (U - light gray) 1-way-ANOVA with Tukey's *post hoc* multiple comparisons test. **C)** Likewise, the individual ultimate strain values for each donor (n=5-32) or **D)** combined ultimate strain values for similar donors (n=18-55) are shown. The values are presented as box plots with 5-95 percentile whiskers from 1-3 independent experiments, $^{*}p<0.05$ assessed by unpaired t-test (black) or by group-wise (NU - dark gray) or (U - light gray) 1-way-ANOVA with Tukey's *post hoc* multiple comparisons test. **E)** A semi-logarithmic correlation between the Young's moduli and the ultimate strains is shown.

5.1.6 The uniform geometry mold elicits a pro-fibrotic gene signature in normal and ICM cells, but not DCM cells, after 5 days

Differences in gene expression for normal and diseased ECT were also investigated to identify if the cells respond similarly to the different mold geometries. Both Male and Female NF ECT, as well as Male ICM ECT showed a higher transcription of *ACTA2*, *COL1A1*, *POSTN*, and *THBS1* in the uniform model. In contrast, Male DCM ECT did not result in a higher transcription of *ACTA2*, *COL1A1*, *POSTN*, and *THBS1* to the uniform mold geometry. Furthermore, Male DCM ECT demonstrated a significantly higher *COL1A1* and *LUM* expression in non-uniform model when compared to non-uniform ECT generated with Male NF and Male ICM hCF. *POSTN* expression in non-uniform Male DCM ECT was also higher in comparison to non-uniform Male NF ECT. *TCF21* was unchanged for all donor cells (Figure 14).

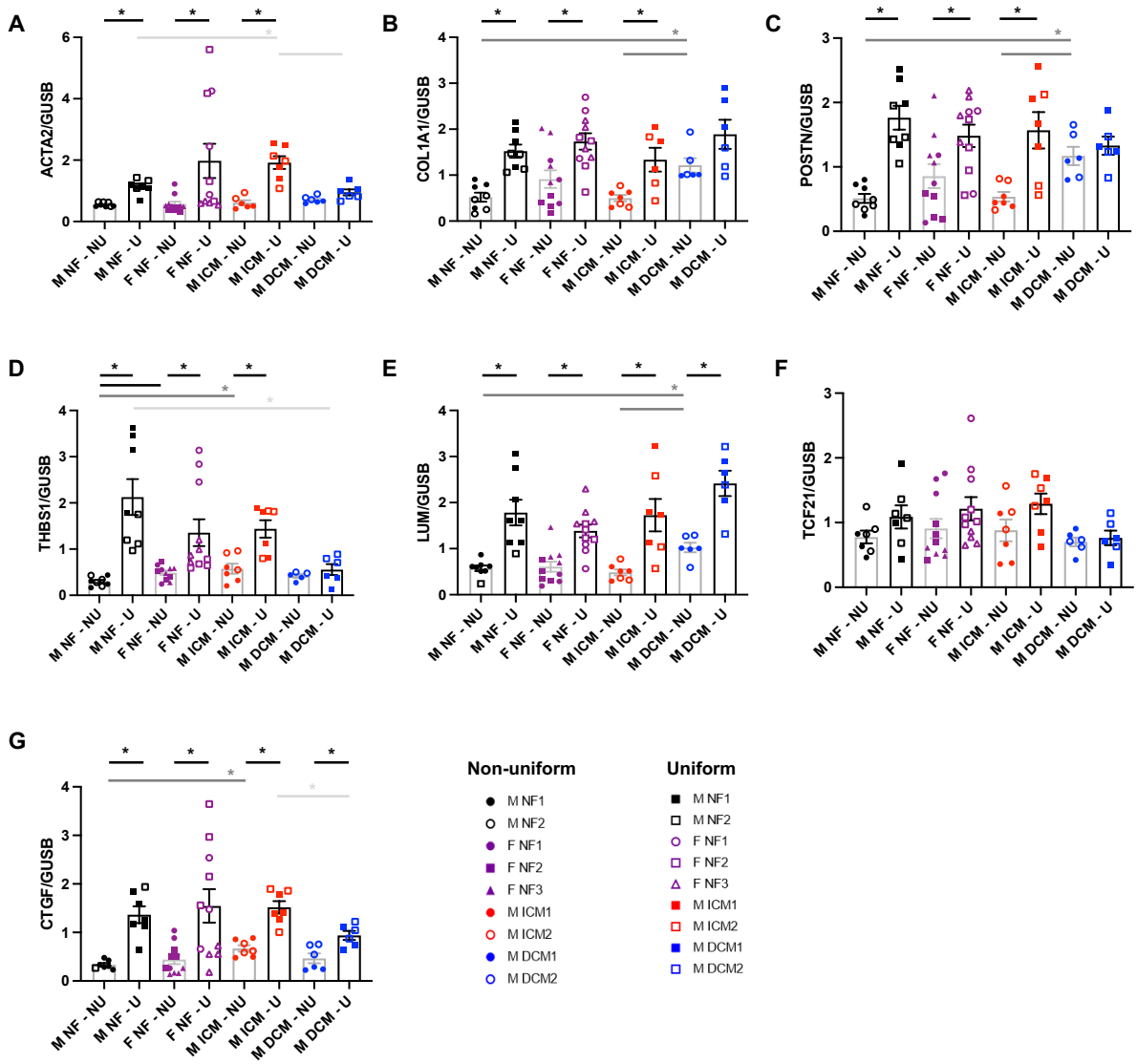

Figure 14. Geometry- and donor-dependent regulation of gene expression in ECT. 2D-cultured hCF from M NF1, M NF2, F NF1, F NF2, F NF3, M ICM1, M ICM2, M DCM1, and M DCM2 were used to generate non-uniform (NU) or uniform (U) ECT. RNA was isolated after 5 days of culture and qPCR analysis of **A)** *ACTA2*, **B)** *COL1A1*, **C)** *POSTN*, **D)** *THBS1*, **E)** *LUM*, **F)** *TCF21*, and **G)** *CTGF* was performed for 3-4 individual experiments for each donor. All qPCR values were normalized to the mean of the housekeeping gene *GUSB*, means±SEM, *p<0.05 assessed by unpaired t-test (black) or by group-wise (NU - dark gray, U - light gray) 1-way-ANOVA with Tukey's *post hoc* multiple comparisons test.

5.1.7 Differential gene transcription in non-uniform versus uniform ECT was less pronounced after 13 days

Transcriptional differences between non-uniform and uniform ECT after 13 days were much less pronounced compared to after 5 days (Figure 14). Significantly higher transcript levels in uniform compared to non-uniform ECT were only found for Male NF2 for *ACTA2*, *POSTN*, *LUM*, and *CTGF*, as well as for Male DCM1 for *ACTA2*, *POSTN*, and *CTGF*. In the Female

NF and the Male ICM1 ECT, the differences observed at day 5 were abolished and the intergroup differences were inconsistent after 13 days (Figure 15).

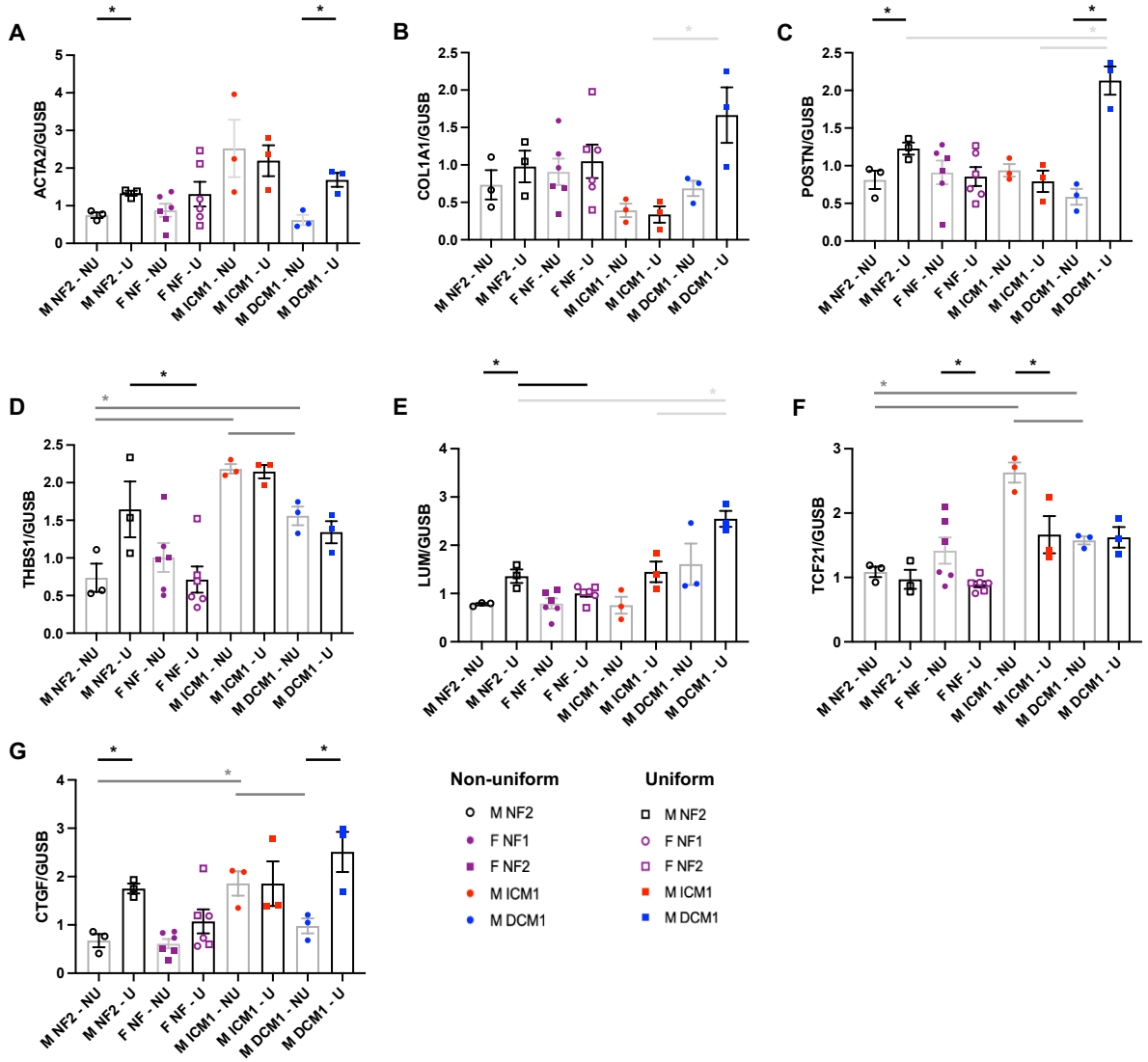

Figure 15. Prolonged culture of ECT shows less pronounced differences in gene expression. 2D-cultured hCF from M NF2, F NF1, F NF2, M ICM1, and M DCM1 were used to generate non-uniform (NU) or uniform (U) ECT. RNA was isolated after 13 days of culture and qPCR analysis of **A)** *ACTA2*, **B)** *COL1A1*, **C)** *POSTN*, **D)** *THBS1*, **E)** *LUM*, **F)** *TCF21*, and **G)** *CTGF* was performed for 3 individual experiments for each donor. All qPCR values were normalized to the mean of the housekeeping gene *GUSB*, means±SEM, *p<0.05 assessed by unpaired t-test (black) or by group-wise (NU - dark gray) or (U - light gray) 1-way-ANOVA with Tukey's *post hoc* multiple comparisons test.

5.2 Dynamic gene transcription changes in ECT during prolonged culture

Having shown that the clear transcriptional differences in the non-uniform versus uniform ECT models after 5 days of culture diminished in the following 8 days, a detailed gene expression time course analysis was performed. Therefore, ECT generated with Male ICM1 hCF were cultured for up to 10 days and qPCR analysis was performed starting from day 2. Genes that

were found to be clearly differentially regulated in non-uniform and uniform Male NF and ICM ECT after 5 days (refer to Figure 14) were analyzed individually, these genes include *LUM*, *THBS1*, *COL1A1*, *ACTA2*, and *POSTN*. Additionally, coiled-coil domain containing 80 (*CCDC80* gene) was investigated. For obtaining a more robust result, their mean change was calculated. The mean expression of this gene cluster was significantly different in non-uniform versus uniform ECT between days 4 and 7 (Figure 16A). More importantly, in the uniform model, gene transcription increased constantly between days 2 and 5, and then plateaued until day 9. In contrast, in the non-uniform model, gene expression was similar within the first 6 days and increased thereafter. Consequently, the difference between the non-uniform and uniform model became insignificant beginning on day 8.

To gain further insight into the gene expression dynamics, especially of how the pro-contractile *ACTA2* gene correlates to the ECT contraction in the non-uniform model, the qPCR result was compared to the pole deflection data. This clearly demonstrated that the increase in *ACTA2* expression parallels ECT contraction until day 4, and then precedes the second contraction phase (Figure 16B).

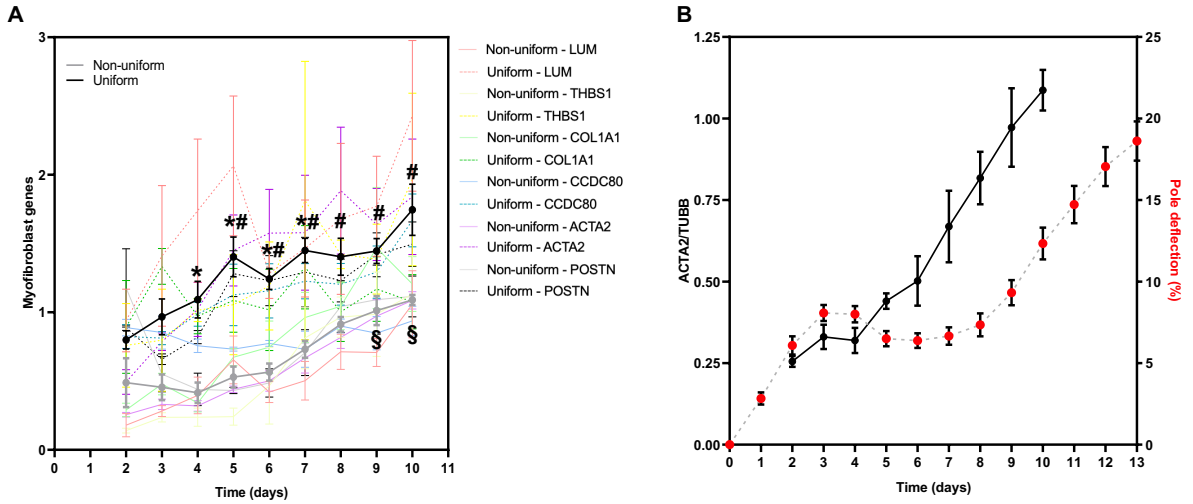

Figure 16. Transcriptional changes and functional correlations between non-uniform and uniform ECT over the course of 10 days. 2D-cultured hCF from M ICM1 were used for generation of ECT and casted in non-uniform or uniform molds for the indicated number of days. **A)** RNA was isolated and qPCR analysis of myofibroblast genes, such as *LUM*, *THBS1*, *COL1A1*, *CCDC80*, *ACTA2*, and *POSTN*, was performed for 3 individual experiments at each time point. A time course of each gene is shown for both non-uniform and uniform ECT, with the mean of all genes for non-uniform in gray and uniform in black. All qPCR values were normalized to the housekeeping gene *TUBB*, means±SEM, *$p<0.05$ comparison of the means of uniform and non-uniform ECT on the same day, $^{\#}p<0.05$ compared to day 2 in the uniform model, and $^{\S}p<0.05$ compared to day 2 in the non-uniform model as analyzed by 2-way-ANOVA with Sidak's *post hoc* multiple comparisons test. **B)** *ACTA2* transcription levels normalized to *TUBB* in the non-uniform ECT between days 2-10 were plotted alongside the passive contraction of non-uniform ECT over the course of 13 days, pole deflection: n=54-61 from at least 3 independent experiments.

5.3 Regulation of ER adaptation in the ECT system

5.3.1 Comparison of transcriptional changes in the M NF1 ECT model with human heart disease

As described in the Preliminary results (2), RNA sequencing of both Male NF1 ECT models at two different time points was performed. Main transcriptional differences between non-uniform and uniform ECT included differences in ECM-related genes and genes involved in protein folding. To further investigate the relevance of these differences with respect to the normal and diseased human heart, a comparison with published transcriptome analyses was performed. However, as our data is representing the transcriptome of only one cell type, to appropriately compare it to published data sets representing the transcriptome of a multi-cellular organ, initial adaptation in data composition and thresholds was applied (Figure 17A) and is described in detail in the Methods (refer to 4.5.2).

After data adaptation, 1,618 genes, including both higher and lower expressed transcripts, were found to be differentially expressed in the two models. Stringent unbiased gene ontology (GO) term analysis was performed with PANTHER, and similar GO terms were identified as being major features between the ECT models as shown in the Preliminary results. These GO terms were involved in ECM organization (green bars), protein folding (blue bars), and of different relation (black bars) (Figure 17B). As one main aim of this thesis was to investigate the role of ER adaptation, a closer identification of the genes involved in the protein folding GO terms: *response to endoplasmic reticulum stress* (GO:0034976)*, protein folding* (GO:0006457), *response to topologically incorrect protein* (GO:0035966), and *response to unfolded protein* (GO:0006986) are represented in a heat map. Of the 101 differentially expressed genes (DEG) found in these GO terms, 92 were upregulated in uniform ECT after day 5, including ER folding genes, such as *HSPA5*, *HSP90B1*, and *DNAJB9*, as well as cytosolic protein folding genes, such as *HSPA1A*. Interestingly, two main signal transducers involved in the UPR, *EIF2AK3* and *DDIT3*, were also significantly upregulated in uniform ECT after day 5 (Figure 17C).

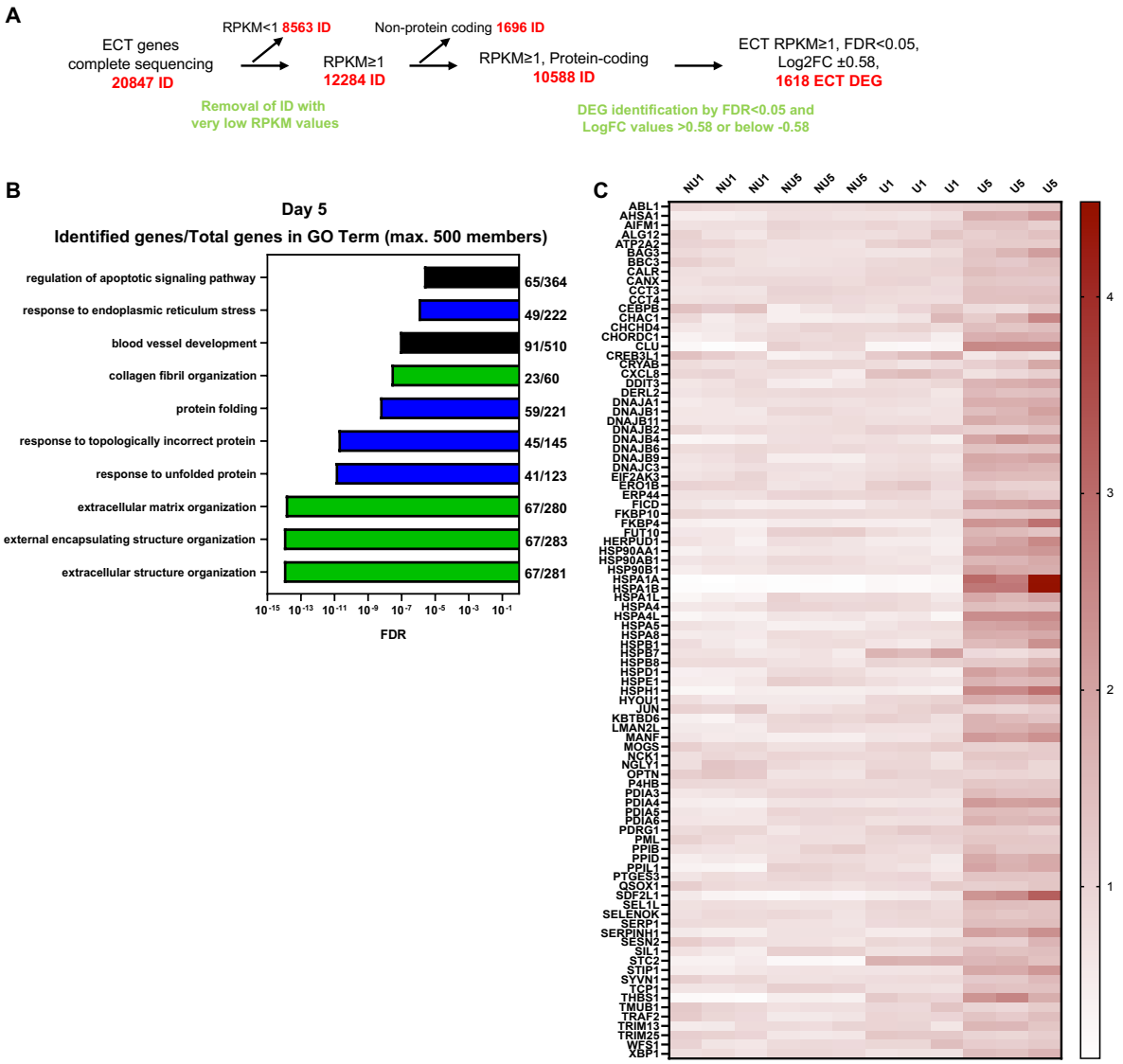

Figure 17. Data adaptation and GO term analysis of RNA sequencing for M NF1 ECT after 5 days. 2D-cultured hCF from M NF1 were used to generate non-uniform (NU) and uniform (U) ECT, then cultured for 1 (NU1, U1) or 5 (NU5, U5) days. RNA was isolated and sequencing was performed for 3 independent experiments. **A**) Single steps of the initial data adaption procedure from original 20,847 identity domains (ID). **B**) Gene ontology (GO) term analysis performed by PANTHER for differentially expressed genes (DEG) between NU and U ECT after day 5 (Reads Per Kilobase Million (RPKM) value under 1, a false discovery rate (FDR) below 0.05, and a log 2-fold change (Log2FC) of ±0.58). The number of identified genes/total number of GO term members are given. **C**) A heat map representing the relative gene expression of protein folding genes from the GO terms: response to endoplasmic reticulum stress, protein folding, response to topologically incorrect protein, and response to unfolded protein.

Next, it was investigated whether differences in the protein folding machinery transcripts were also evident in human hypertrophic (Hyper) (Ren et al., 2020) and heart failure (HF) (Flores et al., 2021) transcriptomic studies. For specific details regarding the data adaptation for these comparisons, refer to the Methods (4.5.3). From both analyses, approximately two thirds of the protein coding genes found in the heart were also found in the ECT data (Figure 18A).

When comparing the ECT data set to the above stated publications, 209 overlapping transcripts were identified exclusively for the hypertrophy data set (ECT ∩ Hypertrophy), and 372 for the heart failure data set (ECT ∩ HF). Furthermore, a substantial overlap of 428 transcripts was found between both hypertrophy and heart failure data sets, which were absent in ECT. Between the ECT, hypertrophy, and heart failure data sets, 150 differentially expressed transcripts were identified (ECT ∩ Hypertrophy ∩ HF). The already mentioned specifications for data adaptation were applied and GO term analysis was once again performed with PANTHER. Mainly an enrichment of ECM organization GO terms (green bars) were revealed between all comparisons; however, no protein folding GO terms were found (Figure 18B).

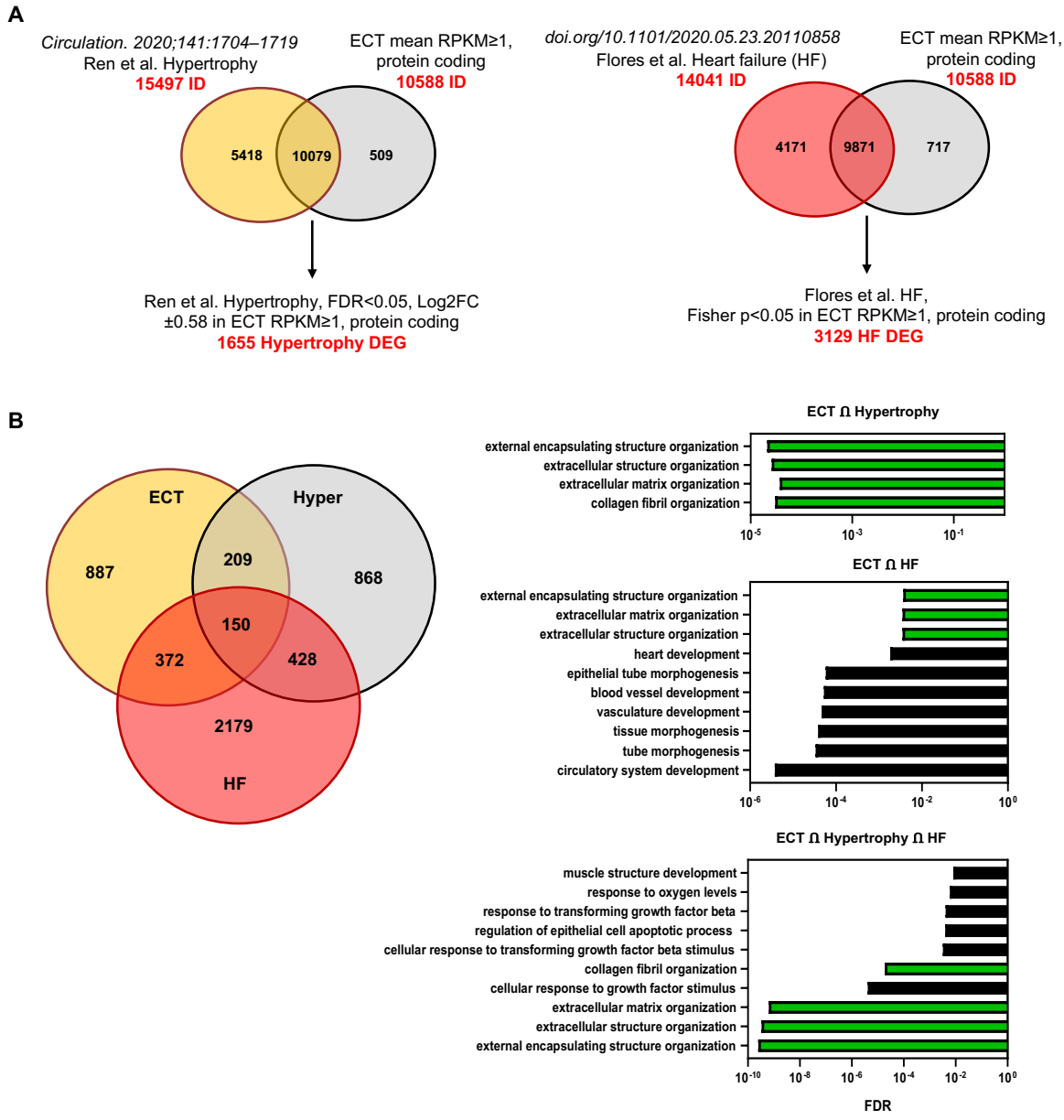

Figure 18. Expression of genes involved in protein folding is dissimilar between ECT and bulk RNA of the diseased heart. 2D-cultured hCF from M NF1 were used to generate non-uniform and uniform ECT then

cultured for 5 days. RNA was isolated and sequencing was performed for 3 independent experiments. **A)** Data adaptation and comparison of 10,588 identity domains (ID) for ECT data set with RNA sequencing from published hypertrophy (Hyper) and heart failure (HF) data sets to identify differentially expressed genes (DEG) is shown (RPKM≥1, protein-coding, FDR<0.05, Log2FC±0.58). **B)** A Venn diagram depicting the overlap of DEG between ECT, hypertrophy, and heart failure data sets. Enriched gene ontology (GO) term identification between ECT and hypertrophy data sets (ECT ∩ Hypertrophy), ECT and heart failure data sets (ECT ∩ HF), as well as all ECT, hypertrophy, and heart failure data sets (ECT ∩ Hypertrophy ∩ HF) were performed using PANTHER.

5.3.2 Comparison of the differential gene expression in ECT with single-cell sequencing data of different fibroblast subtype populations after MI in mice

As the transcriptomes of hypertrophic and heart failure studies present only snapshots of very late time points of these diseases, it was next of interest to compare the ECT model with a more dynamic heart disease model representing earlier transcriptomic changes in fibroblast subtype populations. Therefore, the ECT data was compared to published data of single-cell sequencing from a MI mouse model (Farbehi et al., 2019). As described in more detail in the Introduction (1.5), this publication captured transcriptional profiles of 13,331 cells from male mouse ventricles at days 3 and 7 post-sham or MI surgery, where they described a dynamic flux of different fibroblast subpopulations over time. The statistics of the ECT data was once again adapted to be appropriately compared to the analysis of the single-cell sequencing data (Figure 19A) which is described in detail in the Methods (4.5.4). The overlap between individual fibroblast subpopulations described in the publication (Fibroblast-activated; F-Act, Fibroblast-cycling; F-Cyc, and Myofibroblast 1 & 2; F-Myo) and the ECT data set were compared. Only 35 common DEG were found between the F-Act subpopulation and the ECT data (ECT ∩ F-Act), and 122 DEG were found between the F-Myo subpopulations and the ECT data (ECT ∩ F-Myo). However, these genes were mostly pertaining to GO terms enriched in ECM organization. Interestingly, 191 common DEG were found between the F-Cyc subpopulation and the ECT data (ECT ∩ F-Cyc), with GO terms enriched in ECM organization, as well as protein folding. Furthermore, 39 protein folding genes were upregulated in the overlap with the F-Cyc subpopulation, and only 3 genes were downregulated (Figure 19B), suggesting that the protein folding machinery is transiently activated in a narrow time window in CF after cardiac injury.

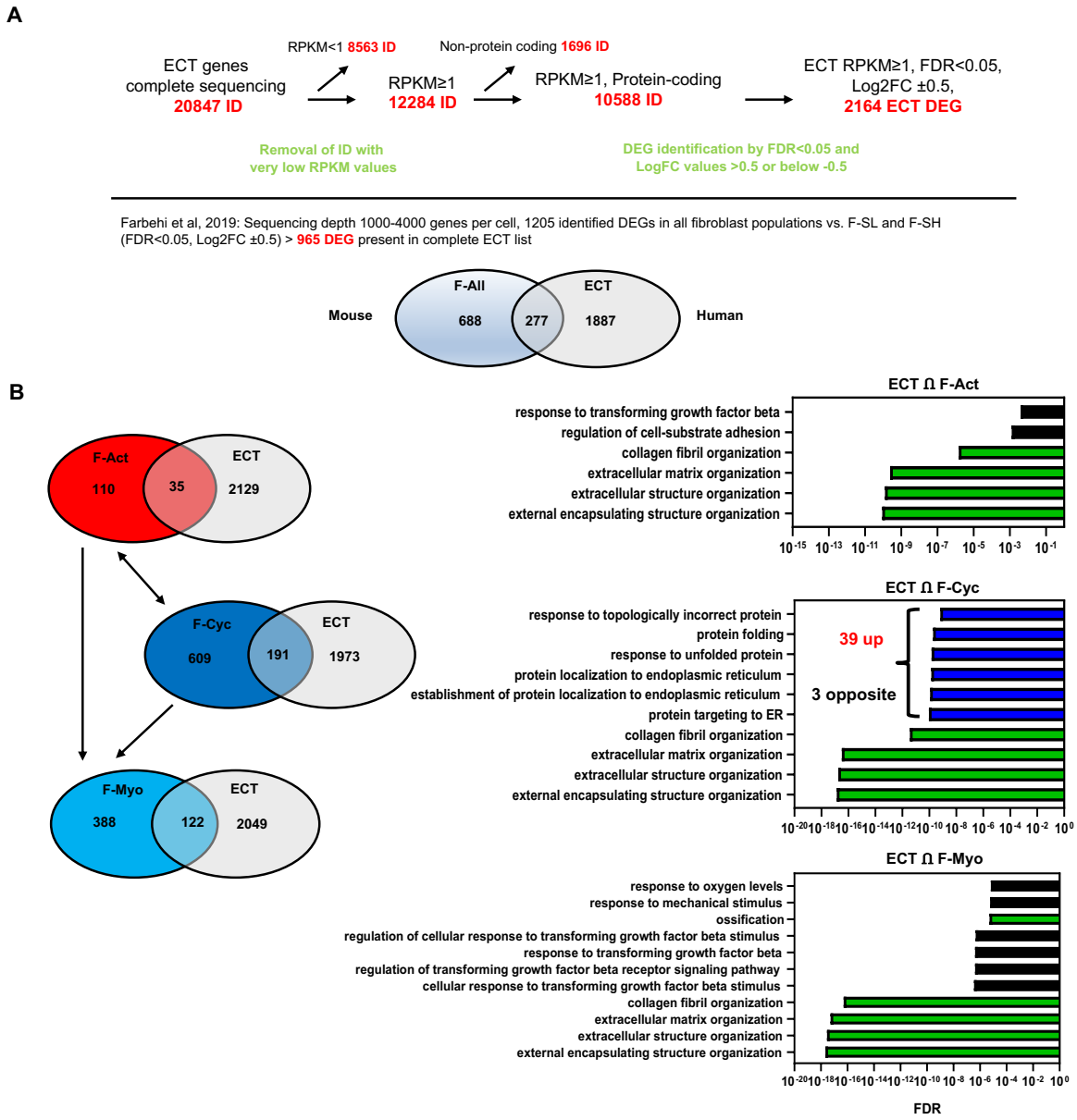

Figure 19. Changes in genes involved in protein folding transiently occur in the phenotypic transdifferentiation of hCF. 2D-cultured hCF from M NF1 were used to generate non-uniform and uniform ECT then cultured for 5 days. RNA was isolated and sequencing was performed for 3 independent experiments. **A)** Data adaptation and comparison of 2,164 identity domains (ID) for ECT data set with published single-cell sequencing data from MI mouse model. **B)** A Venn diagram depicting the overlap of differentially expressed genes (DEG) between different fibroblast subtype populations (Fibroblast-activated; F-Act, Fibroblast-cycling; F-Cyc, and Myofibroblast 1 & 2; F-Myo) found in MI mouse model and the ECT data (RPKM≥1, protein-coding, FDR<0.05, Log2FC±0.5). Enriched gene ontology (GO) term identification between ECT and F-Act data sets (ECT ∩ F-Act), ECT and F-Cyc data sets (ECT ∩ F-Cyc), as well as ECT and F-Myo data sets (ECT ∩ F-Myo) were performed using PANTHER.

5.4 Interference with the PERK pathway of the UPR in ECT and 2D-cultured hCF

5.4.1 PERK expression is differentially regulated in non-uniform and uniform ECT

As previously mentioned, RNA sequencing from uniform Male NF1 ECT after 5 days revealed an upregulation of genes involved in protein folding in the ER and the cytosol, and in the UPR. Specifically, an upregulation of the *EIF2AK3* gene, which encodes the UPR kinase PERK, was identified (Figure 20A). This result was verified by qPCR and immunoblot analysis (Figure 20B, C). Next, *EIF2AK3*/PERK expression was analyzed in Male ICM1 hCF to test whether this is a common regulation. Similarly, protein levels were significantly higher and *EIF2AK3* transcript levels were higher by trend for uniform compared to non-uniform ECT after 5 days (Figure 20D, E). For further control, the biomechanical properties of ECT generated with both hCF donors were directly compared (refer to Figure 8), demonstrating similar differences in ECT stiffnesses (Figure 20F).

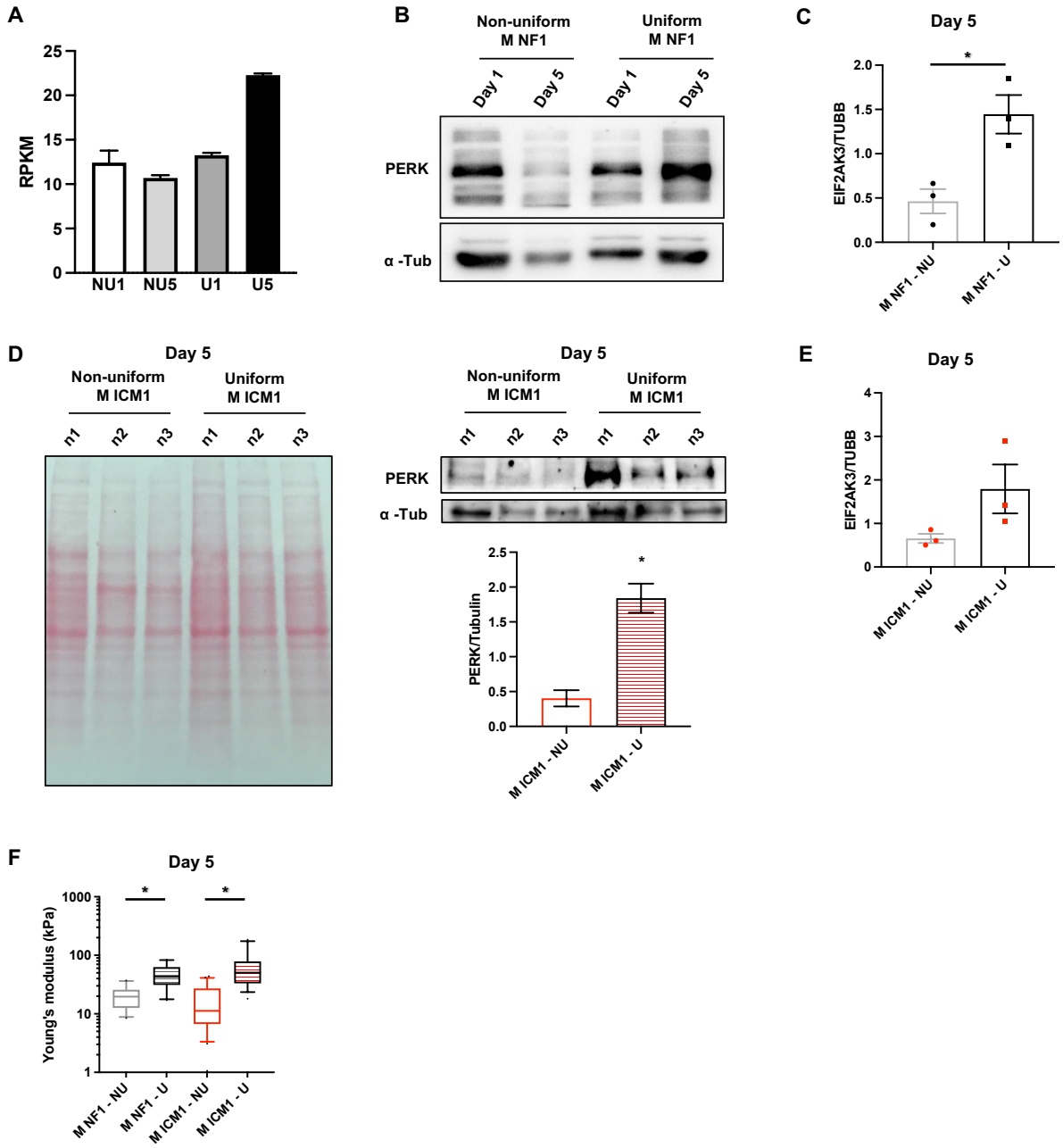

Figure 20. Verification of PERK expression in ECT from M ICM1. hCF from M NF1 or M ICM1 were used to generate ECT in non-uniform (NU) or uniform (U) molds and cultured for 1 or 5 days. All data in this figure referring to M NF1 is from the Ph.D. thesis of Gabriela L. Santos. **A)** RNA was isolated from M NF1 and sequencing was performed for 3 independent experiments. Heat map of relative gene expression of eukaryotic translation initiation factor 2 alpha kinase 3 (*EIF2AK3*) for NU day 1 (NU1), NU day 5 (NU5), U day 1 (U1), and U day 5 (U5) ECT (RPKM≥1). **B)** Representative immunoblots of the expression of protein kinase R-like endoplasmic reticulum kinase (PERK) and the housekeeping protein α-tubulin (α-Tub) are shown for non-uniform and uniform ECT generated from M NF1 and cultured for 1 or 5 days. **C)** RNA was isolated from M NF1 and qPCR analysis of *EIF2AK3* was performed for 3 individual experiments. All qPCR values were normalized to the mean of the housekeeping gene *TUBB*, means±SEM, $^{*}p<0.05$. Statistical analysis by unpaired t-test. **D)** Ponceau S image depicting the loaded protein, for reference. Representative immunoblots and the corresponding analyses of the expression of PERK and α-Tub are shown for non-uniform and uniform ECT generated from M ICM1 and cultured for 5 days. Protein levels were normalized by α-Tub, n=3, means±SEM, $^{*}p<0.05$ vs. M ICM1 - NU by unpaired t-test. **E)** RNA was isolated from M ICM NU and U ECT, and qPCR analysis of *EIF2AK3* was performed for 3 individual experiments. All qPCR values were normalized to the mean of the housekeeping gene *TUBB*,

means±SEM. **F)** Analysis of the Young's Moduli for non-uniform and uniform ECT generated with M NF1 or M ICM1 hCF. The values are presented as box plots with 5-95 percentile whiskers, n=21-23 (M NF1) or n=33-44 (M ICM1) from at least 3 independent experiments, $^{*}p<0.05$ NU vs. U assessed by unpaired t-test.

To further validate this finding, a PCR time course analysis of different genes involved in protein folding was performed. Therefore, non-uniform and uniform ECT were generated with Male ICM1 hCF and harvested every day between days 2 and 10 of culture.

Regarding protein folding in the cytosol, the genes *HSPA1A*, a stress inducible Hsp70 chaperone, and *HSP90AA1*, a cytosolic stress inducible chaperone of the Hsp90 family, showed an almost constant expression level in uniform ECT over the course of 10 days. In contrast, both genes showed low expression at day 2 in non-uniform ECT, then increased over the following days and reached a peak at day 5. After peaking at day 5, the expression in the non-uniform ECT was approximately at the same level as in the uniform model (Figure 21A, B).

Next, genes involved in ER protein folding were examined. The gene that encodes for the ER Hsp70 master regulator chaperone BiP (*HSPA5* gene), the ER chaperone *HSP90B1*, and the co-chaperone *DNAJB9* all showed opposite trends in the non-uniform and uniform model, with their expression starting high in uniform and low in non-uniform ECT. After 4 to 5 days, the expression of these genes converged to an intermediate level (Figure 21C-E).

DDIT3, a transcription factor involved in the UPR that regulates apoptosis caused by prolonged ER stress, did not show any significant differences in expression between the non-uniform and uniform ECT over the complete time course. *EIF2AK3* was by trend expressed more highly during the first 5 days in the uniform model; however, due to the variance, this effect could not be statistically verified in this time course analysis (Figure 21F, G).

Taken together, in these experiments with Male ICM1 hCF, the differences between both models were less clear and appeared to manifest earlier than shown before for the Male NF1 hCF. Moreover, the more pronounced adaptation occurred for the Male ICM1 hCF in the non-uniform model. Importantly, gene expression after day 5 was similar in both models and did not follow the increased expression of the secreted myofibroblast genes, e.g., *COL1A1*, *LUM*, and *POSTN* (Figure 16A). This indicates that the observed changes and differences in transcription of protein folding genes reflect ER adaptation processes occurring within the first 5 days after ECT generation.

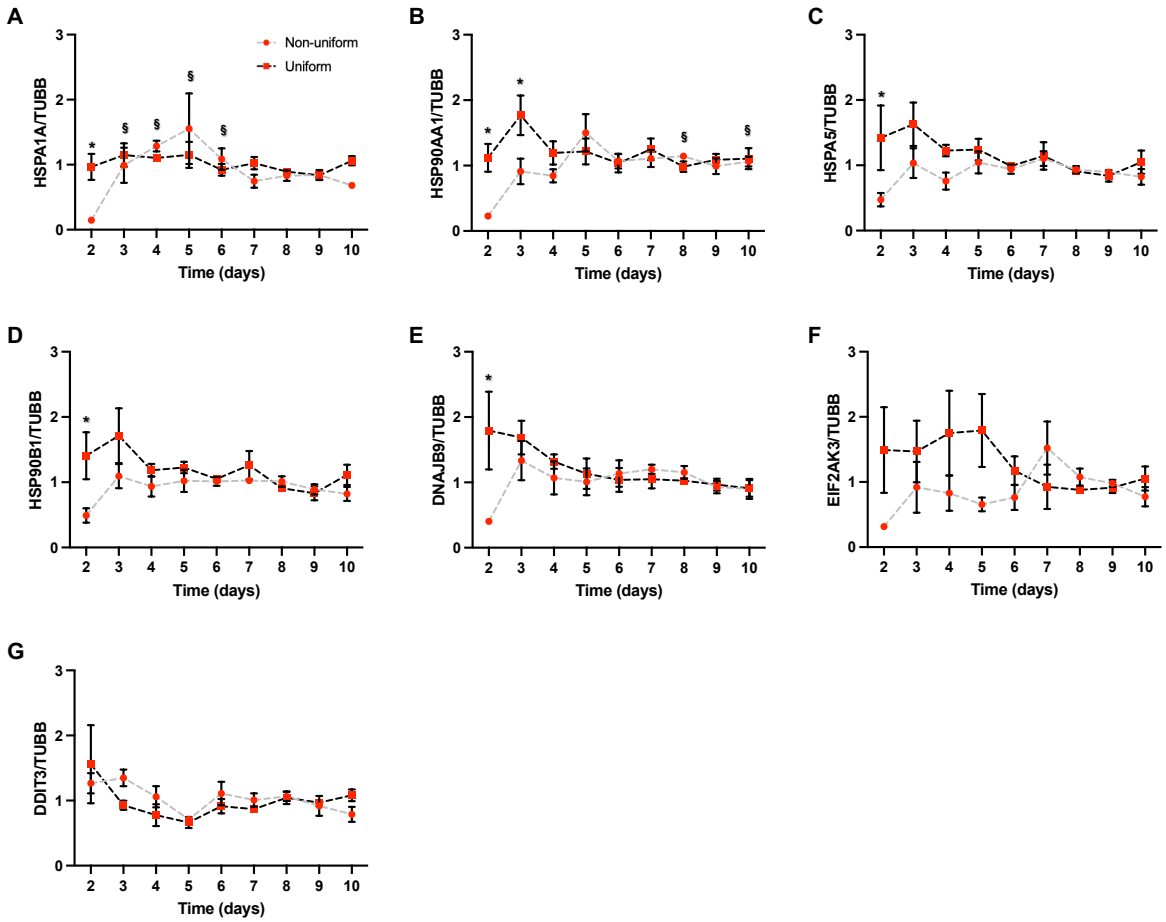

Figure 21. Time course of gene expression for selected genes involved in cytosolic/ER protein folding and the UPR in ECT. 2D-cultured hCF from M ICM1 were used for generation of ECT and casted in non-uniform or uniform molds then cultured for 10 days. ECT were snap-frozen for each day between 2 and 10 days. RNA was isolated and qPCR analysis was performed for 3 individual experiments. Genes involved in **A, B)** cytosolic protein folding (*HSPA1A* and *HSP90AA1*), **C-E)** endoplasmic reticulum protein folding (*HSPA5*, *HSP90B1*, and *DNAJB9*), and **F, G)** the unfolded protein response (*EIF2AK3* and *DDIT3*) are shown. All qPCR values were normalized to the mean of the housekeeping gene *TUBB*, means±SEM, $^{*}p<0.05$ non-uniform vs. uniform analyzed by 2-way-ANOVA with Sidak's *post hoc* multiple comparisons test, $^{§}p<0.05$ vs non-uniform Day 2 analyzed by 2-way-ANOVA with Tukey's *post hoc* multiple comparisons test.

5.4.2 PERK inhibition affects the biomechanical properties of ECT and induces UPR activation

As PERK is the master regulator of one branch of the UPR and plays a role in ER adaptation and stress (Harding et al., 1999), the consequence of its inhibition in the ECT models was studied next. Therefore, Male ICM1 hCF were used to generate non-uniform and uniform ECT, which were treated with 0.03, 0.3, and 3 µM GSK'157 1 h after generation and cultured for 5 days. Pole deflection analysis in the non-uniform model showed that the highest concentration of GSK'157 inhibited contraction beginning on day 3 and continued until day 5 (Figure 22A). To assess ECT compaction, macroscopic images were taken, and the CSA were estimated. The

PERK inhibitor induced a concentration-dependent increase in the CSA for the non-uniform ECT, with the highest concentration significantly increasing the CSA compared to control ECT (Figure 22B). No such effect was observed in the uniform model (Figure 22C). Uniaxial tensile testing showed that GSK'157 treatment resulted in reduced ECT stiffness with the middle and highest concentrations for non-uniform ECT (Figure 22D), and the lowest and highest concentrations for uniform ECT (Figure 22E). The ultimate strain reflecting ECT extensibility remained mostly consistent for both models (Figure 22F, G). After 5 days in culture, the ECT were dissociated to isolate the cells, and the number of viable cells was counted with the CASY TTC system. For both models, no effect of GSK'157 on cell viability could be identified (Figure 22H, I).

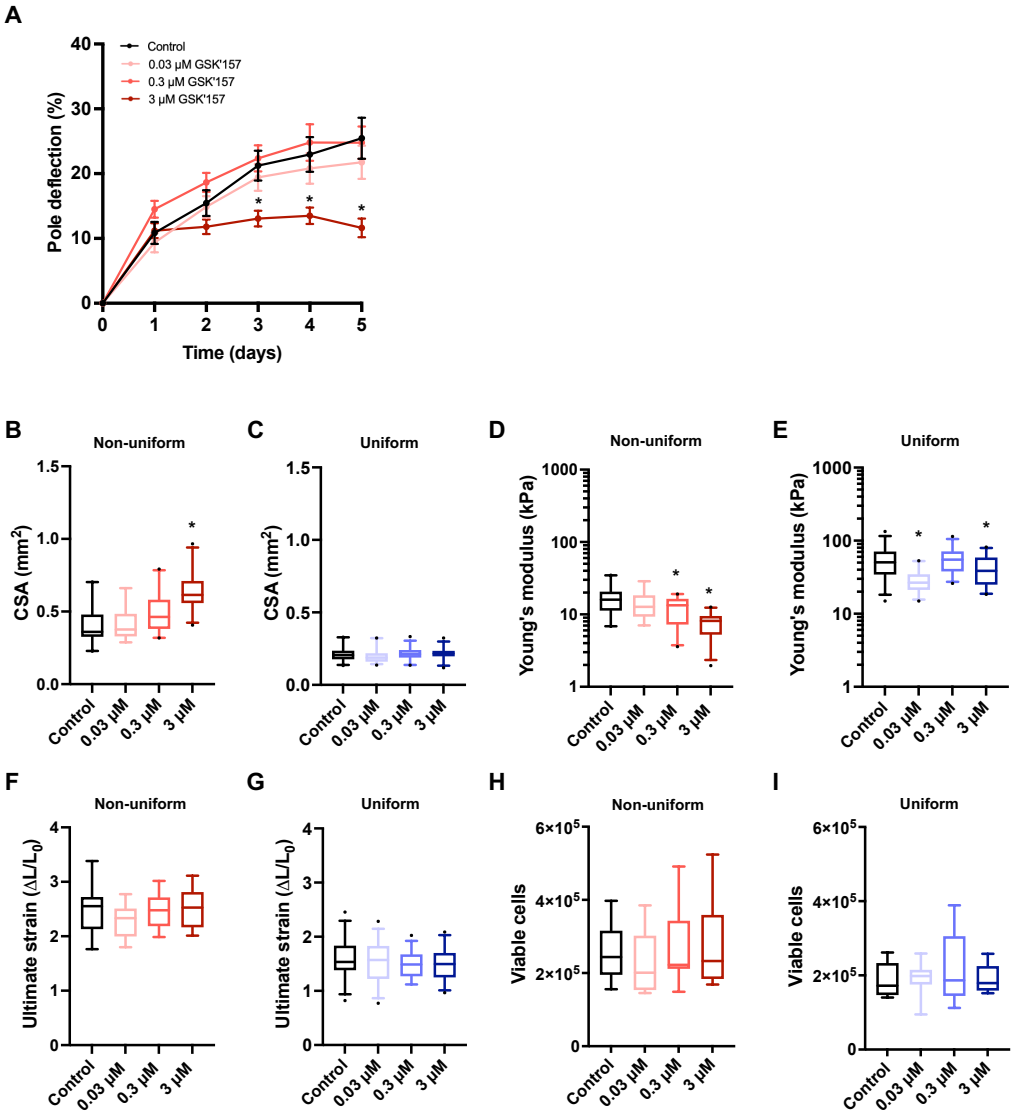

Figure 22. PERK inhibition affects the stiffness of both non-uniform and uniform M ICM1 ECT. hCF from M ICM1 were used to generate ECT in non-uniform or uniform molds then treated with the indicated concentrations of GSK'157 for 5 days. **A)** Pole deflection of non-uniform ECT was measured for each condition

over the course of 5 days, n=38-48 from 3 independent experiments, means±SEM, *p<0.05 vs. Control by 2-way-ANOVA with Tukey's *post hoc* multiple comparisons test. Morphometric measurements and rheology were performed. Analysis of CSA for **B)** non-uniform and **C)** uniform ECT. The values are presented as box plots with 5-95 percentile whiskers, n=13-22 (non-uniform) or n=29-32 (uniform) from at least 3 independent experiments, *p<0.05 vs. Control by 1-way-ANOVA. Analysis of the Young's Moduli for **D)** non-uniform and **E)** uniform ECT. The values are presented as box plots with 5-95 percentile whiskers, n=17-22 (non-uniform) or n=24-32 (uniform) from at least 3 independent experiments, *p<0.05 vs. Control by 1-way-ANOVA Dunnett's *post hoc* multiple comparisons test. Analysis of the ultimate strain for **F)** non-uniform and **G)** uniform ECT. The values are presented as box plots with 5-95 percentile whiskers, n=17-22 (non-uniform) or n=24-32 (uniform) from at least 3 independent experiments. Number of viable cells isolated from **H)** non-uniform and **I)** uniform ECT. The values are presented as box plots with 5-95 percentile whiskers, n=7-8 (non-uniform) and n=9 (uniform) from 3 independent experiments.

For comparison to the results found for PERK inhibition in Male ICM1 ECT, non-uniform Male NF2 ECT were also generated and treated with 0.03, 0.3, 3 µM GSK'157. Pole deflection showed a consistent decrease for the highest concentrations from day 3 on (Figure 23A). No significant change in compaction was found in any condition for the non-uniform ECT (Figure 23B). However, the highest concentration did significantly decrease stiffness in the non-uniform ECT, as similarly seen for non-uniform Male ICM1 ECT (Figure 22D, Figure 23C).

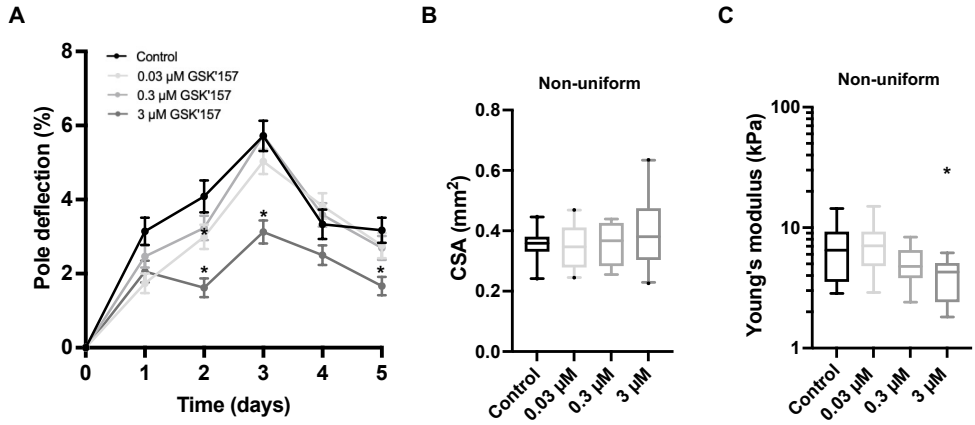

Figure 23. PERK inhibition affects ECT contraction and stiffening of non-uniform M NF2 ECT. hCF from M NF2 were used to generate ECT in non-uniform molds then treated with the indicated concentrations of GSK'157 for 5 days. **A)** Pole deflection of non-uniform ECT was measured for each condition over the course of 5 days, n=27-29 from 2 independent experiments, means±SEM, *p<0.05 vs. Control by 2-way-ANOVA with Tukey's *post hoc* multiple comparisons test. Analysis of CSA for **B)** non-uniform ECT. The values are presented as box plots with 5-95 percentile whiskers, n=19-21 (non-uniform) at least 2 independent experiments, *p<0.05 vs. Control by 1-way-ANOVA. Analysis of the Young's Moduli for **C)** non-uniform ECT. The values are presented as box plots with 5-95 percentile whiskers, n=15-16 (non-uniform) from at least 2 independent experiments, *p<0.05 vs. Control by 1-way-ANOVA Dunnett's *post hoc* multiple comparisons test.

To better understand the effects of GSK'157 on the Male ICM1 ECT, the expression of a set of genes was investigated by qPCR. Typical fibroblast and myofibroblast markers, such as *TCF21* and *ACTA2*, were unchanged for both non-uniform and uniform ECT (Figure 24A-D).

However, *COL1A1* and *CTGF* were decreased in the non-uniform model, and *CTGF* was also decreased in the uniform model after treatment with 3 µM GSK'157 (Figure 24E-H). Interestingly, this was accompanied by an increase in *DDIT3* transcript levels for both non-uniform and uniform ECT (Figure 24I, J), indicating an activation of the UPR in response to PERK inhibition and a potential link to *COL1A1* regulation.

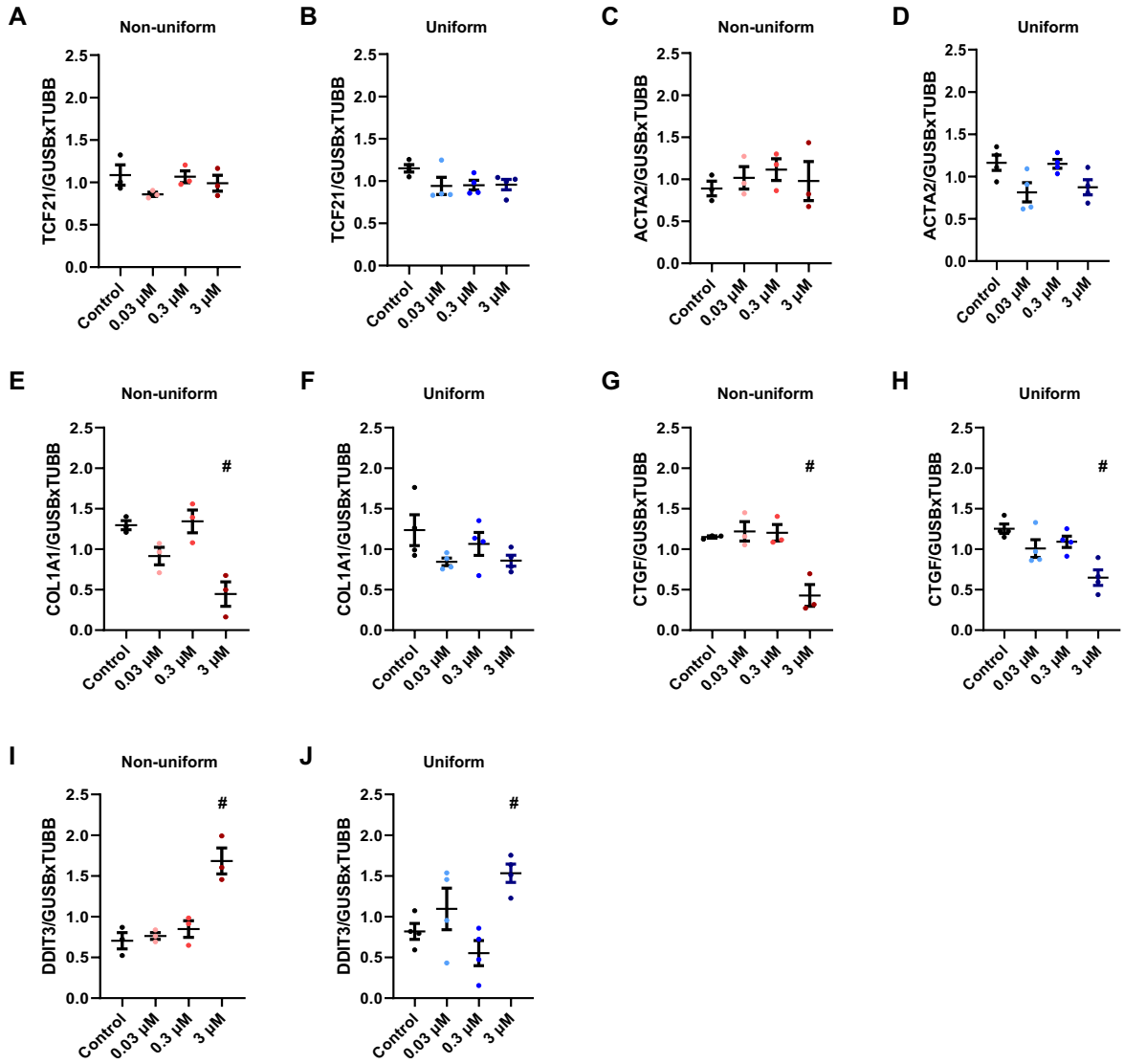

Figure 24. PERK inhibition results in ER stress induction and COL1A1 and CTGF downregulation in M ICM1 ECT. hCF from M ICM1 were used to generate ECT in non-uniform or uniform molds then treated with the indicated concentrations of GSK'157 for 5 days. RNA was isolated and qPCR analysis of **A, B)** fibroblast (*TCF21*), **C, D)** myofibroblast (*ACTA2* and *COL1A1*), **E-H)** extracellular matrix (ECM) organization (*CTGF*), and **I, J)** unfolded protein response (*DDIT3*) related genes was performed for non-uniform and uniform ECT from 3-4 individual experiments. All qPCR values were normalized to the mean of the housekeeping genes *GUSB* and *TUBB*, means±SEM, $^{\#}p<0.05$ vs. Control. Statistical analysis by 1-way-ANOVA with Dunnett's *post hoc* multiple comparisons test.

5.4.3 PERK inhibition affects proliferation and induces *DDIT3* expression in 2D-cultured M ICM1 hCF

To further analyze the effect of GSK'157 on hCF, a proliferation assay was performed with 2D-cultured Male ICM1 hCF. The cells were treated with a concentration range from 0.03 to 3 µM of GSK'157 and cultured for a maximum of 6 days. Only the highest concentration exhibited a significant impairment in proliferation after 6 days (Figure 25A). Additionally, the effect of GSK'157 on the protein levels of the ER stress markers, PERK and BiP, was investigated, demonstrating downregulation of both proteins by 3 µM GSK'157 after 4 days (Figure 25B, C). In line with this result, the corresponding transcripts, *EIF2AK3* and *HSPA5,* were already downregulated one day prior (Figure 25D, E). As shown for the Male ICM1 ECT, PERK inhibition resulted in higher *DDIT3* (Figure 25F) and lower *COL1A1* transcription (Figure 25G). Additionally, the proteoglycan lumican (*LUM*) was lower expressed (Figure 25H). However, not all examined genes were regulated, as shown for the cytosolic chaperone *HSPA1A* (Figure 25I) and the two matricellular factors, *CTGF* (Figure 25J) and *THBS1* (Figure 25K). Taken together, this data corroborates that moderate ER stress induction by PERK inhibition reduces *COL1A1* expression in Male ICM1 hCF.

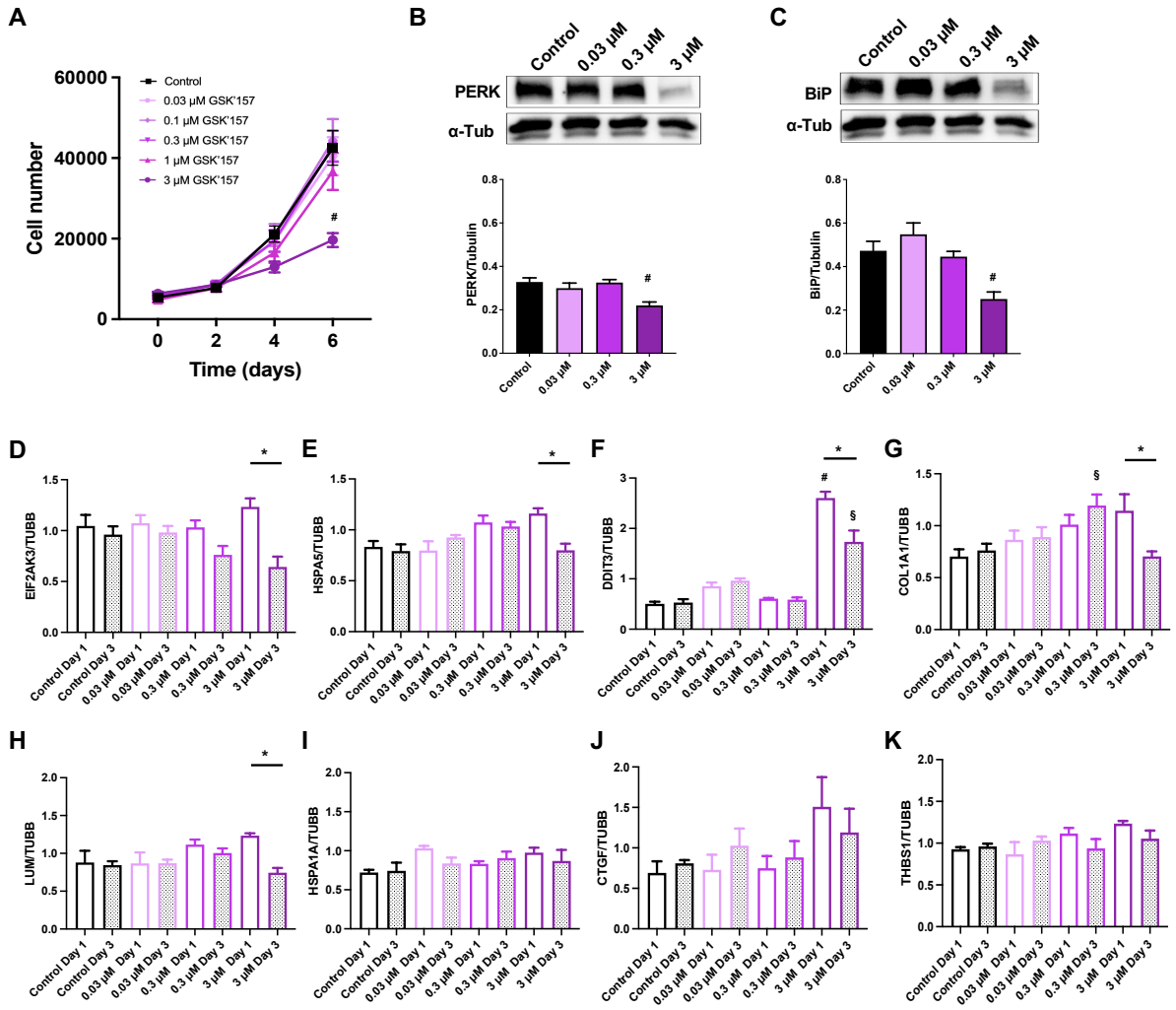

Figure 25. Interference with PERK activity by the inhibitor GSK'157 leads to an inhibition in proliferation, induction of ER stress, and regulation of exemplary ECM regulators in 2D. hCF from M ICM1 were cultured for 1, 3, 4, or 6 days in 2D and treated with the indicated concentrations of GSK'157. **A)** Cell proliferation was assessed by automated counting of DAPI-stained nuclei, n=3 in 4 replicates each, means±SEM, $^{\#}p<0.05$ vs. Control by 2-way-ANOVA with Tukey's *post hoc* multiple comparisons test. **B, C)** Representative immunoblots and the corresponding analyses of the expression of protein kinase R-like endoplasmic reticulum kinase (PERK), binding immunoglobulin protein (BiP), and of the housekeeping protein α-tubulin (α-Tub) are shown. Protein levels were normalized to α-Tub and are given relative to the control, n=7, means+SEM, $^{\#}p<0.05$ vs. Control by 1-way-ANOVA with Dunnett's *post hoc* multiple comparisons test. RNA was isolated and qPCR analysis of **D)** *EIF2AK3,* **E)** *HSPA5*, **F)** *DDIT3*, **G)** *COL1A1*, **H)** *LUM*, **I)** *HSPA1A*, **J)** *CTGF*, and **K)** *THBS1* was performed for 3-4 individual experiments. All qPCR values were normalized to the mean of the housekeeping gene *TUBB*, means+SEM, $^{*}p<0.05$ vs. 3µM Day 1, $^{\#}p<0.05$ vs. Control Day 1, $^{\S}p<0.05$ vs. Control Day 3. Statistical analysis by unpaired t-test or 1-way-ANOVA with Tukey's *post hoc* multiple comparisons test.

5.5 Interference with the ER results in the downregulation of Collagen I

5.5.1 Classical ER stress inducer thapsigargin results in a downregulation of *COL1A1* in hCF

As the results so far have suggested that an interference with the UPR results in a downregulation of *COL1A1*, the effect of acute ER stress induction was investigated next. Therefore, 2D-cultured hCF from Male NF2, Male ICM1, and Male DCM1 donors were treated with the ER stress inducer thapsigargin (TGN), which inhibits Ca^{2+} uptake via the SERCA pump into the ER, for varying time durations (0.5 - 8 h).

On the mRNA level, TGN did reduce *COL1A1* by trend within 4-8 h (Figure 26A). Furthermore, *HSPA5* (BiP) expression was significantly increased within 8 h of TGN treatment (Figure 26B) and *DDIT3* (CHOP) expression was significantly increased within 4 h of TGN treatment (Figure 26C).

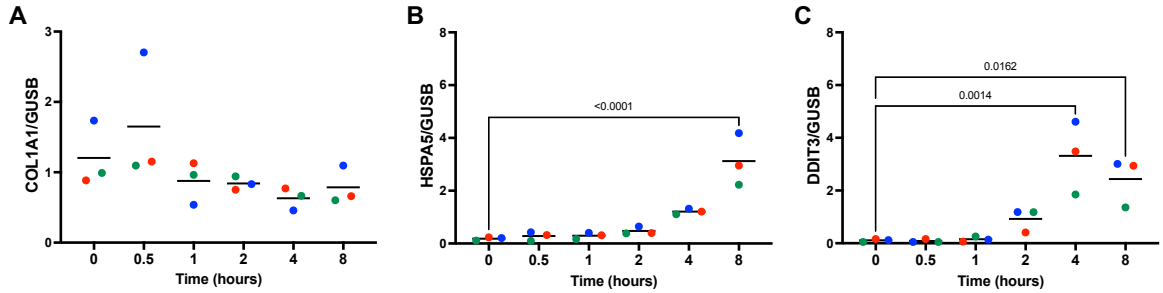

Figure 26. Effect of classical ER stress inducer thapsigargin on gene expression in normal and diseased hCF. hCF from M NF2 (green), M ICM1 (red), or M DCM1 (blue) donors were treated with 0.3 µM thapsigargin (TGN) for the indicated amount of time. RNA was isolated and qPCR analysis of **D)** *COL1A1,* **E)** *HSPA5*, and **F)** *DDIT3* was performed for each individual donor. All qPCR values were normalized to the mean of the housekeeping gene *GUSB*, p-values assessed by 1-way-ANOVA with Tukey's *post hoc* multiple comparisons test.

Protein analyses showed that TGN treatment results in a downregulation of pro-Collagen I expression by trend in all three donors after 8 h (Figure 27A, B). Protein expression of IRE1α did not change throughout the time course (Figure 27A, C), and BiP and CHOP expression was significantly increased after 8 h when compared to the control (Figure 27A, D, E).

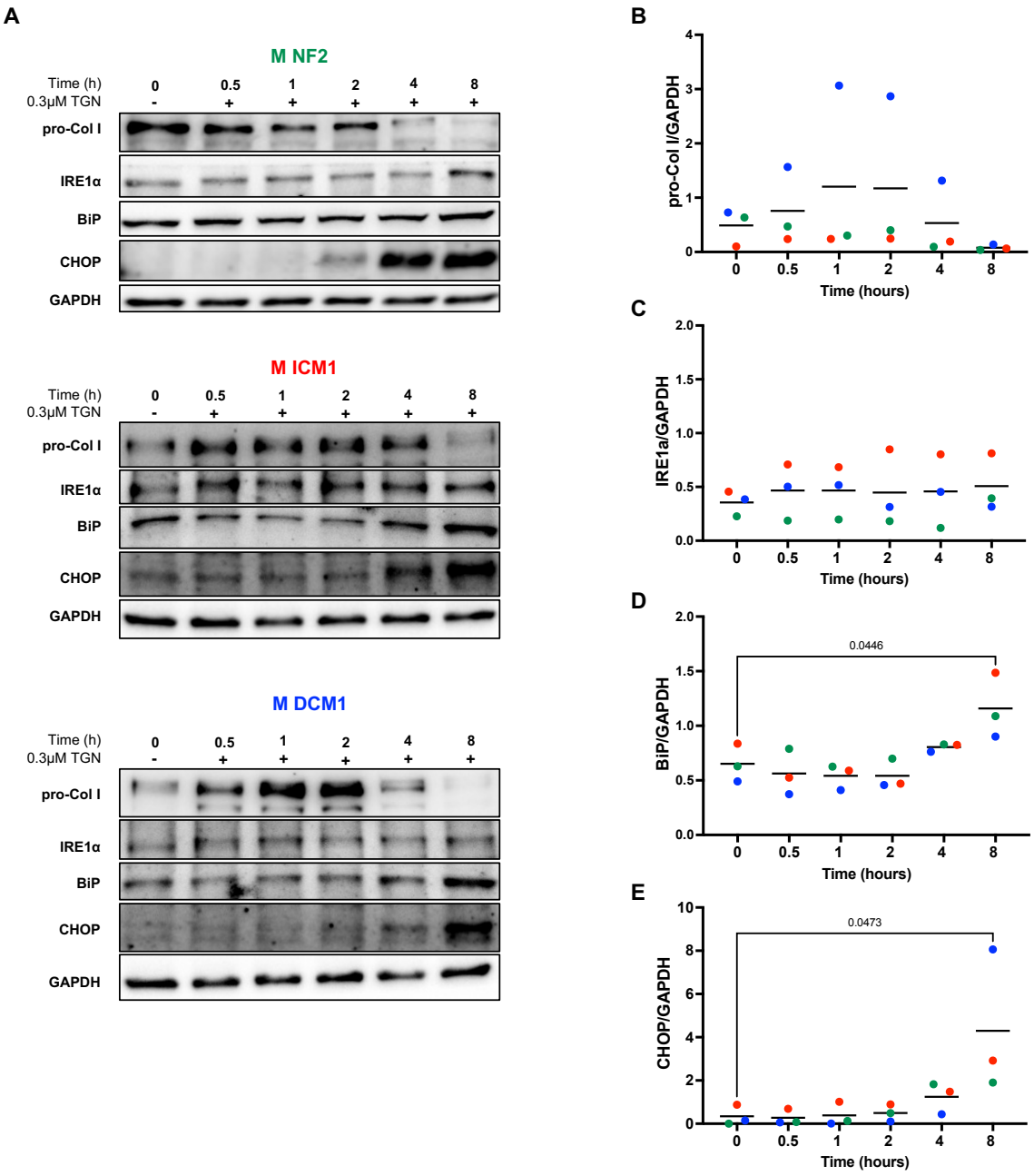

Figure 27. Effect of classical ER stress inducer thapsigargin on protein expression in normal and diseased hCF. hCF from M NF2 (green), M ICM1 (red), or M DCM1 (blue) donors were treated with 0.3 μM thapsigargin (TGN) for the indicated durations. Cell lysates were used for protein analysis. **A)** Representative immunoblots of intracellular pro-Collagen I (pro-Col I), IRE1α, BiP, CHOP, and the housekeeping protein GAPDH for all three hCF donors are shown. The corresponding analyses for the expression of **B)** intracellular pro-Col I, **C)** IRE1α, **D)** BiP, and **E)** CHOP are given. Protein levels were normalized to GAPDH expression, n=3, p-values assessed by 1-way-ANOVA with Tukey's *post hoc* multiple comparisons test.

5.5.2 Collagen expression in human cardiac fibroblasts is closely regulated by the UPR mediator PERK

To further understand the molecular mechanism behind the observed collagen I regulation by interference with the ER via the PERK inhibitor GSK'157 and TGN, the effect of a combined treatment was investigated. 2D-cultured hCF from Male NF2, Male ICM1, and Male DCM1 donors were treated with GSK'157 for 4 days after ER stress induction with TGN for 1 h. Whole cell lysates were prepared, and the medium was collected to perform immunoblotting. For detection, pro-Collagen I, Collagen I, PERK, BiP, and GAPDH antibodies were used. Protein analysis showed that without TGN treatment, GSK'157 reduced the amounts of intracellular pro-Collagen I in a bell-shaped concentration manner, with a transient decline for the lowest concentration, a significant upregulation in expression for the middle concentration, and a significant downregulation with the highest concentration for all donor cells regardless of disease (Figure 28A, B). TGN alone resulted in a complete loss of intracellular pro-Collagen I. When inducing ER stress, the combination with GSK'157 partly restored intracellular pro-Collagen I expression for the middle and highest concentrations. This effect could also be seen for extracellular Collagen I expression, although it was not significant (Figure 28A, C).

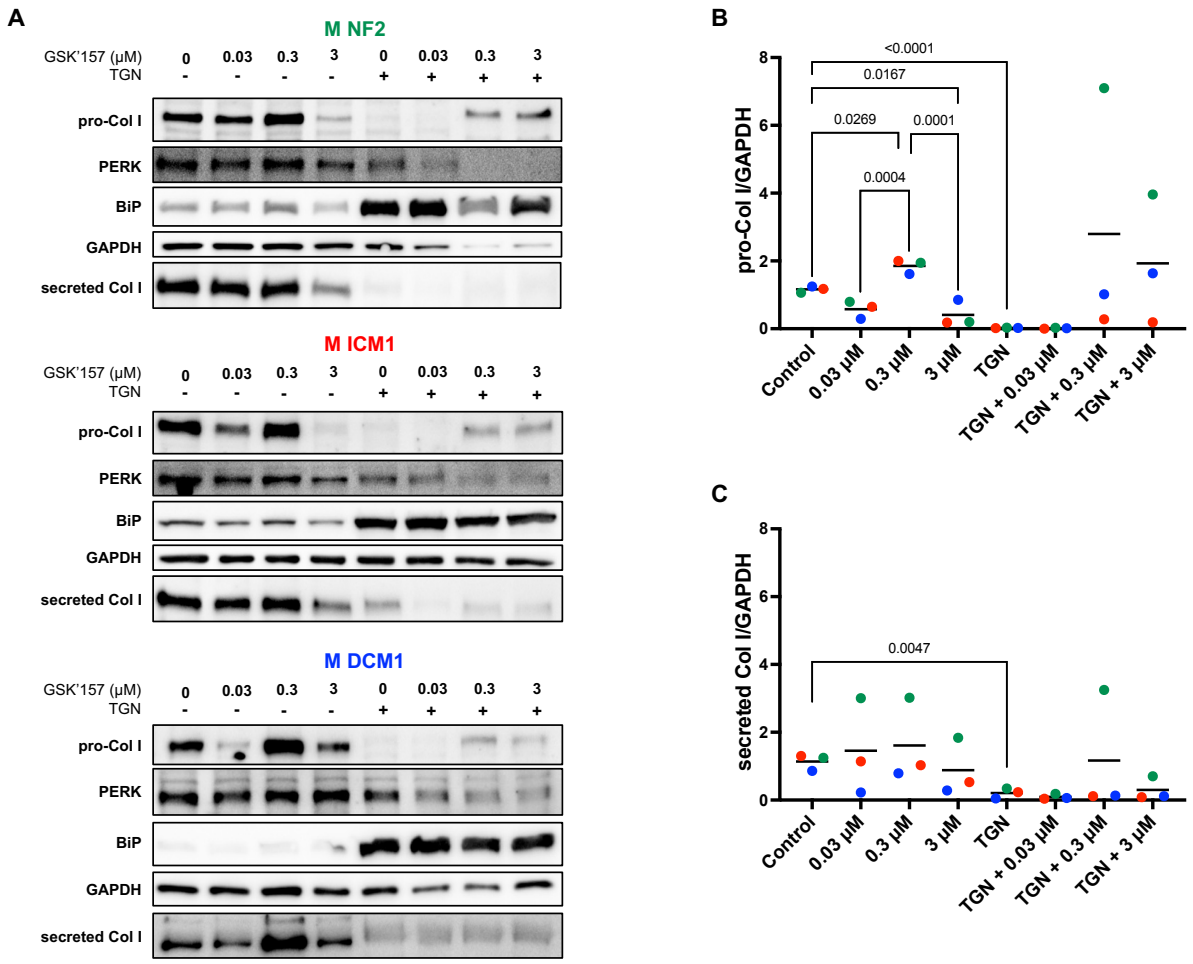

Figure 28. PERK inhibition by GSK'157 partly restores pro-Collagen I levels under high ER stress in normal and diseased hCF. hCF from M NF2 (green), M ICM1 (red), or M DCM1 (blue) donors were pulsed for 1 h with 0.3 µM TGN and treated with the indicated concentrations of GSK'157 for 4 days. Cell lysates and medium were used for protein analysis. **A)** Representative immunoblots of intracellular pro-Collagen I (pro-Col I), PERK, BiP, the housekeeping protein GAPDH, and extracellular Collagen I (secreted Col I) for all three hCF donors are shown. The corresponding analyses for the expression of **B)** intracellular pro-Col I and **C)** secreted Col I are given. Protein levels were normalized to GAPDH expression and are given relative to the basal conditions, n=3, p-values assessed by unpaired t-test or 1-way-ANOVA with Tukey's *post hoc* multiple comparisons test.

As it has been shown that GSK'157 does have a clear off-target effect (Rojas-Rivera et al., 2017), an additional PERK inhibitor, AMG PERK 44 (AMG'44), was investigated. Therefore, 2D-cultured hCF from Male NF2, Male ICM1, and Male DCM1 donors were treated with AMG'44 for 4 days after ER stress induction with TGN for 1 h. Interference with PERK showed a downregulation of intracellular and extracellular Collagen I by 0.5 µM AMG'44 in all donor cells (Figure 29A, B). TGN once again resulted in a complete loss of pro-Collagen I. Under high ER stress, only 5 µM AMG'44 led to a moderate restoration of intracellular pro-Collagen I. This effect was not observed for extracellular Collagen I (Figure 29A, C).

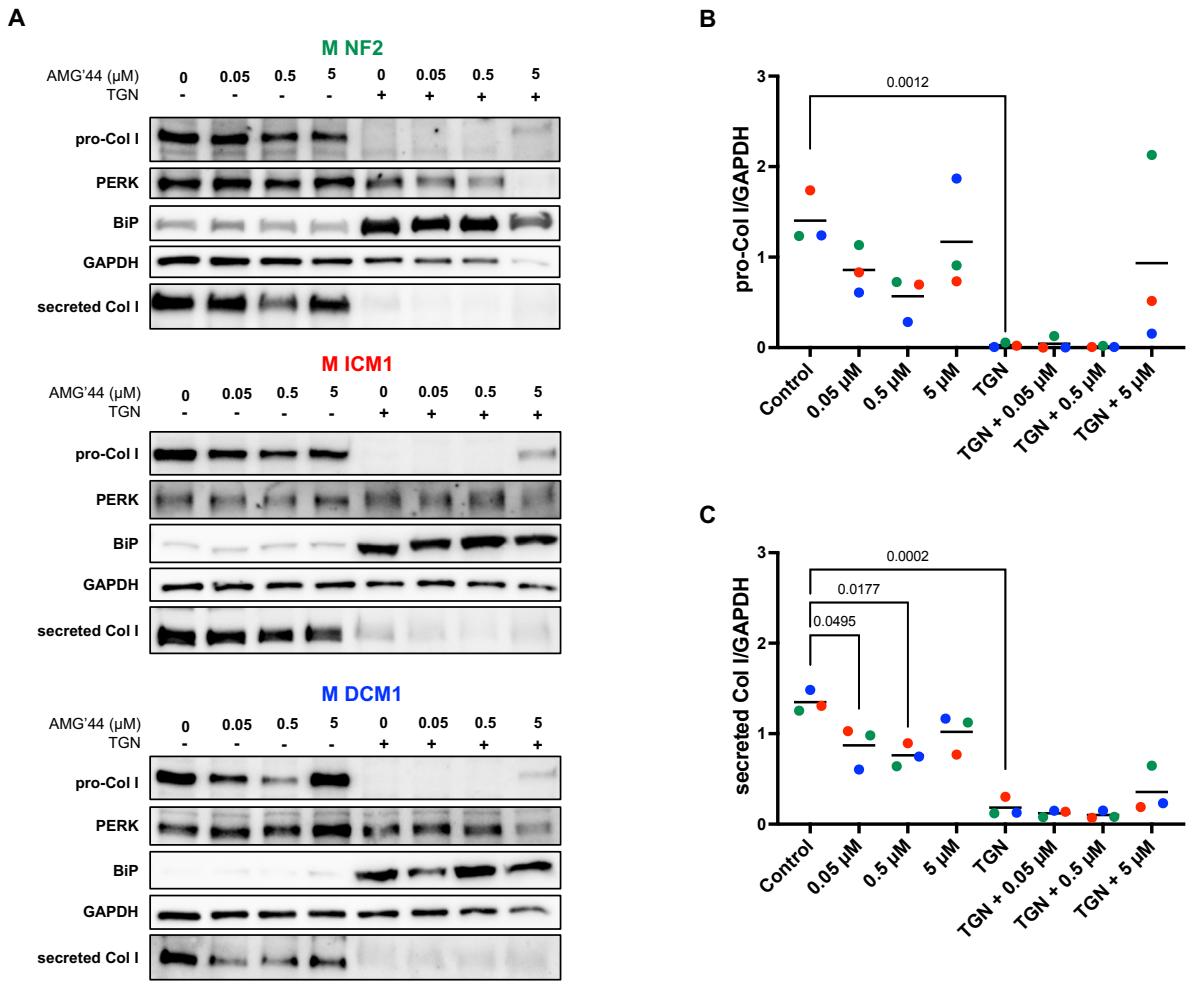

Figure 29. PERK inhibition by AMG PERK 44 partly restores pro-Collagen I levels under high ER stress in normal and diseased hCF. hCF from M NF2, M ICM1, or M DCM1 donors were pulsed for 1 h with 0.3 µM TGN and treated with the indicated concentrations of AMG PERK 44 (AMG'44) for 4 days. Cell lysates and medium were used for protein analysis. **A)** Representative immunoblots of intracellular pro-Collagen I (pro-Col I), PERK, BiP, the housekeeping protein GAPDH, and extracellular Collagen I (secreted Col I) for all three hCF donors are shown. The corresponding analyses for the expression of **B)** intracellular pro-Col I and **C)** secreted Col I are given. Protein levels were normalized to GAPDH expression and are given relative to the basal conditions, n=3, p-values assessed by unpaired t-test or 1-way-ANOVA with Tukey's *post hoc* multiple comparisons test.

5.5.3 Inhibition of IRE1α RNase results in Collagen I downregulation

Based on the only partial restoration of intracellular pro-Collagen I expression, the underlying mechanism behind this regulation was further investigated. As the second UPR master regulator IRE1α, which can induce RNA decay (RIDD), could be involved in this process via degradation of the COL1A1 mRNA, 4µ8C was tested as it specifically inhibits the RNase activity of IRE1α. 2D-cultured hCF from Male NF2, Male ICM1, and Male DCM1 donors were treated with 4µ8C for 4 days after ER stress induction with TGN for 1 h. Inhibition of

RIDD by 4μ8C resulted similarly to the PERK inhibitors in a concentration-dependent loss of intracellular pro-Collagen I levels under basal conditions, with a significant downregulation for the highest concentration (Figure 30A, B). However, in the presence of TGN, there was no restoration of intracellular pro-Collagen I levels in any condition for any of the donor cells. This was also the case for expression of extracellular Collagen I (Figure 30A, C). Under high ER stress, the expression of IRE1α was significantly upregulated for the highest concentration when compared to TGN (Figure 30A, D).

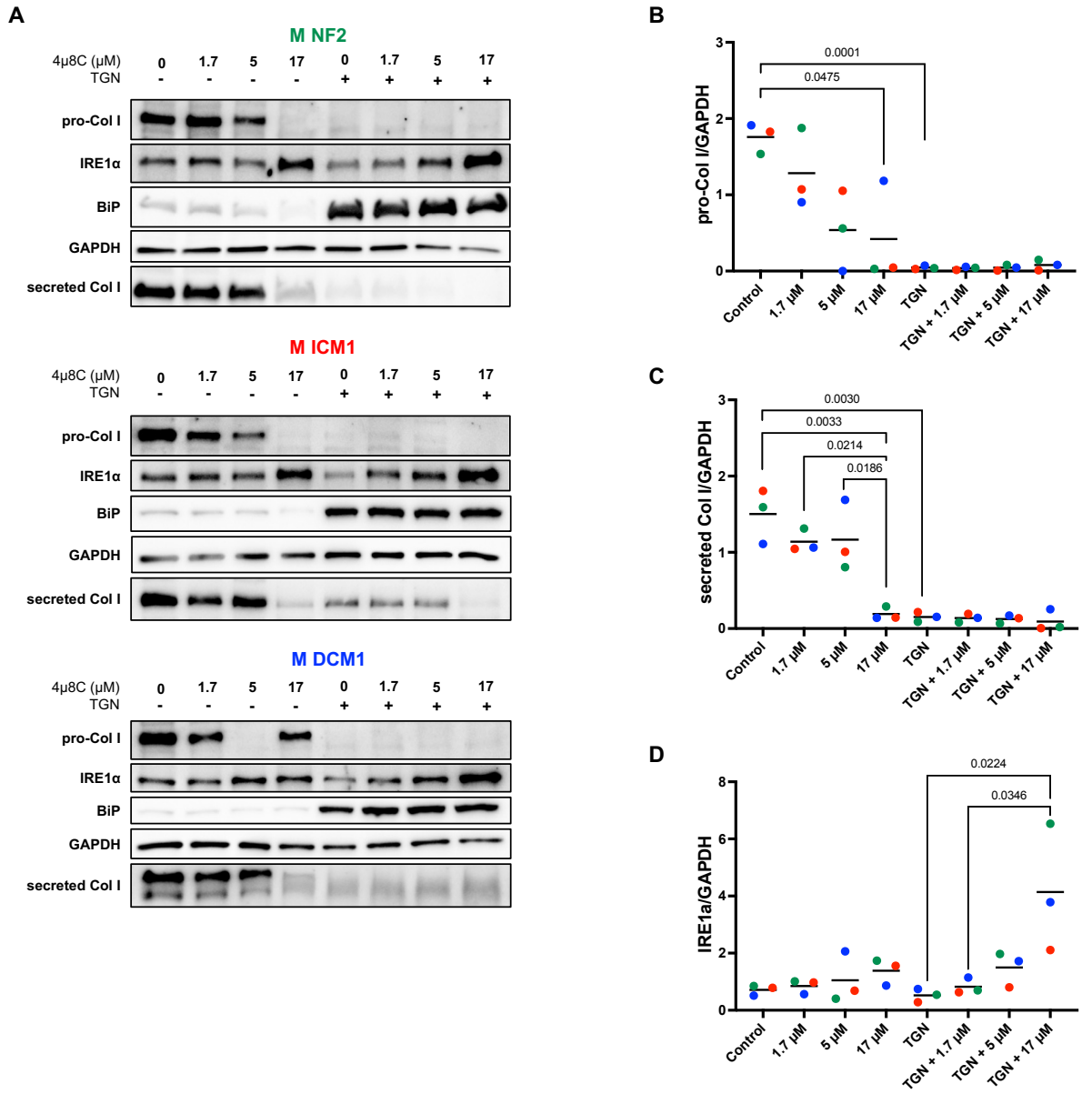

Figure 30. IRE1α RNase inhibition results in a downregulation of pro-Collagen I in normal and diseased hCF. hCF from M NF2 (green), M ICM1 (red), or M DCM1 (blue) donors were pulsed for 1 h with 0.3 μM TGN and treated with the indicated concentrations of 4μ8C for 4 days. Cell lysates and medium were used for protein analysis. **A**) Representative immunoblots of intracellular pro-Collagen I (pro-Col I), IRE1α, BiP, the housekeeping protein GAPDH, and extracellular Collagen I (secreted Col I) for all three hCF donors are shown. The corresponding analyses for the expression of **B**) intracellular pro-Col I, **C**) secreted Col I, and **D**) IRE1α are

given. Protein levels were normalized to GAPDH expression and are given relative to the basal conditions, n=3, p-values assessed by unpaired t-test or 1-way-ANOVA with Tukey's *post hoc* multiple comparisons test.

6 Discussion

During the progression of pathological cardiac remodeling, cardiac fibrosis ensues and is characterized by an extensive amount of ECM proteins secreted by CF within the connective tissue (Travers et al., 2016). As an effective therapy is still lacking, understanding the behavior of CF, as well as correlating the behavior to their phenotypic state, is crucial for the development of anti-fibrotic drugs. However, hCF are difficult to obtain, especially from normal donors. Therefore, hCF from commercial vendors are often used to confirm data of complex animal models or as a basis for tissue engineering, as it is known that the use of 2D models has limitations due to how quickly CF respond to changes in their environment. Depending on the culture conditions, rich medium compositions with undefined serum components, glucose, and other supplements, as well as changes in the environmental mechanics, lead to a rapid transdifferentiation of CF into a diseased phenotype (Hinz, 2007; Tomasek et al., 2002). For instance, it has been shown that the rather high Young's modulus (>1 GPa) of standard cell culture dishes, which is estimated to be five orders of magnitude stiffer than the healthy myocardium, effectively triggers the formation of myofibroblasts (Emig et al., 2021; Travers et al., 2016). Therefore, 2D models do not allow for the study of CF in a comparative physiological setting, considerably limiting translatability.

Furthermore, studies have also shown that CF do adapt their phenotype to their surrounding environment when seeded on or in substrates with varying stiffnesses (Atance et al., 2004; Emig et al., 2020; Shi et al., 2011; Xie et al., 2014; Yeh et al., 2017). However, this approach does not allow for the investigation of dynamic interactions between CF and matrix remodeling. Thus, dynamic models that combine cells with non-polymerized ECM molecules, allowing compaction and remodeling of the ECM over time, are advantageous compared to more static models or 2D culture systems.

6.1 Comparison of non-uniform and uniform ECT properties after 5 days

In recent years, our group has established a dual ECT model that can be used to differentially influence the CF phenotype and the biomechanical properties of the tissues. The only difference in the generation of both ECT types is the geometry of the used molds. We used molds that were equipped with two distant bendable poles (non-uniform model) and molds that contained one central rod (uniform model). In preliminary studies with human CF from one male donor without heart disease (Male NF1), our group was able to demonstrate that ECT

were more compact, stiffer, stronger, less elastic and less extensible in the uniform model than compared to their non-uniform counterparts. To further assess if these differences were dependent on the mold geometry or the hardness of the material properties of the molds, we utilized material properties ranging in hardnesses for both geometries. The data clearly indicated that even the softest material in the uniform model could not give rise to ECT with similar properties in relation to non-uniform ECT prepared with hard, unbendable poles. Moreover, our group demonstrated that the embedded cells in the uniform ECT showed a higher cell cycle activity and more pronounced myofibroblast and ECM signatures than those in the non-uniform ECT. Taken together, these data argue that the geometry is an important determining factor for the phenotypic adaptation of the embedded cells, and these phenotypically different hCF give rise to tissues with distinct biomechanical properties (Santos et al., 2022).

Although these data provided new perspectives, the demonstrated heterogeneity of human CF as seen from scRNA-seq (Farbehi et al., 2019; Koenig et al., 2022; McLellan et al., 2020; Ren et al., 2020; Shang et al., 2022), as well as interindividual differences between humans, made it essential to validate this model with hCF from other donors. Therefore, as one aim of this thesis, hCF from 8 different donors were compared in the dual ECT model. This included human CF from male (Male NF2) and female (Female NF1, Female NF2, and Female NF3) donors without heart disease, as well hCF from male donors with end-stage heart failure, two with ICM (Male ICM1 and Male ICM2) and two with DCM (Male DCM1 and Male DCM2). For comparison to the previously described preliminary results, all initial experiments were performed for a culture period of 5 days. In addition, the contraction analysis of non-uniform ECT generated with Male NF1 hCF seemingly reached a plateau after 5 days, suggesting that a phenotypic steady state was reached.

The data obtained in this thesis demonstrates that all hCF donors reacted to the different geometries similarly by generating significantly stiffer and less extensible ECT in the uniform model than in the non-uniform model after 5 days (Figure 8A, C). Additionally, for all hCF except Male ICM2, the uniform model generated more compact ECT (Figure 6A). Both results are in line with the data seen by the Male NF1 hCF. Moreover, the importance of the geometry as the determining factor was also confirmed for Female NF1 hCF, as the material properties with varying hardnesses led to the same result (Figure 9).

Surprisingly, heterogeneous results were obtained for the longitudinal contraction analysis in the non-uniform model. The measured pole deflection varied between 2 and 22% after 5 days.

Furthermore, not all non-uniform ECT from every donor appeared to have reached a plateau by day 5 (Figure 7A). To better understand the diversity in the contractile ability of the different hCF, ECT contraction was compared to ECT compaction, as both are considered to be dependent on actin-driven processes (Li & Wang, 2011; Vaughan et al., 2019; Wakatsuki et al., 2000; Wakatsuki & Elson, 2002). However, ECT contraction did not correlate with compaction or other biomechanical parameters (Figure 7C).

Other possible explanations for the observed differences could be related to the sex or diseased-states of the donors. Nevertheless, the normal female hCF showed a very high intragroup variance, with Female NF3 generating the lowest and Female NF1 generating the highest contraction of all donors. In addition, Male ICM1 and Male DCM1 hCF contracted very similar to hCF from the normal heart. These explanations do not negate that both the sex and diseased-state can influence the contractile ability. For instance, both Male ICM2 and Male DCM2 contracted very differently than the hCF from the normal heart. In order to obtain statistically valid data, a substantially higher number of hCF from different donors would be necessary.

Another explanation could be contingent on the age of the donor, which has been suggested to be a regulatory factor for other fibroblasts (Kaji et al., 2009; Solé-Boldo et al., 2020). However, a comparison of the different donor ages to the maximal contraction within 5 days did not reveal a significant correlation (data not shown). In addition, the replicative age of the cells could play a role. Unfortunately, when commercial cells are used it is impossible to know how many replicative cycles the cells have experienced. Nevertheless, it is clear that primary CF undergo a phenotypic change after several passages and the number of senescent cells do increase (Chen et al., 2022). Senescence was shown to impact not only the proliferative capacity of cells, but also other features like ECM production and composition and contraction (Meyer et al., 2016; Midgley et al., 2016). To test if the biological age of the hCF influences their contractile ability, Female NF1 hCF, which were derived from a donor 60 years of age, was passaged 8 times. This massively slowed down the proliferation rate (data not shown) and resulted in a significant increase in size according to their cell diameter in suspension (Figure 10A). However, the contraction capacity of this cell was largely unchanged (Figure 10C). Thus, it is not clear what determines the contractile ability of individual hCF. Later discussed changes in gene expression, especially of *ACTA2*, which encodes for the pro-contractile α-SMA, were not conclusive.

Although the regulation of contraction remains obscure, the capacity of ECT compaction could be clearly correlated with the cell size in both models (Figure 6B, C). Moreover, when

generating ECT with passage 8 hCF, the compaction ability was limited compared to passage 4 cells (Figure 10B). In line with this data, the input cells displayed a significantly bigger diameter (Figure 10A). It has been shown that myofibroblasts have increased diameters compared to their fibroblast predecessor (Baxter et al., 2008; Brand et al., 2017; Imaizumi, 1996; Petrov et al., 2000); however, myofibroblasts also show a higher expression of α-SMA (Avery et al., 2018; Hinz et al., 2001; Shinde et al., 2017). Therefore, this higher expression of α-SMA should enforce ECT compaction. Although there is no clear explanation for this observation, one could speculate that either the bigger cell size sterically hinders efficient compaction in a collaborative effort by the whole cell population or the necessary organization of actin is disturbed by the enlarged endomembrane system. Further time course imaging studies investigating the compaction process would be helpful to answer this question.

Of importance in this context might also be that the diseased cells appear bigger in size than the cells from the normal heart. Whether that allows for the classification of their phenotype as a more pronounced myofibroblast compared to cells from the normal heart remains elusive. In general, one cannot rule out that the cells originate from different CF subpopulations, as their local origin is not specified and the isolation protocols of different companies may vary. Regarding the identified differential expression of *THY1*, which is considered to be a myofibroblast marker (Rao et al., 2021), the difference found between two normal female hCF in this thesis demonstrates that there is a relatively high degree of heterogeneity in these commercial cells (Figure 10D).

Despite the relationship between cell size and compaction ability, there was a very strong non-linear inverse correlation identified between ECT stiffness and extensibility, meaning stiffer tissues are less extensible (Figure 8E). This is in line with observations made with native healthy and scarred tissues (Clark, 1996; Corr & Hart, 2013).

6.2 Reactivation of hCF in non-uniform ECT between day 5 and day 13

One unexpected finding in contrast to what was suggested by the preliminary results after a culture period of 5 days was that not all hCF generated non-uniform ECT that reached a contractile plateau. Therefore, we expanded the culture period to 13 days. This demonstrated that there was a clear decrease in ECT compaction and an increase in stiffness between day 5 and 13 for both models and with all investigated hCF (Figure 6A, Figure 8A, Figure 11A, Figure 13A). Thus, indicating that there is no steady state reached, neither in the cellular phenotype nor in the ECM production and degradation. This became especially obvious for the

contraction behavior of some hCF. For example, non-uniform ECT from Male ICM1 resulted in a second phase of contraction after day 7 and Female NF2 ECT increased gradually over the duration of 13 days (Figure 12A).

To better understand these results, a 10 day-wise gene expression analysis of certain myofibroblast markers was performed. These data demonstrated a continuous increase between days 2 and 5 for uniform ECT, whereas expression for non-uniform remained similar within the first 6 days and increased after 10 days (Figure 16A). Furthermore, *ACTA2* expression was shown to parallel ECT contraction until day 4 but increased in expression preceding the second contraction phase for Male ICM1 ECT (Figure 16B).

This temporal regulation in myofibroblast markers between both ECT models effectively explains why the differential expression at day 5 was much more pronounced than at day 13. For instance, Male/Female NF and Male ICM hCF generated ECT that showed a higher transcription of *ACTA2*, *COL1A1*, *POSTN*, *THBS1*, *LUM*, and *CTFG* in the uniform model after 5 days. Whereas Male DCM hCF did not significantly upregulate *ACTA2*, *COL1A1*, *POSTN*, and *THBS1* in the uniform model. Yet, what should also be noted is that the non-uniform Male DCM ECT demonstrated an upregulation of *COL1A1*, *POSTN*, and *LUM* expression already when compared to Male NF or Male ICM ECT, indicating a higher ECM gene signature under lower mechanical strain (Figure 14). This is in line with recent sc and snRNA-seq data investigating DCM donors that displayed higher transcript levels for these specific genes (Chaffin et al., 2022; Koenig et al., 2022). However, after 13 days, intergroup differences were inconsistent and only Male NF2 and Male DCM1 ECT showed an upregulation of *ACTA2*, *POSTN*, and *CTGF* in the uniform model (Figure 15A).

An open question is why this reactivation of the hCF in the non-uniform ECT model takes place after an initial steady phase of gene expression. There are several different possibilities which could account for this result, but all are linked to the non-uniform geometry. It is important to emphasize that there are at least two different mechanical conditions in the non-uniform ECT. One can be found around the pole regions and the other region is in the arm. As described by others, tissues that are suspended in a structure with micropillars and have contact with poles or posts show clearly higher stress levels in these regions, and accordingly, cells with a more pronounced myofibroblast phenotype compared to the cells in the region of the tissue between the poles (Asmani et al., 2018). Consequently, there should be regions with high and low densities of myofibroblasts in the non-uniform ECT, which could result in a crosstalk

between both cells. When taking into consideration different CF subpopulations, this crosstalk could occur due to autocrine signaling, or rather paracrine, as well as from paratensile signals.

For instance, activation of CF around the poles in the non-uniform ECT could lead to diseased phenotypes that secrete the profibrotic cytokine transforming growth factor-ß (TGF-ß), and in turn results in autocrine stimulation of neighboring less activated fibroblasts (Bosman & Stamenkovic, 2003). The formation of a cytokine or growth factor gradient, when a cell secretes an extracellular signaling molecule and the neighboring cell expresses the corresponding receptor, is one argument for cell reactivation after day 5 and further propagation in response to high mechanical stress around the flexible poles or entirely around the central rod. TGF-ß is well-known for its involvement in autocrine signaling and activation of CF through small mothers against decapentaplegic (SMAD) transcription factors, which increase α-SMA, collagen, THBS1, and CTGF expression (Borthwick et al., 2013; M. M. Chen et al., 2000; Leask & Abraham, 2004; Lijnen et al., 2000). By trend, *ACTA2*, *COL1A1*, *THBS1*, and *CTGF* expression in the non-uniform ECT was always slightly higher or the same expression as the uniform ECT after 13 days (Figure 15). However, as the medium is regularly exchanged every second day, it is likely that soluble cytokines, such as TGF-ß, and other factors are washed out, minimizing this gradient accumulation. Another explanation against this argument is based on the ECT RNA sequencing data, where it was shown that expression of TGF-ß variants is not higher in uniform ECT when compared to non-uniform (data not shown). Therefore, it can be speculated that TGF-ß is not higher in the pole area in the non-uniform ECT, as it is the same mechanical condition that the uniform ECT is exposed to. In addition, upon application of TGF-ß to the culture of non-uniform ECT, our group has seen that the shape of the contraction curves remains identical to the intrinsic mechanics of the cell; however, contraction is always enhanced by 2-fold, regardless at which time point TGF-ß is applied (data not shown). If the effect of TGF-ß would be fully active after 5 days, then externally added TGF-ß would have no effect on contraction. As these are only speculative arguments against our data resulting from autocrine signaling, further investigation, e.g., culturing with TGF-ß receptor inhibitors, is necessary to be conclusive.

A second argument for cell reactivation in the pole areas of the non-uniform ECT that are subjected to high mechanical stress is related to paratensile signaling. Liu and colleagues describe paratensile signaling as the crosstalk between myofibroblasts and CF at the fibrotic border zone, where the contractile force of a myofibroblast transmits the mechano-transduction through the fibrous collagen matrices of a CF which it then senses, leading to its activation and

further propagation of the fibrotic area (L. Liu et al., 2020). Paratensile signaling in the high stress vector areas can occur through direct mechanical linking to neighboring cells via cadherins, or by both the myofibroblast and CF binding to the same collagen fibril.

6.3 Protein folding machinery adaptation in uniform ECT and *in vivo* CF subpopulations

Upon cardiac injury, CF undergo a transition into diseased phenotypes, which display a higher secretory activity (Driesen et al., 2014; Elson & Genin, 2016). This process was shown to be accompanied by the induction of ER stress in fibroblasts *in vitro* (Turishcheva et al., 2022). Accordingly, our RNA sequencing data from Male NF1 hCF demonstrated that a more pronounced ECM signature was found in the uniform model and was accompanied by an increased expression of genes involved in protein folding and the UPR (Figure 2), specifically *HSPA5*, *EIF2AK3*, and *DDIT3* (Figure 17). In line with this, recent literature has indicated that similar correlations between ER regulation and ECM production have been found *in vivo* during the course of heart disease. For instance, Xiao et al. demonstrated in a mouse model that genetic deletion of upstream kinases involved in the Hippo kinase cascade resulted in spontaneous fibroblast transdifferentiation, with this subpopulation exemplifying gene signatures related to ER stress and UPR activation, as well as profibrotic factors were detectable (Xiao et al., 2019). Similarly, in this thesis, a sub-analysis was performed between the RNA sequencing of our ECT data and the scRNA-seq data of non-myocytes from healthy and MI mouse hearts, which showed a gene signature related to protein folding, ER stress, and ECM regulation could be transiently detected in an intermediate phenotype subpopulation (F-Cyc) between activated CF and myofibroblasts (Farbehi et al., 2019). Interestingly, McLellan and colleagues demonstrated that in an Ang II-induced model of cardiac fibrosis the ECM signature was more pronounced in female CF than in male CF; however, the degree of fibrosis was clearly lower in the female mouse hearts (McLellan et al., 2020). A possible explanation for this paradox could be due to the fact that in male CF, but not in female CF, genes related to protein folding and ER stress are increased, thus allowing male CF to be able to more efficiently process the secreted cargo load. This led to the hypothesis that interfering with ER adaptation in our ECT model might exert anti-fibrotic effects.

6.4 Effect of PERK inhibition by GSK-2656157 on 2D- and 3D-cultured hCF

To gain more insight into the regulation of ER genes between the different ECT models, an analysis of exemplary genes was performed for ECT generated with hCF from a second donor. Therefore, Male ICM1 hCF were used and a detailed gene expression time course was performed to identify the differences between non-uniform and uniform ECT gene expression at different time points (Figure 16A), as it was shown that clear transcriptional differences were diminished between day 5 and 13 (Figure 14, Figure 15). This supported the notion that the observed regulations are not cell-type specific, although the dynamic in gene regulation appeared to be reflect faster ER adaptation processes (occurring within the first 5 days) and the effects were less pronounced for Male ICM1 ECT. Moreover, the adaptation seemed to occur more prominently in the non-uniform model for Male ICM1 hCF (Figure 21).

As it was hypothesized that interfering with ER adaptation could have anti-fibrotic effects in our dual ECT model, the UPR and its activation in response to misfolded or unfolded proteins was investigated. It is known that the three main UPR regulators, PERK, IRE1α, and ATF6, are initiators of important ER adaptations, including the upregulation of chaperones and co-chaperones to resolve ER stress (Glembotski, 2008; Lenna & Trojanowska, 2012). Additionally, *EIF2AK3* (PERK) expression was found to be most differential in both ECT models base on the RNA sequencing data, and further analysis demonstrated a common regulation of PERK also for Male ICM1 hCF (Figure 20). Therefore, interference with the UPR via PERK inhibition was chosen to test the hypothesis.

Male ICM1 hCF were used to generate non-uniform and uniform ECT, as well as cultured in 2D, and treated with varying concentrations (0.03, 0.3, and 3 µM) of the PERK inhibitor GSK-2656157 (GSK'157). The biomechanical properties of the ECT were assessed after 5 days, and the proliferative activity of the 2D-cultured cells were assessed after 6 days. In addition, the expression of exemplary genes was studied. In brief, it was demonstrated that the compaction, contraction, and stiffness of non-uniform ECT were reduced, whereas in the uniform model no or less pronounced effects were seen (Figure 22). This was paralleled by more prominent changes in gene transcription in the non-uniform model (Figure 24). In line with the hypothesis, PERK inhibition reduced the expression of *COL1A1* and *CTGF* in non-uniform ECT. In addition, an impairment of proliferative abilities was also seen in the 2D-cultured hCF (Figure 25A). It is not clear why the anti-fibrotic effect of the PERK inhibition was more prominent in the non-uniform model; however, one could speculate that this is based on the more pronounced regulation of ER gene expression of this cell in this model as described above.

While the reduction in stiffness might be explained by the lower expression in *COL1A1*, which is the main collagen isoform in hCF, it is unclear how PERK inhibition might affect actin-driven processes, such as compaction and contraction. However, in this context, it has been shown in embryonic mouse fibroblasts that a loss of PERK results in a reorganization of F-actin fibers, suggesting that PERK plays a role in actin polymerization (van Vliet et al., 2017). Whether or not that applies to 3D-cultured hCF remains a question for further investigation.

An interesting finding of these studies was that *DDIT3* expression, a well-known downstream target of PERK, was upregulated in response to PERK inhibition. This increase in *DDIT3* transcript levels was found for both non-uniform and uniform ECT after 5 days (Figure 24I, J), and in 2D after 3 days (Figure 25F).

This finding is in line with a study that found a sustained increase in *DDIT3* expression in a kidney ischemic/reperfusion mouse model (Shu et al., 2018). In addition, another study investigating GSK'157 in PERK-deficient mouse embryonic fibroblasts, found that PERK may promote the adaption of cells to ER stress by inhibiting the proapoptotic function of the tumor suppressor p53 (Krishnamoorthy et al., 2014). Although this study does not give direct insight into the role of DDIT3 regulation, it does provide information to better understand this ER mediator. In contrast to this literature, GSK'157 has also been shown to downregulate DDIT3 on the RNA and protein level (Atkins et al., 2013). Furthermore, a CHOP knockout model attenuated apoptosis in response to ER stress (Panganiban et al., 2019).

Finally, it should be stated that the PERK inhibitor GSK'157 demonstrated a non-linear concentration-dependent response in many applications, with inhibitory effects at 0.03 µM, followed by almost no effect with 0.3 µM and again an inhibitory effect with 3 µM. Although there is no sound explanation, it must be taken into consideration that the inhibitor has been described to have other targets than PERK. For example, it was shown that GSK'157 is a much more potent inhibitor for RIPK1, a kinase involved in TNF-dependent regulation of apoptosis and necrosis, than for PERK (Rojas-Rivera et al., 2017).

Taken together, the exact regulation of CHOP may be dependent on the context in which the cell must adapt, which would also be highly dependent on the intensity of the ER stress. Therefore, in order to have a better overview, the mechanism involved in CHOP induction in response to GSK'157 in hCF needs further clarification. Although the aims of this thesis did not directly unravel this paradox, the indication that UPR activation in response to PERK inhibition may be linked to *COL1A1* regulation was further investigated.

6.5 PERK as a regulator of collagen I under ER stress conditions in 2D-cultured hCF

By treating 2D-cultured hCF from Male NF2, Male ICM1, and Male DCM1 with GSK'157 for 4 days in the absence and presence of the ER stress inducer thapsigargin (TGN), GSK'157 reduced the amount of intracellular secreted pro-Collagen I in a concentration-dependent manner under mild ER stress conditions and partly restored the pro-Collagen 1 levels under high ER stress conditions (Figure 28). The latter could be explained by the argument that PERK induces a translational blockade during ER stress (Harding et al., 1999; Ron, 2002; Y. Shi et al., 1998). However, it has also been demonstrated in the literature that a target of RIDD was collagen IV in mouse embryonic fibroblasts (Hollien et al., 2009), indicating RIDD could play a role in the observed regulation of pro-Collagen I by PERK inhibition under high ER stress conditions. By a more detailed analysis of this hypothesis by 4μ8C, an inhibitor of the RNase activity of IRE1α, it was shown that although pro-Collagen I levels were similarly reduced as the GSK'157 under basal conditions, but no restoration was seen under high ER stress conditions (Figure 30). Therefore, further investigation of the regulation of pro-Collagen I must be pursued.

6.6 Conclusion and outlook

With the work of this doctoral thesis, further validation of our dual ECT model made it possible to identify certain parameters, such as the uniform geometry generates stiffer and less extensible ECT than the non-uniform geometry, and both parameters showed an inverse correlation. Moreover, ECT compaction was closely linked to cell size, whereas ECT contraction was a highly individual parameter. Most hCF generated uniform ECT that showed a higher expression of fibrosis-associated genes, such as *ACTA2*, *POSTN*, *COL1A1*, *CTGF*, and *LUM*, when compared to non-uniform ECT. Finally, the prolongation of our culture period allowed for the identification that no homeostatic steady state was reached between the cellular phenotype and ECM organization.

The mentioned results allow for a better understanding of shared relationships between different analyzed parameters. These shared relationships make it feasible for appropriate drug screening without donor specific features compromising results. In addition, certain parameters could serve to better understand differences between individuals, which is especially important when investigating cells from certain CVD. Furthermore, the reactivation of the non-uniform model can be used to analyze drug effects in a more realistic way by targeting the correct time point needed for pharmacotherapy treatment. This could be beneficial to identify which

processes are affected by certain signal cascades, i.e., when compaction and contraction are affected the actin cytoskeleton may be involved or when stiffness is affected then there may be critical differences in ECM organization.

Additionally, a contribution to a better understanding of the ER adaptive processes involved in the phenotypic switch of CF was accomplished. Inhibiting ER adaptation during the process of fibroblast to myofibroblast transdifferentiation could potentially serve as an anti-fibrotic intervention. Inhibiting PERK did not only limit actin-driven processes, such as compaction and contraction of hCF in 3D but also resulted in an efficient downregulation of the major cardiac collagen isoform COL1A1. However, a general interference with PERK would probably have both favorable and unfavorable consequences, as PERK was demonstrated to have protective functions in cardiomyocytes (Liu et al., 2014). Unfortunately, CF-specific *in vivo* studies that supplement the mainly cardiomyocyte-focused analyses are largely missing, which would allow us to challenge the opinion that UPR activation in the diseased heart helps to protect the myocardium in general.

7 References

Adam, O., Theobald, K., Lavall, D., Grube, M., Kroemer, H. K., Ameling, S., Schäfers, H.-J., Böhm, M., & Laufs, U. (2011). Increased lysyl oxidase expression and collagen cross-linking during atrial fibrillation. *Journal of Molecular and Cellular Cardiology*, *50*(4), 678–685. https://doi.org/10.1016/j.yjmcc.2010.12.019

Aebi, M., Bernasconi, R., Clerc, S., & Molinari, M. (2010). N-glycan structures: Recognition and processing in the ER. *Trends in Biochemical Sciences*, *35*(2), 74–82. https://doi.org/10.1016/j.tibs.2009.10.001

Agah, A., Kyriakides, T. R., Lawler, J., & Bornstein, P. (2002). The lack of thrombospondin-1 (TSP1) dictates the course of wound healing in double-TSP1/TSP2-null mice. *The American Journal of Pathology*, *161*(3), 831–839. https://doi.org/10.1016/S0002-9440(10)64243-5

Alberts, B., Johnson, A., Lewis, J., Raff, M., Roberts, K., & Walter, P. (2002). *Molecular biology of the cell* (4th ed.). Garland Science.

Alberts, B., Johnson, A., Lewis, J., Raff, M., Roberts, K., & Walter, P. (2007). *Molecular biology of the cell* (5th ed.). Garland Science.

Al-Haque, S., Miklas, J. W., Feric, N., Chiu, L. L. Y., Chen, W. L. K., Simmons, C. A., & Radisic, M. (2012). Hydrogel substrate stiffness and topography interact to induce contact guidance in cardiac fibroblasts. *Macromolecular Bioscience*, *12*(10), 1342–1353. https://doi.org/10.1002/mabi.201200042

Anderson, K. R., Sutton, M. G. S. J., & Lie, J. T. (1979). Histopathological types of cardiac fibrosis in myocardial disease. *The Journal of Pathology*, *128*(2), 79–85. https://doi.org/10.1002/path.1711280205

Ao, M., Brewer, B. M., Yang, L., Franco Coronel, O. E., Hayward, S. W., Webb, D. J., & Li, D. (2015). Stretching fibroblasts remodels fibronectin and alters cancer cell migration. *Scientific Reports*, *5*(1), 8334. https://doi.org/10.1038/srep08334

Aragona, M., Panciera, T., Manfrin, A., Giulitti, S., Michielin, F., Elvassore, N., Dupont, S., & Piccolo, S. (2013). A mechanical checkpoint controls multicellular growth through YAP/TAZ regulation by actin-processing factors. *Cell*, *154*(5), 1047–1059. https://doi.org/10.1016/j.cell.2013.07.042

Asmani, M., Velumani, S., Li, Y., Wawrzyniak, N., Hsia, I., Chen, Z., Hinz, B., & Zhao, R. (2018). Fibrotic microtissue array to predict anti-fibrosis drug efficacy. *Nature Communications*, *9*(1), 2066. https://doi.org/10.1038/s41467-018-04336-z

Atance, J., Yost, M. J., & Carver, W. (2004). Influence of the extracellular matrix on the regulation of cardiac fibroblast behavior by mechanical stretch. *Journal of Cellular Physiology*, *200*(3), 377–386. https://doi.org/10.1002/jcp.20034

Atkins, C., Liu, Q., Minthorn, E., Zhang, S.-Y., Figueroa, D. J., Moss, K., Stanley, T. B., Sanders, B., Goetz, A., Gaul, N., Choudhry, A. E., Alsaid, H., Jucker, B. M., Axten, J. M., & Kumar, R. (2013). Characterization of a novel PERK kinase inhibitor with antitumor and antiangiogenic activity. *Cancer Research*, *73*(6), 1993–2002. https://doi.org/10.1158/0008-5472.CAN-12-3109

Avery, D., Govindaraju, P., Jacob, M., Todd, L., Monslow, J., & Puré, E. (2018). Extracellular matrix directs phenotypic heterogeneity of activated fibroblasts. *Matrix Biology*, *67*, 90–106. https://doi.org/10.1016/j.matbio.2017.12.003

Ayala, P., Montenegro, J., Vivar, R., Letelier, A., Urroz, P. A., Copaja, M., Pivet, D., Humeres, C., Troncoso, R., Vicencio, J. M., Lavandero, S., & Díaz-Araya, G. (2012). Attenuation of endoplasmic reticulum stress using the chemical chaperone 4-phenylbutyric acid prevents cardiac fibrosis induced by isoproterenol. *Experimental and Molecular Pathology*, *92*(1), 97–104. https://doi.org/10.1016/j.yexmp.2011.10.012

Baek, H. A., Kim, D. S., Park, H. S., Jang, K. Y., Kang, M. J., Lee, D. G., Moon, W. S., Chae, H. J., & Chung, M. J. (2012). Involvement of endoplasmic reticulum stress in myofibroblastic differentiation of lung fibroblasts. *American Journal of Respiratory Cell and Molecular Biology*, *46*(6), 731–739. https://doi.org/10.1165/rcmb.2011-0121OC

Barnes, L. A., Marshall, C. D., Leavitt, T., Hu, M. S., Moore, A. L., Gonzalez, J. G., Longaker, M. T., & Gurtner, G. C. (2018). Mechanical forces in cutaneous wound healing: Emerging therapies to minimize scar formation. *Advances in Wound Care*, *7*(2), 47–56. https://doi.org/10.1089/wound.2016.0709

Baudino, T. A., Carver, W., Giles, W., & Borg, T. K. (2006). Cardiac fibroblasts: Friend or foe? *American Journal of Physiology-Heart and Circulatory Physiology*, *291*(3), H1015–H1026. https://doi.org/10.1152/ajpheart.00023.2006

Baxter, S. C., Morales, M. O., & Goldsmith, E. C. (2008). Adaptive changes in cardiac fibroblast morphology and collagen organization as a result of mechanical environment. *Cell Biochemistry and Biophysics*, *51*(1), 33–44. https://doi.org/10.1007/s12013-008-9013-8

Bertolotti, A., Zhang, Y., Hendershot, L. M., Harding, H. P., & Ron, D. (2000). Dynamic interaction of BiP and ER stress transducers in the unfolded-protein response. *Nature Cell Biology*, *2*(6), 326–332. https://doi.org/10.1038/35014014

Blackwood, E. A., Azizi, K., Thuerauf, D. J., Paxman, R. J., Plate, L., Kelly, J. W., Wiseman, R. L., & Glembotski, C. C. (2019). Pharmacologic ATF6 activation confers global protection in widespread disease models by reprograming cellular proteostasis. *Nature Communications*, *10*(1), 187. https://doi.org/10.1038/s41467-018-08129-2

Bond, J. E., Kokosis, G., Ren, L., Selim, M. A., Bergeron, A., & Levinson, H. (2011). Wound contraction is attenuated by fasudil inhibition of Rho-associated kinase. *Plastic and Reconstructive Surgery*, *128*(5), 438e–450e. https://doi.org/10.1097/PRS.0b013e31822b7352

Bonnans, C., Chou, J., & Werb, Z. (2014). Remodelling the extracellular matrix in development and disease. *Nature Reviews Molecular Cell Biology*, *15*(12), 786–801. https://doi.org/10.1038/nrm3904

Borthwick, L. A., Wynn, T. A., & Fisher, A. J. (2013). Cytokine mediated tissue fibrosis. *Biochimica et Biophysica Acta (BBA) - Molecular Basis of Disease*, *1832*(7), 1049–1060. https://doi.org/10.1016/j.bbadis.2012.09.014

Bosman, F. T., & Stamenkovic, I. (2003). Functional structure and composition of the extracellular matrix: Structure and composition of the extracellular matrix. *The Journal of Pathology*, *200*(4), 423–428. https://doi.org/10.1002/path.1437

Braakman, I., & Bulleid, N. J. (2011). Protein folding and modification in the mammalian endoplasmic reticulum. *Annual Review of Biochemistry*, *80*(1), 71–99. https://doi.org/10.1146/annurev-biochem-062209-093836

Braakman, I., & Hebert, D. N. (2013). Protein folding in the endoplasmic reticulum. *Cold Spring Harbor Perspectives in Biology*, *5*(5), a013201. https://doi.org/10.1101/cshperspect.a013201

Brand, C. A., Linke, M., Weißenbruch, K., Richter, B., Bastmeyer, M., & Schwarz, U. S. (2017). tension and elasticity contribute to fibroblast cell shape in three dimensions. *Biophysical Journal*, *113*(4), 770–774. https://doi.org/10.1016/j.bpj.2017.06.058

Bukau, B., Weissman, J., & Horwich, A. (2006). Molecular chaperones and protein quality control. *Cell*, *125*(3), 443–451. https://doi.org/10.1016/j.cell.2006.04.014

Burgess, M. L., Carver, W. E., Terracio, L., Wilson, S. P., Wilson, M. A., & Borg, T. K. (1994). Integrin-mediated collagen gel contraction by cardiac fibroblasts. Effects of angiotensin II. *Circulation Research*, *74*(2), 291–298. https://doi.org/10.1161/01.RES.74.2.291

Calfon, M., Zeng, H., Urano, F., Till, J. H., Hubbard, S. R., Harding, H. P., Clark, S. G., & Ron, D. (2002). IRE1 couples endoplasmic reticulum load to secretory capacity by processing the XBP-1 mRNA. *Nature*, *415*(6867), 92–96. https://doi.org/10.1038/415092a

Camelliti, P., Borg, T., & Kohl, P. (2005). Structural and functional characterisation of cardiac fibroblasts. *Cardiovascular Research*, *65*(1), 40–51. https://doi.org/10.1016/j.cardiores.2004.08.020

Cen, B., Selvaraj, A., Burgess, R. C., Hitzler, J. K., Ma, Z., Morris, S. W., & Prywes, R. (2003). Megakaryoblastic leukemia 1, a potent transcriptional coactivator for serum response factor (SRF), is required for serum induction of SRF target genes. *Molecular and Cellular Biology*, *23*(18), 6597–6608. https://doi.org/10.1128/MCB.23.18.6597-6608.2003

Cen, B., Selvaraj, A., & Prywes, R. (2004). Myocardin/MKL family of SRF coactivators: Key regulators of immediate early and muscle specific gene expression. *Journal of Cellular Biochemistry*, *93*(1), 74–82. https://doi.org/10.1002/jcb.20199

Chaffin, M., Papangeli, I., Simonson, B., Akkad, A.-D., Hill, M. C., Arduini, A., Fleming, S. J., Melanson, M., Hayat, S., Kost-Alimova, M., Atwa, O., Ye, J., Bedi, K. C., Nahrendorf, M., Kaushik, V. K., Stegmann, C. M., Margulies, K. B., Tucker, N. R., & Ellinor, P. T. (2022). Single-nucleus profiling of human dilated and hypertrophic cardiomyopathy. *Nature*, *608*(7921), 174–180. https://doi.org/10.1038/s41586-022-04817-8

Chang, H. Y., Chi, J.-T., Dudoit, S., Bondre, C., van de Rijn, M., Botstein, D., & Brown, P. O. (2002). Diversity, topographic differentiation, and positional memory in human fibroblasts. *Proceedings of the National Academy of Sciences*, *99*(20), 12877–12882. https://doi.org/10.1073/pnas.162488599

Chen, C., Li, R., Ross, R. S., & Manso, A. M. (2016). Integrins and integrin-related proteins in cardiac fibrosis. *Journal of Molecular and Cellular Cardiology*, *93*, 162–174. https://doi.org/10.1016/j.yjmcc.2015.11.010

Chen, M. M., Lam, A., Abraham, J. A., Schreiner, G. F., & Joly, A. H. (2000). CTGF expression is induced by TGF- in cardiac fibroblasts and cardiac myocytes: A potential role in heart fibrosis. *Journal of Molecular and Cellular Cardiology*, *32*, 1805–1819. https://doi.org/10.1006/2000.1215

Chen, M. S., Lee, R. T., & Garbern, J. C. (2022). Senescence mechanisms and targets in the heart. *Cardiovascular Research*, *118*(5), 1173–1187. https://doi.org/10.1093/cvr/cvab161

Chen, X., Shen, J., & Prywes, R. (2002). The luminal domain of ATF6 senses endoplasmic reticulum (ER) stress and causes translocation of ATF6 from the ER to the golgi. *Journal of Biological Chemistry*, *277*(15), 13045–13052. https://doi.org/10.1074/jbc.M110636200

Chevet, E., Smirle, J., Cameron, P. H., Thomas, D. Y., & Bergeron, J. J. M. (2010). Calnexin phosphorylation: Linking cytoplasmic signalling to endoplasmic reticulum lumenal functions. *Seminars in Cell & Developmental Biology*, *21*(5), 486–490. https://doi.org/10.1016/j.semcdb.2009.12.005

Clark, J. A., Cheng, J. C. Y., & Leung, K. S. (1996). Mechanical properties of normal skin and hypertrophic scars. *Burns*, *22*(6), 443–446. https://doi.org/10.1016/0305-4179(96)00038-1

Cleutjens, J., Kandala, J., Guarda, E., Guntaka, R., & Weber, K. (1995). Regulation of collagen degradation in the rat myocardium after infarction. *Journal of Molecular and Cellular Cardiology*, *27*(6), 1281–1292. https://doi.org/10.1016/S0022-2828(05)82390-9

Corr, D. T., & Hart, D. A. (2013). Biomechanics of Scar Tissue and Uninjured Skin. *Advances in Wound Care*, *2*(2), 37–43. https://doi.org/10.1089/wound.2011.0321

Cross, B. C. S., Bond, P. J., Sadowski, P. G., Jha, B. K., Zak, J., Goodman, J. M., Silverman, R. H., Neubert, T. A., Baxendale, I. R., Ron, D., & Harding, H. P. (2012). The molecular basis for selective inhibition of unconventional mRNA splicing by an IRE1-binding small molecule. *Proceedings of the National Academy of Sciences*, *109*(15). https://doi.org/10.1073/pnas.1115623109

Cyr, D. M., Lu, X., & Douglas, M. G. (1992). Regulation of Hsp70 function by a eukaryotic DnaJ homolog. *Journal of Biological Chemistry*, *267*(29), 20927–20931. https://doi.org/10.1016/S0021-9258(19)36777-8

Dallon, J. C., & Ehrlich, H. P. (2008). A review of fibroblast-populated collagen lattices. *Wound Repair and Regeneration*, *16*(4), 472–479. https://doi.org/10.1111/j.1524-475X.2008.00392.x

Driesen, R. B., Nagaraju, C. K., Abi-Char, J., Coenen, T., Lijnen, P. J., Fagard, R. H., Sipido, K. R., & Petrov, V. V. (2014). Reversible and irreversible differentiation of cardiac fibroblasts. *Cardiovascular Research*, *101*(3), 411–422. https://doi.org/10.1093/cvr/cvt338

Dupont, S., Morsut, L., Aragona, M., Enzo, E., Giulitti, S., Cordenonsi, M., Zanconato, F., Le Digabel, J., Forcato, M., Bicciato, S., Elvassore, N., & Piccolo, S. (2011). Role of YAP/TAZ in mechanotransduction. *Nature*, *474*(7350), 179–183. https://doi.org/10.1038/nature10137

Dupuis, L. E., Berger, M. G., Feldman, S., Doucette, L., Fowlkes, V., Chakravarti, S., Thibaudeau, S., Alcala, N. E., Bradshaw, A. D., & Kern, C. B. (2015). Lumican deficiency results In cardiomyocyte hypertrophy with altered collagen assembly. *Journal of Molecular and Cellular Cardiology*, *84*, 70–80. https://doi.org/10.1016/j.yjmcc.2015.04.007

Dworatzek, E., Mahmoodzadeh, S., Schriever, C., Kusumoto, K., Kramer, L., Santos, G., Fliegner, D., Leung, Y.-K., Ho, S.-M., Zimmermann, W.-H., Lutz, S., & Regitz-Zagrosek, V. (2019). Sex-specific regulation of collagen I and III expression by 17β-Estradiol in cardiac fibroblasts: Role of estrogen receptors. *Cardiovascular Research*, *115*(2), 315–327. https://doi.org/10.1093/cvr/cvy185

Ellgaard, L., & Helenius, A. (2003). Quality control in the endoplasmic reticulum. *Nature Reviews Molecular Cell Biology*, *4*(3), 181–191. https://doi.org/10.1038/nrm1052

Ellis, R. J., & Van der Vies, S. M. (1991). Molecular chaperones. *Annual Review of Biochemistry*, *60*, 321–347. https://doi.org/10.1146/annurev.bi.60.070191.001541

Elosegui-Artola, A., Oria, R., Chen, Y., Kosmalska, A., Pérez-González, C., Castro, N., Zhu, C., Trepat, X., & Roca-Cusachs, P. (2016). Mechanical regulation of a molecular clutch defines force transmission and transduction in response to matrix rigidity. *Nature Cell Biology*, *18*(5), 540–548. https://doi.org/10.1038/ncb3336

Elson, E. L., & Genin, G. M. (2016). Tissue constructs: Platforms for basic research and drug discovery. *Interface Focus*, *6*(1), 20150095. https://doi.org/10.1098/rsfs.2015.0095

Emig, R., Zgierski-Johnston, C. M., Beyersdorf, F., Rylski, B., Ravens, U., Weber, W., Kohl, P., Hörner, M., & Peyronnet, R. (2020). Human atrial fibroblast adaptation to heterogeneities in substrate stiffness. *Frontiers in Physiology*, *10*, 1526. https://doi.org/10.3389/fphys.2019.01526

Emig, R., Zgierski-Johnston, C. M., Timmermann, V., Taberner, A. J., Nash, M. P., Kohl, P., & Peyronnet, R. (2021). Passive myocardial mechanical properties: Meaning, measurement, models. *Biophysical Reviews*, *13*(5), 587–610. https://doi.org/10.1007/s12551-021-00838-1

Esnault, C., Stewart, A., Gualdrini, F., East, P., Horswell, S., Matthews, N., & Treisman, R. (2014). Rho-actin signaling to the MRTF coactivators dominates the immediate transcriptional response to serum in fibroblasts. *Genes & Development*, *28*(9), 943–958. https://doi.org/10.1101/gad.239327.114

Farbehi, N., Patrick, R., Dorison, A., Xaymardan, M., Janbandhu, V., Wystub-Lis, K., Ho, J. W., Nordon, R. E., & Harvey, R. P. (2019). Single-cell expression profiling reveals dynamic flux of cardiac stromal, vascular and immune cells in health and injury. *ELife*, *8*, e43882. https://doi.org/10.7554/eLife.43882

Fliegel, L., Burns, K., MacLennan, D. H., Reithmeier, R. A., & Michalak, M. (1989). Molecular cloning of the high affinity calcium-binding protein (calreticulin) of skeletal muscle sarcoplasmic reticulum. *Journal of Biological Chemistry*, *264*(36), 21522–21528. https://doi.org/10.1016/S0021-9258(20)88216-7

Flores, R. O. R., Lanzer, J. D., Holland, C. H., Leuschner, F., Most, P., Schultz, J.-H., Levinson, R. T., & Saez-Rodriguez, J. (2021). A consensus transcriptional landscape of human end-stage heart failure. *Journal of the American Heart Association*, *10*(7), e019667. https://doi.org/10.1161/JAHA.120.019667

Francisco, J., Zhang, Y., Jeong, J. I., Mizushima, W., Ikeda, S., Ivessa, A., Oka, S., Zhai, P., Tallquist, M. D., & Del Re, D. P. (2020). Blockade of fibroblast YAP attenuates cardiac fibrosis and dysfunction through MRTF-A inhibition. *JACC: Basic to Translational Science*, *5*(9), 931–945. https://doi.org/10.1016/j.jacbts.2020.07.009

Frangogiannis, N. G. (2012). Matricellular proteins in cardiac adaptation and disease. *Physiological Reviews*, *92*(2), 635–688. https://doi.org/10.1152/physrev.00008.2011

Fu, H. Y., Okada, K., Liao, Y., Tsukamoto, O., Isomura, T., Asai, M., Sawada, T., Okuda, K., Asano, Y., Sanada, S., Asanuma, H., Asakura, M., Takashima, S., Komuro, I., Kitakaze, M., & Minamino, T. (2010). Ablation of C/EBP homologous protein attenuates endoplasmic reticulum–mediated apoptosis and cardiac dysfunction induced by pressure overload. *Circulation*, *122*(4), 361–369. https://doi.org/10.1161/CIRCULATIONAHA.109.917914

Glembotski, C. C. (2008). The role of the unfolded protein response in the heart. *Journal of Molecular and Cellular Cardiology*, *44*(3), 453–459. https://doi.org/10.1016/j.yjmcc.2007.10.017

Groenendyk, J., Lee, D., Jung, J., Dyck, J. R. B., Lopaschuk, G. D., Agellon, L. B., & Michalak, M. (2016). Inhibition of the unfolded protein response mechanism prevents cardiac fibrosis. *PLoS ONE*, *11*(7). https://doi.org/10.1371/journal.pone.0159682

Guettler, S., Vartiainen, M. K., Miralles, F., Larijani, B., & Treisman, R. (2008). RPEL motifs link the serum response factor cofactor MAL but not myocardin to Rho signaling via actin binding. *Molecular and Cellular Biology*, *28*(2), 732–742. https://doi.org/10.1128/MCB.01623-07

Gurtner, G. C., Werner, S., Barrandon, Y., & Longaker, M. T. (2008). Wound repair and regeneration. *Nature*, *453*(7193), 314–321. https://doi.org/10.1038/nature07039

Hamada, H., Suzuki, M., Yuasa, S., Mimura, N., Shinozuka, N., Takada, Y., Suzuki, M., Nishino, T., Nakaya, H., Koseki, H., & Aoe, T. (2004). Dilated cardiomyopathy caused by aberrant endoplasmic reticulum quality control in mutant KDEL receptor transgenic mice. *Molecular and Cellular Biology*, *24*(18), 8007–8017. https://doi.org/10.1128/MCB.24.18.8007-8017.2004

Han, D., Lerner, A. G., Vande Walle, L., Upton, J.-P., Xu, W., Hagen, A., Backes, B. J., Oakes, S. A., & Papa, F. R. (2009). IRE1α kinase activation modes control alternate endoribonuclease outputs to determine divergent cell fates. *Cell*, *138*(3), 562–575. https://doi.org/10.1016/j.cell.2009.07.017

Harding, H. P., Novoa, I., Zhang, Y., Zeng, H., Wek, R., Schapira, M., & Ron, D. (2000). Regulated translation initiation controls stress-induced gene expression in mammalian cells. *Molecular Cell*, *6*(5), 1099–1108. https://doi.org/10.1016/S1097-2765(00)00108-8

Harding, H. P., Zhang, Y., & Ron, D. (1999). Protein translation and folding are coupled by an endoplasmic-reticulum-resident kinase. *Nature*, *397*(6716), 271–274. https://doi.org/10.1038/16729

Harding, H. P., Zhang, Y., Zeng, H., Novoa, I., Lu, P. D., Calfon, M., Sadri, N., Yun, C., Popko, B., Paules, R., Stojdl, D. F., Bell, J. C., Hettmann, T., Leiden, J. M., & Ron, D. (2003). An integrated stress response regulates amino acid metabolism and resistance to oxidative stress. *Molecular Cell*, *11*(3), 619–633. https://doi.org/10.1016/S1097-2765(03)00105-9

Hebert, D. N., Garman, S. C., & Molinari, M. (2005). The glycan code of the endoplasmic reticulum: Asparagine-linked carbohydrates as protein maturation and quality-control tags. *Trends in Cell Biology*, *15*(7), 364–370. https://doi.org/10.1016/j.tcb.2005.05.007

Hebert, D. N., & Molinari, M. (2007). In and out of the ER: Protein folding, quality control, degradation, and related human diseases. *Physiological Reviews*, *87*(4), 1377–1408. https://doi.org/10.1152/physrev.00050.2006

Helenius, A., & Aebi, M. (2004). Roles of N-linked glycans in the endoplasmic reticulum. *Annual Review of Biochemistry*, *73*(1), 1019–1049. https://doi.org/10.1146/annurev.biochem.73.011303.073752

Hetz, C. (2012). The unfolded protein response: Controlling cell fate decisions under ER stress and beyond. *Nature Reviews Molecular Cell Biology*, *13*(2), Article 2. https://doi.org/10.1038/nrm3270

Hill, C. S., Wynne, J., & Treisman, R. (1995). The Rho family GTPases RhoA, Rac1, and CDC42Hs regulate transcriptional activation by SRF. *Cell*, *81*(7), 1159–1170. https://doi.org/10.1016/s0092-8674(05)80020-0

Hinz, B. (2007). Formation and function of the myofibroblast during tissue repair. *Journal of Investigative Dermatology*, *127*(3), 526–537. https://doi.org/10.1038/sj.jid.5700613

Hinz, B., Celetta, G., Tomasek, J. J., Gabbiani, G., & Chaponnier, C. (2001). Alpha-smooth muscle actin expression upregulates fibroblast contractile activity. *Molecular Biology of the Cell*, *12*(9), 2730–2741. https://doi.org/10.1091/mbc.12.9.2730

Hinz, B., Phan, S. H., Thannickal, V. J., Galli, A., Bochaton-Piallat, M.-L., & Gabbiani, G. (2007). The myofibroblast. *The American Journal of Pathology*, *170*(6), 1807–1816. https://doi.org/10.2353/ajpath.2007.070112

Hollien, J., Lin, J. H., Li, H., Stevens, N., Walter, P., & Weissman, J. S. (2009). Regulated IRE1-dependent decay of messenger RNAs in mammalian cells. *Journal of Cell Biology*, *186*(3), 323–331. https://doi.org/10.1083/jcb.200903014

Hollien, J., & Weissman, J. S. (2006). Decay of endoplasmic reticulum-localized mRNAs during the unfolded protein response. *Science*, *313*(5783), 104–107. https://doi.org/10.1126/science.1129631

Horimoto, S., Ninagawa, S., Okada, T., Koba, H., Sugimoto, T., Kamiya, Y., Kato, K., Takeda, S., & Mori, K. (2013). The unfolded protein response transducer ATF6 represents a novel transmembrane-type endoplasmic reticulum-associated degradation substrate requiring both mannose trimming and SEL1L protein. *Journal of Biological Chemistry*, *288*(44), 31517–31527. https://doi.org/10.1074/jbc.M113.476010

Hsu, S.-K., Chiu, C.-C., Dahms, H.-U., Chou, C.-K., Cheng, C.-M., Chang, W.-T., Cheng, K.-C., Wang, H.-M. D., & Lin, I.-L. (2019). Unfolded protein response (UPR) in survival, dormancy, immunosuppression, metastasis, and treatments of cancer cells. *International Journal of Molecular Sciences*, *20*(10), 2518. https://doi.org/10.3390/ijms20102518

Hwang, J., & Qi, L. (2018). Quality control in the endoplasmic reticulum: Crosstalk between ERAD and UPR pathways. *Trends in Biochemical Sciences*, *43*(8), 593–605. https://doi.org/10.1016/j.tibs.2018.06.005

Imaizumi, T. (1996). Effect of human basic fibroblast growth factor on fibroblast proliferation, cell volume, collagen lattice contraction: In comparison with acidic type. *Journal of Dermatological Science*, *11*(2), 134–141. https://doi.org/10.1016/0923-1811(95)00431-9

Jatho, A., Hartmann, S., Kittana, N., Mügge, F., Wuertz, C. M., Tiburcy, M., Zimmermann, W.-H., Katschinski, D. M., & Lutz, S. (2015). RhoA ambivalently controls prominent myofibroblast characteritics by involving distinct signaling routes. *PLOS ONE*, *10*(10), e0137519. https://doi.org/10.1371/journal.pone.0137519

Jiang, J., Prasad, K., Lafer, E. M., & Sousa, R. (2005). Structural basis of interdomain communication in the Hsc70 chaperone. *Molecular Cell*, *20*(4), 513–524. https://doi.org/10.1016/j.molcel.2005.09.028

Johnson, L. A., Rodansky, E. S., Haak, A. J., Larsen, S. D., Neubig, R. R., & Higgins, P. D. R. (2014). Novel Rho/MRTF/SRF inhibitors block matrix-stiffness and TGF-β–induced fibrogenesis in human colonic myofibroblasts. *Inflammatory Bowel Diseases*, *20*(1), 154–165. https://doi.org/10.1097/01.MIB.0000437615.98881.31

Jonas, O., & Duschl, C. (2010). Force propagation and force generation in cells. *Cytoskeleton*, *67*(9), 555–563. https://doi.org/10.1002/cm.20466

Joy, M., Gau, D., Castellucci, N., Prywes, R., & Roy, P. (2017). The myocardin-related transcription factor MKL co-regulates the cellular levels of two profilin isoforms. *The Journal of Biological Chemistry*, *292*(28), 11777–11791. https://doi.org/10.1074/jbc.M117.781104

Kaji, K., Ohta, T., Horie, N., Naru, E., Hasegawa, M., & Kanda, N. (2009). Donor age reflects the replicative lifespan of human fibroblasts in culture. *Human Cell*, *22*(2), 38–42. https://doi.org/10.1111/j.1749-0774.2009.00066.x

Kassan, M., Galán, M., Partyka, M., Saifudeen, Z., Henrion, D., Trebak, M., & Matrougui, K. (2012). Endoplasmic reticulum stress is involved in cardiac damage and vascular endothelial dysfunction in hypertensive mice. *Arteriosclerosis, Thrombosis, and Vascular Biology*, *32*(7), 1652–1661. https://doi.org/10.1161/ATVBAHA.112.249318

Koenig, A. L., Shchukina, I., Amrute, J., Andhey, P. S., Zaitsev, K., Lai, L., Bajpai, G., Bredemeyer, A., Smith, G., Jones, C., Terrebonne, E., Rentschler, S. L., Artyomov, M. N., & Lavine, K. J. (2022). Single-cell transcriptomics reveals cell-type-specific diversification in human heart failure. *Nature Cardiovascular Research*, *1*(3), 263–280. https://doi.org/10.1038/s44161-022-00028-6

Krebs, J., Groenendyk, J., & Michalak, M. (2011). Ca^{2+}-signaling, alternative splicing and endoplasmic reticulum stress responses. *Neurochemical Research*, *36*(7), 1198–1211. https://doi.org/10.1007/s11064-011-0431-4

Krishnamoorthy, J., Rajesh, K., Mirzajani, F., Kesoglidou, P., Papadakis, A., & Koromilas, A. E. (2014). Evidence for eIF2α phosphorylation-independent effects of GSK2656157, a novel catalytic inhibitor of PERK with clinical implications. *Cell Cycle*, *13*(5), 801–806. https://doi.org/10.4161/cc.27726

Krishnan, A., Li, X., Kao, W.-Y., Viker, K., Butters, K., Masuoka, H., Knudsen, B., Gores, G., & Charlton, M. (2012). Lumican, an extracellular matrix proteoglycan, is a novel requisite for hepatic fibrosis. *Laboratory Investigation*, *92*(12), 1712–1725. https://doi.org/10.1038/labinvest.2012.121

Kuwahara, F., Kai, H., Tokuda, K., Kai, M., Takeshita, A., Egashira, K., & Imaizumi, T. (2002). Transforming growth factor-β function blocking prevents myocardial fibrosis and diastolic dysfunction in pressure-overloaded rats. *Circulation*, *106*(1), 130–135. https://doi.org/10.1161/01.CIR.0000020689.12472.E0

Leask, A. (2010). Potential therapeutic targets for cardiac fibrosis: TGFβ, angiotensin, endothelin, CCN2, and PDGF, partners in fibroblast activation. *Circulation Research*, *106*(11), 1675–1680. https://doi.org/10.1161/CIRCRESAHA.110.217737

Leask, A. (2013). Integrin β1: A mechanosignaling sensor essential for connective tissue deposition by fibroblasts. *Advances in Wound Care*, *2*(4), 160–166. https://doi.org/10.1089/wound.2012.0365

Leask, A., & Abraham, D. J. (2004). TGF-β signaling and the fibrotic response. *The FASEB Journal*, *18*(7), 816–827. https://doi.org/10.1096/fj.03-1273rev

Lee, A.-H., Iwakoshi, N. N., & Glimcher, L. H. (2003). XBP-1 regulates a subset of endoplasmic reticulum resident chaperone genes in the unfolded protein response. *Molecular and Cellular Biology*, *23*(21), 7448–7459. https://doi.org/10.1128/MCB.23.21.7448-7459.2003

Lenna, S., & Trojanowska, M. (2012). The role of endoplasmic reticulum stress and the unfolded protein response in fibrosis. *Current Opinion in Rheumatology*, *24*(6), 663–668. https://doi.org/10.1097/BOR.0b013e3283588dbb

Li, B., & Wang, J. H.-C. (2011). Fibroblasts and myofibroblasts in wound healing: Force generation and measurement. *Journal of Tissue Viability*, *20*(4), 108–120. https://doi.org/10.1016/j.jtv.2009.11.004

Li, Y., Guo, Y., Tang, J., Jiang, J., & Chen, Z. (2014). New insights into the roles of CHOP-induced apoptosis in ER stress. *Acta Biochimica et Biophysica Sinica*, *46*(8), 629–640. https://doi.org/10.1093/abbs/gmu048

Lijnen, P. J., Petrov, V. V., & Fagard, R. H. (2000). Induction of cardiac fibrosis by transforming growth factor-β1. *Molecular Genetics and Metabolism*, *71*(1–2), 418–435. https://doi.org/10.1006/mgme.2000.3032

Litviňuková, M., Talavera-López, C., Maatz, H., Reichart, D., Worth, C. L., Lindberg, E. L., Kanda, M., Polanski, K., Heinig, M., Lee, M., Nadelmann, E. R., Roberts, K., Tuck, L., Fasouli, E. S., DeLaughter, D. M., McDonough, B., Wakimoto, H., Gorham, J. M., Samari, S., … Teichmann, S. A. (2020). Cells of the adult human heart. *Nature*, *588*(7838), 466–472. https://doi.org/10.1038/s41586-020-2797-4

Liu, C. Y., Schröder, M., & Kaufman, R. J. (2000). Ligand-independent dimerization activates the stress response kinases IRE1 and PERK in the lumen of the endoplasmic reticulum. *Journal of Biological Chemistry*, *275*(32), 24881–24885. https://doi.org/10.1074/jbc.M004454200

Liu, F., Lagares, D., Choi, K. M., Stopfer, L., Marinković, A., Vrbanac, V., Probst, C. K., Hiemer, S. E., Sisson, T. H., Horowitz, J. C., Rosas, I. O., Fredenburgh, L. E., Feghali-Bostwick, C., Varelas, X., Tager, A. M., & Tschumperlin, D. J. (2015). Mechanosignaling through YAP and TAZ drives fibroblast activation and fibrosis. *American Journal of Physiology. Lung Cellular and Molecular Physiology*, *308*(4), L344-357. https://doi.org/10.1152/ajplung.00300.2014

Liu, L., Yu, H., Zhao, H., Wu, Z., Long, Y., Zhang, J., Yan, X., You, Z., Zhou, L., Xia, T., Shi, Y., Xiao, B., Wang, Y., Huang, C., & Du, Y. (2020). Matrix-transmitted paratensile signaling enables myofibroblast-fibroblast cross talk in fibrosis expansion. *Proceedings of the National Academy of Sciences*, *117*(20), 10832–10838. https://doi.org/10.1073/pnas.1910650117

Liu, X., Kwak, D., Lu, Z., Xu, X., Fassett, J., Wang, H., Wei, Y., Cavener, D. R., Hu, X., Hall, J., Bache, R. J., & Chen, Y. (2014). Endoplasmic reticulum stress sensor protein kinase R–like endoplasmic reticulum kinase (PERK) protects against pressure overload–induced heart failure and lung remodeling. *Hypertension*, *64*(4), 738–744. https://doi.org/10.1161/HYPERTENSIONAHA.114.03811

López, B., Querejeta, R., González, A., Larman, M., & Díez, J. (2012). Collagen cross-linking but not collagen amount associates with elevated filling pressures in hypertensive patients with stage C heart failure: Potential role of lysyl oxidase. *Hypertension*, *60*(3), 677–683. https://doi.org/10.1161/HYPERTENSIONAHA.112.196113

Lu, P. D., Harding, H. P., & Ron, D. (2004). Translation reinitiation at alternative open reading frames regulates gene expression in an integrated stress response. *Journal of Cell Biology*, *167*(1), 27–33. https://doi.org/10.1083/jcb.200408003

Marijianowski, M. M. H., Teeling, P., Mann, J., & Becker, A. E. (1995). Dilated cardiomyopathy is associated with an increase in the type I/type III collagen ratio: A quantitative assessment. *Journal of the American College of Cardiology*, *25*(6), 1263–1272. https://doi.org/10.1016/0735-1097(94)00557-7

Maruhashi, T., Kii, I., Saito, M., & Kudo, A. (2010). Interaction between periostin and BMP-1 promotes proteolytic activation of lysyl oxidase. *Journal of Biological Chemistry*, *285*(17), 13294–13303. https://doi.org/10.1074/jbc.M109.088864

Mayer, M. P., & Bukau, B. (2005). Hsp70 chaperones: Cellular functions and molecular mechanism. *Cellular and Molecular Life Sciences*, *62*(6), 670–684. https://doi.org/10.1007/s00018-004-4464-6

Mayer, M. P., & Gierasch, L. M. (2019). Recent advances in the structural and mechanistic aspects of Hsp70 molecular chaperones. *Journal of Biological Chemistry*, *294*(6), 2085–2097. https://doi.org/10.1074/jbc.REV118.002810

McCullough, K. D., Martindale, J. L., Klotz, L.-O., Aw, T.-Y., & Holbrook, N. J. (2001). GADD153 sensitizes cells to endoplasmic reticulum stress by down-regulating Bcl2 and perturbing the cellular redox state. *Molecular and Cellular Biology*, *21*(4), 1249–1259. https://doi.org/10.1128/MCB.21.4.1249-1259.2001

McLellan, M. A., Skelly, D. A., Dona, M. S. I., Squiers, G. T., Farrugia, G. E., Gaynor, T. L., Cohen, C. D., Pandey, R., Diep, H., Vinh, A., Rosenthal, N. A., & Pinto, A. R. (2020). High-resolution transcriptomic profiling of the heart during chronic stress reveals cellular drivers of cardiac fibrosis and hypertrophy. *Circulation*, *142*(15), 1448–1463. https://doi.org/10.1161/CIRCULATIONAHA.119.045115

Melnick, J., Dul, J. L., & Argon, Y. (1994). Sequential interaction of the chaperones BiP and GRP94 with immunoglobulin chains in the endoplasmic reticulum. *Nature*, *370*(6488), 373–375. https://doi.org/10.1038/370373a0

Meyer, K., Hodwin, B., Ramanujam, D., Engelhardt, S., & Sarikas, A. (2016). Essential role for premature senescence of myofibroblasts in myocardial fibrosis. *Journal of the American College of Cardiology*, *67*(17), 2018–2028. https://doi.org/10.1016/j.jacc.2016.02.047

Midgley, A. C., Morris, G., Phillips, A. O., & Steadman, R. (2016). 17β-estradiol ameliorates age-associated loss of fibroblast function by attenuating IFN-γ/STAT1-dependent miR-7 upregulation. *Aging Cell*, *15*(3), 531–541. https://doi.org/10.1111/acel.12462

Mikami, Y., Matsuzaki, H., Takeshima, H., Makita, K., Yamauchi, Y., & Nagase, T. (2016). Development of an in vitro assay to evaluate contractile function of mesenchymal cells that underwent epithelial-mesenchymal transition. *Journal of Visualized Experiments*, *112*, 53974. https://doi.org/10.3791/53974

Minamino, T., Komuro, I., & Kitakaze, M. (2010). Endoplasmic reticulum stress as a therapeutic target in cardiovascular disease. *Circulation Research*, *107*(9), 1071–1082. https://doi.org/10.1161/CIRCRESAHA.110.227819

Miralles, F., Posern, G., Zaromytidou, A.-I., & Treisman, R. (2003). Actin dynamics control SRF activity by regulation of its coactivator MAL. *Cell*, *113*(3), 329–342. https://doi.org/10.1016/s0092-8674(03)00278-2

Morisco, C., Sadoshima, J., Trimarco, B., Arora, R., Vatner, D. E., & Vatner, S. F. (2003). Is treating cardiac hypertrophy salutary or detrimental: The two faces of Janus. *American Journal of Physiology-Heart and Circulatory Physiology*, *284*(4), H1043–H1047. https://doi.org/10.1152/ajpheart.00990.2002

Muggleton-Harris, A. L., & Hayflick, L. (1976). Cellular aging studied by the reconstruction of replicating cells from nuclei and cytoplasms isolated from normal human diploid cells. *Experimental Cell Research*, *103*(2), 321–330. https://doi.org/10.1016/0014-4827(76)90269-X

Norman, C., Runswick, M., Pollock, R., & Treisman, R. (1988). Isolation and properties of cDNA clones encoding SRF, a transcription factor that binds to the c-fos serum response element. *Cell*, *55*(6), 989–1003. https://doi.org/10.1016/0092-8674(88)90244-9

Novoa, I., Zeng, H., Harding, H. P., & Ron, D. (2001). Feedback inhibition of the unfolded protein response by GADD34-mediated dephosphorylation of eIF2α. *The Journal of Cell Biology*, *153*(5), 1011–1021.

Oflaz, H., & Baran, O. (2014). A new medical device to measure a stiffness of soft materials. *Acta of Bioengineering and Biomechanics*, *16*(1), 125–131. https://doi.org/10.5277/ABB140115

Oka, T., Xu, J., Kaiser, R. A., Melendez, J., Hambleton, M., Sargent, M. A., Lorts, A., Brunskill, E. W., Dorn, G. W., Conway, S. J., Aronow, B. J., Robbins, J., & Molkentin, J. D. (2007). Genetic manipulation of periostin expression reveals a role in cardiac hypertrophy and ventricular remodeling. *Circulation Research*, *101*(3), 313–321. https://doi.org/10.1161/CIRCRESAHA.107.149047

Olson, E. N., & Nordheim, A. (2010). Linking actin dynamics and gene transcription to drive cellular motile functions. *Nature Reviews Molecular Cell Biology*, *11*(5), 353–365. https://doi.org/10.1038/nrm2890

Ongherth, A., Pasch, S., Wuertz, C. M., Nowak, K., Kittana, N., Weis, C. A., Jatho, A., Vettel, C., Tiburcy, M., Toischer, K., Hasenfuss, G., Zimmermann, W.-H., Wieland, T., & Lutz, S. (2015). P63RhoGEF regulates auto- and paracrine signaling in cardiac fibroblasts. *Journal of Molecular and Cellular Cardiology*, *88*, 39–54. https://doi.org/10.1016/j.yjmcc.2015.09.009

Oslowski, C. M., & Urano, F. (2011). Measuring ER stress and the unfolded protein response using mammalian tissue culture system. In P. M. Conn (Ed.), *Methods in Enzymology* (Vol. 490, pp. 71–92). Academic Press. https://doi.org/10.1016/B978-0-12-385114-7.00004-0

Otero, J. H., Lizák, B., & Hendershot, L. M. (2010). Life and death of a BiP substrate. *Seminars in Cell & Developmental Biology*, *21*(5), 472–478. https://doi.org/10.1016/j.semcdb.2009.12.008

Panganiban, R. A., Park, H.-R., Sun, M., Shumyatcher, M., Himes, B. E., & Lu, Q. (2019). Genome-wide CRISPR screen identifies suppressors of endoplasmic reticulum stress-induced apoptosis. *Proceedings of the National Academy of Sciences*, *116*(27), 13384–13393. https://doi.org/10.1073/pnas.1906275116

Parker, M. W., Rossi, D., Peterson, M., Smith, K., Sikström, K., White, E. S., Connett, J. E., Henke, C. A., Larsson, O., & Bitterman, P. B. (2014). Fibrotic extracellular matrix activates a profibrotic positive feedback loop. *Journal of Clinical Investigation*, *124*(4), 1622–1635. https://doi.org/10.1172/JCI71386

Pearse, B. R., & Hebert, D. N. (2010). Lectin chaperones help direct the maturation of glycoproteins in the endoplasmic reticulum. *Biochimica et Biophysica Acta*, *1803*(6), 684–693. https://doi.org/doi.org/10.1016/j.bbamcr.2009.10.008

Perera, M. M., Fischesser, D. M., Molkentin, J. D., & Ayres, N. (2019). Stiffness of thermoresponsive gelatin-based dynamic hydrogels affects fibroblast activation. *Polymer Chemistry*, *10*(46), 6360–6367. https://doi.org/10.1039/C9PY01424A

Petrov, V. V., Fagard, R. H., & Lijnen, P. J. (2000). Transforming growth factor-β1 induces angiotensin-converting enzyme synthesis in rat cardiac fibroblasts during their differentiation to myofibroblasts. *Journal of the Renin-Angiotensin-Aldosterone System*, *1*(4), 342–352. https://doi.org/10.3317/jraas.2000.064

Porter, K. E., & Turner, N. A. (2009). Cardiac fibroblasts: At the heart of myocardial remodeling. *Pharmacology & Therapeutics*, *123*(2), 255–278. https://doi.org/10.1016/j.pharmthera.2009.05.002

Prostko, C. R., Brostrom, M. A., & Brostrom, C. O. (1993). Reversible phosphorylation of eukaryotic initiation factor 2 alpha in response to endoplasmic reticular signaling. *Molecular and Cellular Biochemistry*, *127–128*, 255–265. https://doi.org/10.1007/BF01076776

Rao, M., Wang, X., Guo, G., Wang, L., Chen, S., Yin, P., Chen, K., Chen, L., Zhang, Z., Chen, X., Hu, X., Hu, S., & Song, J. (2021). Resolving the intertwining of inflammation and fibrosis in human heart failure at single-cell level. *Basic Research in Cardiology*, *116*(55), 1–19. https://doi.org/10.1007/s00395-021-00897-1

Rao, R., Ellerby, H., & Bredesen, D. (2004). Coupling endoplasmic reticulum stress to the cell death program. *Cell Death and Differentiation*, *11*(4), 372–380. https://doi.org/doi.org/10.1038/sj.cdd.4401378

Ren, Z., Yu, P., Li, D., Li, Z., Liao, Y., Wang, Y., Zhou, B., & Wang, L. (2020). Single-cell reconstruction of progression trajectory reveals intervention principles in pathological cardiac hypertrophy. *Circulation*, *141*(21), 1704–1719. https://doi.org/10.1161/CIRCULATIONAHA.119.043053

Rojas-Rivera, D., Delvaeye, T., Roelandt, R., Nerinckx, W., Augustyns, K., Vandenabeele, P., & Bertrand, M. J. M. (2017). When PERK inhibitors turn out to be new potent RIPK1 inhibitors: Critical issues on the specificity and use of GSK2606414 and GSK2656157. *Cell Death & Differentiation*, *24*(6), 1100–1110. https://doi.org/10.1038/cdd.2017.58

Römisch, K. (2005). Endoplasmic reticulum-associated degradation. *Annual Review of Cell and Developmental Biology*, *21*, 435–456. https://doi.org/doi.org/10.1146/annurev.cellbio.21.012704.133250

Ron, D. (2002). Translational control in the endoplasmic reticulum stress response. *Journal of Clinical Investigation*, *110*(10), 1383–1388. https://doi.org/10.1172/JCI0216784

Rong, J., Pass, I., Diaz, P. W., Ngo, T. A., Sauer, M., Magnuson, G., Zeng, F.-Y., Hassig, C. A., Jackson, M. R., Cosford, N. D. P., Matsuzawa, S., & Reed, J. C. (2015). Cell-based high-throughput luciferase reporter gene assays for identifying and profiling chemical modulators of endoplasmic reticulum signaling protein, IRE1. *SLAS Discovery*, *20*(10), 1232–1245. https://doi.org/10.1177/1087057115600414

Rozpędek-Kamińska, W., Siwecka, N., Wawrzynkiewicz, A., Wojtczak, R., Pytel, D., Diehl, J. A., & Majsterek, I. (2020). The PERK-dependent molecular mechanisms as a novel therapeutic target for neurodegenerative diseases. *International Journal of Molecular Sciences*, *21*(6), 2108. https://doi.org/10.3390/ijms21062108

Ruoslahti, E., & Yamaguchi, Y. (1991). Proteoglycans as modulators of growth factor activities. *Cell*, *64*(5), 867–869. https://doi.org/10.1016/0092-8674(91)90308-L

Sandbo, N., Lau, A., Kach, J., Ngam, C., Yau, D., & Dulin, N. O. (2011). Delayed stress fiber formation mediates pulmonary myofibroblast differentiation in response to TGF-β. *American Journal of Physiology. Lung Cellular and Molecular Physiology*, *301*(6), L656–L666. https://doi.org/doi.org/10.1152/ajplung.00166.2011

Santos, G. L. (2021). *Mechanical regulation of cardiac fibroblasts.* [Georg-August-University Göttingen]. https://doi.org/10.53846/goediss-8721

Santos, G. L., DeGrave, A. N., Rehman, A., Al Disi, S., Xhaxho, K., Schröder, H., Bao, G., Meyer, T., Tiburcy, M., Dworatzek, E., Zimmermann, W.-H., & Lutz, S. (2022). Using different geometries to modulate the cardiac fibroblast phenotype and the biomechanical properties of engineered connective tissues. *Biomaterials Advances*, *139*, 213041. https://doi.org/10.1016/j.bioadv.2022.213041

Santos, G. L., Hartmann, S., Zimmermann, W.-H., Ridley, A., & Lutz, S. (2019). Inhibition of Rho-associated kinases suppresses cardiac myofibroblast function in engineered connective and heart muscle tissues. *Journal of Molecular and Cellular Cardiology*, *134*, 13–28. https://doi.org/10.1016/j.yjmcc.2019.06.015

Satoh, S., Ueda, Y., Koyanagi, M., Kadokami, T., Sugano, M., Yoshikawa, Y., & Makino, N. (2003). Chronic inhibition of Rho kinase blunts the process of left ventricular hypertrophy leading to cardiac contractile dysfunction in hypertension-induced heart failure. *Journal of Molecular and Cellular Cardiology*, *35*(1), 59–70. https://doi.org/10.1016/S0022-2828(02)00278-X

Schellings, M. W. M., Vanhoutte, D., Swinnen, M., Cleutjens, J. P., Debets, J., van Leeuwen, R. E. W., d'Hooge, J., Van de Werf, F., Carmeliet, P., Pinto, Y. M., Sage, E. H., & Heymans, S. (2009). Absence of SPARC results in increased cardiac rupture and dysfunction after acute myocardial infarction. *Journal of Experimental Medicine*, *206*(1), 113–123. https://doi.org/10.1084/jem.20081244

Schröder, M., & Kaufman, R. J. (2005). The mammalian unfolded protein response. *Annual Review of Biochemistry*, *74*(1), 739–789. https://doi.org/10.1146/annurev.biochem.73.011303.074134

Senft, D., & Ronai, Z. A. (2015). UPR, autophagy, and mitochondria crosstalk underlies the ER stress response. *Trends in Biochemical Sciences*, *40*(3), 141–148. https://doi.org/10.1016/j.tibs.2015.01.002

Shamu, C. E., & Walter, P. (1996). Oligomerization and phosphorylation of the IRE1p kinase during intracellular signaling from the endoplasmic reticulum to the nucleus. *The EMBO Journal*, *15*(12), 3028–3039. https://doi.org/10.1002/j.1460-2075.1996.tb00666.x

Shang, M., Hu, Y., Cao, H., Lin, Q., Yi, N., Zhang, J., Gu, Y., Yang, Y., He, S., Lu, M., Peng, L., & Li, L. (2022). Concordant and heterogeneity of single-cell transcriptome in cardiac development of human and mouse. *Frontiers in Genetics*, *13*, 892766. https://doi.org/10.3389/fgene.2022.892766

Shi, M., Zhu, J., Wang, R., Chen, X., Mi, L., Walz, T., & Springer, T. A. (2011). Latent TGF-β structure and activation. *Nature*, *474*(7351), 343–349. https://doi.org/10.1038/nature10152

Shi, Y., Vattem, K. M., Sood, R., An, J., Liang, J., Stramm, L., & Wek, R. C. (1998). Identification and characterization of pancreatic eukaryotic initiation factor 2 alpha-subunit kinase, PEK, involved in translational control. *Molecular and Cellular Biology*, *18*(12), 7499–7509. https://doi.org/10.1128/MCB.18.12.7499

Shimazaki, M., Nakamura, K., Kii, I., Kashima, T., Amizuka, N., Li, M., Saito, M., Fukuda, K., Nishiyama, T., Kitajima, S., Saga, Y., Fukayama, M., Sata, M., & Kudo, A. (2008). Periostin is essential for cardiac healing after acute myocardial infarction. *Journal of Experimental Medicine*, *205*(2), 295–303. https://doi.org/10.1084/jem.20071297

Shimizu, Y., Dobashi, K., Iizuka, K., Horie, T., Suzuki, K., Tukagoshi, H., Nakazawa, T., Nakazato, Y., & Mori, M. (2001). Contribution of small GTPase Rho and its target protein ROCK in a murine model of lung fibrosis. *American Journal of Respiratory and Critical Care Medicine*, *163*(1), 210–217. https://doi.org/10.1164/ajrccm.163.1.2001089

Shinde, A. V., Humeres, C., & Frangogiannis, N. G. (2017). The role of α-smooth muscle actin in fibroblast-mediated matrix contraction and remodeling. *Biochimica et Biophysica Acta (BBA) - Molecular Basis of Disease*, *1863*(1), 298–309. https://doi.org/10.1016/j.bbadis.2016.11.006

Shu, S., Zhu, J., Liu, Z., Tang, C., Cai, J., & Dong, Z. (2018). Endoplasmic reticulum stress is activated in post-ischemic kidneys to promote chronic kidney disease. *EBioMedicine*, *37*, 269–280. https://doi.org/10.1016/j.ebiom.2018.10.006

Sidrauski, C., & Walter, P. (1997). The transmembrane kinase IRE1p is a site-specific endonuclease that initiates mRNA splicing in the unfolded protein response. *Cell*, *90*(6), 1031–1039. https://doi.org/10.1016/S0092-8674(00)80369-4

Solé-Boldo, L., Raddatz, G., Schütz, S., Mallm, J.-P., Rippe, K., Lonsdorf, A. S., Rodríguez-Paredes, M., & Lyko, F. (2020). Single-cell transcriptomes of the human skin reveal age-related loss of fibroblast priming. *Communications Biology*, *3*(1), 188. https://doi.org/10.1038/s42003-020-0922-4

Souders, C. A., Bowers, S. L. K., & Baudino, T. A. (2009). Cardiac fibroblast: The renaissance cell. *Circulation Research*, *105*(12), 1164–1176. https://doi.org/10.1161/CIRCRESAHA.109.209809

Spinale, F. G. (2007). Myocardial matrix remodeling and the matrix metalloproteinases: Influence on cardiac form and function. *Physiological Reviews*, *87*(4), 1285–1342. https://doi.org/10.1152/physrev.00012.2007

Spitler, K. M., & Webb, R. C. (2014). Endoplasmic reticulum stress contributes to aortic stiffening via proapoptotic and fibrotic signaling mechanisms. *Hypertension*, *63*(3), e40–e45. https://doi.org/10.1161/HYPERTENSIONAHA.113.02558

Stauffer, W. T., Blackwood, E. A., Azizi, K., Kaufman, R. J., & Glembotski, C. C. (2020). The ER unfolded protein response effector, ATF6, reduces cardiac fibrosis and decreases activation of cardiac fibroblasts. *International Journal of Molecular Sciences*, *21*(4). https://doi.org/10.3390/ijms21041373

Stefan, C. J., Manford, A. G., Baird, D., Yamada-Hanff, J., Mao, Y., & Emr, S. D. (2011). Osh proteins regulate phosphoinositide metabolism at ER-plasma membrane contact sites. *Cell*, *144*(3), 389–401. https://doi.org/10.1016/j.cell.2010.12.034

Sun, S., Shi, G., Sha, H., Ji, Y., Han, X., Shu, X., Ma, H., Inoue, T., Gao, B., Kim, H., Bu, P., Guber, R. D., Shen, X., Lee, A.-H., Iwawaki, T., Paton, A. W., Paton, J. C., Fang, D., Tsai, B., … Qi, L. (2015). IRE1α is an endogenous substrate of endoplasmic-reticulum-associated degradation. *Nature Cell Biology*, *17*(12), 1546–1555. https://doi.org/10.1038/ncb3266

Takeshita, S., Kikuno, R., Tezuka, K., & Amann, E. (1993). Osteoblast-specific factor 2: Cloning of a putative bone adhesion protein with homology with the insect protein fasciclin I. *Biochemical Journal*, *294*(1), 271–278. https://doi.org/10.1042/bj2940271

Tejo-Otero, A., Fenollosa-Artés, F., Achaerandio, I., Rey-Vinolas, S., Buj-Corral, I., Mateos-Timoneda, M. Á., & Engel, E. (2022). Soft-tissue-mimicking using hydrogels for the development of phantoms. *Gels*, *8*(1), 40. https://doi.org/10.3390/gels8010040

Theocharis, A. D., Skandalis, S. S., Gialeli, C., & Karamanos, N. K. (2016). Extracellular matrix structure. *Advanced Drug Delivery Reviews*, *97*, 4–27. https://doi.org/10.1016/j.addr.2015.11.001

Tingstrom, A., Heldin, C.-H., & Rubin, K. (1992). Regulation of fibroblast-mediated collagen gel contraction by platelet-derived growth factor, interleukin-1 alpha and transforming growth factor-beta 1. *Journal of Cell Science*, *102*(2), 315–322. https://doi.org/10.1242/jcs.102.2.315

Tomasek, J. J., Gabbiani, G., Hinz, B., Chaponnier, C., & Brown, R. A. (2002). Myofibroblasts and mechano-regulation of connective tissue remodelling. *Nature Reviews Molecular Cell Biology*, *3*(5), 349–363. https://doi.org/10.1038/nrm809

Tomasek, J. J., & Hay, E. D. (1984). Analysis of the role of microfilaments and microtubules in acquisition of bipolarity and elongation of fibroblasts in hydrated collagen gels. *Journal of Cell Biology*, *99*(2), 536–549. https://doi.org/10.1083/jcb.99.2.536

Travers, J. G., Kamal, F. A., Robbins, J., Yutzey, K. E., & Blaxall, B. C. (2016). Cardiac fibrosis: The fibroblast awakens. *Circulation Research*, *118*(6), 1021–1040. https://doi.org/10.1161/CIRCRESAHA.115.306565

Trombetta, E. S., & Parodi, A. J. (2003). Quality control and protein folding in the secretory pathway. *Annual Review of Cell and Developmental Biology*, *19*, 649–676. https://doi.org/10.1146/annurev.cellbio.19.110701.153949

Tsai, J., & Douglas, M. G. (1996). A conserved HPD sequence of the J-domain is necessary for YDJ1 stimulation of Hsp70 ATPase activity at a site distinct from substrate binding. *Journal of Biological Chemistry*, *271*(16), 9347–9354. https://doi.org/10.1074/jbc.271.16.9347

Tucker, N. R., Chaffin, M., Fleming, S. J., Hall, A. W., Parsons, V. A., Bedi, K. C., Akkad, A.-D., Herndon, C. N., Arduini, A., Papangeli, I., Roselli, C., Aguet, F., Choi, S. H., Ardlie, K. G., Babadi, M., Margulies, K. B., Stegmann, C. M., & Ellinor, P. T. (2020). Transcriptional and cellular diversity of the human heart. *Circulation*, *142*(5), 466–482. https://doi.org/10.1161/CIRCULATIONAHA.119.045401

Turishcheva, E., Vildanova, M., Onishchenko, G., & Smirnova, E. (2022). The role of endoplasmic reticulum stress in differentiation of cells of mesenchymal origin. *Biochemistry (Moscow)*, *87*(9), 916–931. https://doi.org/10.1134/S000629792209005X

van Vliet, A. R., Giordano, F., Gerlo, S., Segura, I., Van Eygen, S., Molenberghs, G., Rocha, S., Houcine, A., Derua, R., Verfaillie, T., Vangindertael, J., De Keersmaecker, H., Waelkens, E., Tavernier, J., Hofkens, J., Annaert, W., Carmeliet, P., Samali, A., Mizuno, H., & Agostinis, P. (2017). The ER stress sensor PERK coordinates ER-plasma membrane contact site formation through interaction with filamin-A and F-actin remodeling. *Molecular Cell*, *65*(5), 885-899.e6. https://doi.org/10.1016/j.molcel.2017.01.020

Vaughan, M. B., Xu, G., Morris, T. L., Kshetri, P., & Herwig, J. X. (2019). Predictable fibroblast tension generation by measuring compaction of anchored collagen matrices using microscopy and optical coherence tomography. *Cell Adhesion & Migration*, *13*(1), 302–313. https://doi.org/10.1080/19336918.2019.1644855

Vikhorev, P., & Vikhoreva, N. (2018). Cardiomyopathies and related changes in contractility of human heart muscle. *International Journal of Molecular Sciences*, *19*(8), 2234. https://doi.org/10.3390/ijms19082234

Wada, I., Rindress, D., Cameron, P. H., Ou, W. J., Doherty, J. J., Louvard, D., Bell, A. W., Dignard, D., Thomas, D. Y., & Bergeron, J. J. (1991). SSR alpha and associated calnexin are major calcium binding proteins of the endoplasmic reticulum membrane. *Journal of Biological Chemistry*, *266*(29), 19599–19610. https://doi.org/10.1016/S0021-9258(18)55036-5

Wakatsuki, T., & Elson, E. L. (2002). Reciprocal interactions between cells and extracellular matrix during remodeling of tissue constructs. *Biophysical Chemistry*, *100*(1–3), 593–605. https://doi.org/10.1016/S0301-4622(02)00308-3

Wakatsuki, T., Kolodney, M. S., Zahalak, G. I., & Elson, E. L. (2000). Cell mechanics studied by a reconstituted model tissue. *Biophysical Journal*, *79*(5), 2353–2368. https://doi.org/10.1016/S0006-3495(00)76481-2

Wallis, A. K., & Freedman, R. B. (2011). Assisting oxidative protein folding: How do protein disulphide-isomerases couple conformational and chemical processes in protein folding? In S. Jackson (Ed.), *Molecular Chaperones* (Vol. 328, pp. 1–34). Springer. https://doi.org/10.1007/128_2011_171

Wang, D.-Z., Chang, P. S., Wang, Z., Sutherland, L., Richardson, J. A., Small, E., Krieg, P. A., & Olson, E. N. (2001). Activation of cardiac gene expression by myocardin, a transcriptional cofactor for serum response factor. *Cell*, *105*(7), 851–862. https://doi.org/10.1016/S0092-8674(01)00404-4

Weber, K. T. (1989). Cardiac interstitium in health and disease: The fibrillar collagen network. *Journal of the American College of Cardiology*, *13*(7), 1637–1652. https://doi.org/10.1016/0735-1097(89)90360-4

Whittaker, P., Boughner, D. R., & Kloner, R. A. (1989). Analysis of healing after myocardial infarction using polarized light microscopy. *American Journal of Pathology*, *134*(4), 879–893.

Wille, J. J., Elson, E. L., & Okamoto, R. J. (2006). Cellular and matrix mechanics of bioartificial tissues during continuous cyclic stretch. *Annals of Biomedical Engineering*, *34*(11), 1678–1690. https://doi.org/10.1007/s10439-006-9153-1

Woodiwiss, A. J., Tsotetsi, O. J., Sprott, S., Lancaster, E. J., Mela, T., Chung, E. S., Meyer, T. E., & Norton, G. R. (2001). Reduction in myocardial collagen cross-linking parallels left ventricular dilatation in rat models of systolic chamber dysfunction. *Circulation*, *103*(1), 155–160. https://doi.org/10.1161/01.CIR.103.1.155

World Health Organization. (2021, June 11). *Cardiovascular diseases*. Cardiovascular Diseases. https://www.who.int/en/news-room/fact-sheets/detail/cardiovascular-diseases-(cvds)

Xia, Y., Dobaczewski, M., Gonzalez-Quesada, C., Chen, W., Biernacka, A., Li, N., Lee, D.-W., & Frangogiannis, N. G. (2011). Endogenous thrombospondin 1 protects the pressure-overloaded myocardium by modulating fibroblast phenotype and matrix metabolism. *Hypertension*, *58*(5), 902–911. https://doi.org/10.1161/HYPERTENSIONAHA.111.175323

Xiao, Y., Hill, M. C., Li, L., Deshmukh, V., Martin, T. J., Wang, J., & Martin, J. F. (2019). Hippo pathway deletion in adult resting cardiac fibroblasts initiates a cell state transition with spontaneous and self-sustaining fibrosis. *Genes & Development*, *33*(21–22), 1491–1505. https://doi.org/10.1101/gad.329763.119

Xie, J., Zhang, Q., Zhu, T., Zhang, Y., Liu, B., Xu, J., & Zhao, H. (2014). Substrate stiffness-regulated matrix metalloproteinase output in myocardial cells and cardiac fibroblasts: Implications for myocardial fibrosis. *Acta Biomaterialia*, *10*(6), 2463–2472. https://doi.org/10.1016/j.actbio.2014.01.031

Yan, W., Wang, P., Zhao, C. X., Tang, J., Xiao, X., & Wang, D. W. (2009). Decorin gene delivery inhibits cardiac fibrosis in spontaneously hypertensive rats by modulation of transforming growth factor-beta/SMAD and p38 mitogen-activated protein kinase signaling pathways. *Human Gene Therapy*, *20*(10), 1190–1200. https://doi.org/10.1089/hum.2008.204

Yang, J., Dungrawala, H., Hua, H., Manukyan, A., Abraham, L., Lane, W., Mead, H., Wright, J., & Schneider, B. L. (2011). Cell size and growth rate are major determinants of replicative lifespan. *Cell Cycle*, *10*(1), 144–155. https://doi.org/10.4161/cc.10.1.14455

Yao, Y., Lu, Q., Hu, Z., Yu, Y., Chen, Q., & Wang, Q. K. (2017). A non-canonical pathway regulates ER stress signaling and blocks ER stress-induced apoptosis and heart failure. *Nature Communications*, *8*(1), 133. https://doi.org/10.1038/s41467-017-00171-w

Yeh, Y.-C., Corbin, E. A., Caliari, S. R., Ouyang, L., Vega, S. L., Truitt, R., Han, L., Margulies, K. B., & Burdick, J. A. (2017). Mechanically dynamic PDMS substrates to investigate changing cell environments. *Biomaterials*, *145*, 23–32. https://doi.org/10.1016/j.biomaterials.2017.08.033

Yoshida, H., Matsui, T., Yamamoto, A., Okada, T., & Mori, K. (2001). XBP1 mRNA is induced by ATF6 and spliced by IRE1 in response to ER stress to produce a highly active transcription factor. *Cell*, *107*(7), 881–891. https://doi.org/10.1016/S0092-8674(01)00611-0

Young, J. C. (2010). Mechanisms of the Hsp70 chaperone system. *Biochemistry and Cell Biology*, *88*(2), 291–300. https://doi.org/10.1139/O09-175

Yu, F.-X., Zhao, B., Panupinthu, N., Jewell, J. L., Lian, I., Wang, L. H., Zhao, J., Yuan, H., Tumaneng, K., Li, H., Fu, X.-D., Mills, G. B., & Guan, K.-L. (2012). Regulation of the hippo-YAP pathway by G-protein-coupled receptor signaling. *Cell*, *150*(4), 780–791. https://doi.org/10.1016/j.cell.2012.06.037

Yu, J., Seldin, M. M., Fu, K., Li, S., Lam, L., Wang, P., Wang, Y., Huang, D., Nguyen, T. L., Wei, B., Kulkarni, R. P., Di Carlo, D., Teitell, M., Pellegrini, M., Lusis, A. J., & Deb, A. (2018). Topological arrangement of cardiac fibroblasts regulates cellular plasticity. *Circulation Research*, *123*(1), 73–85. https://doi.org/10.1161/CIRCRESAHA.118.312589

Zhang, G., Wang, X., Gillette, T. G., Deng, Y., & Wang, Z. V. (2019). Unfolded protein response as a therapeutic target in cardiovascular disease. *Current Topics in Medicinal Chemistry*, *19*(21), 1902–1917. https://doi.org/10.2174/1568026619666190521093049

Zhang, H., Liu, C.-Y., Zha, Z.-Y., Zhao, B., Yao, J., Zhao, S., Xiong, Y., Lei, Q.-Y., & Guan, K.-L. (2009). TEAD transcription factors mediate the function of TAZ in cell growth and epithelial-mesenchymal transition. *Journal of Biological Chemistry*, *284*(20), 13355–13362. https://doi.org/10.1074/jbc.M900843200

Zhao, B., Wei, X., Li, W., Udan, R. S., Yang, Q., Kim, J., Xie, J., Ikenoue, T., Yu, J., Li, L., Zheng, P., Ye, K., Chinnaiyan, A., Halder, G., Lai, Z.-C., & Guan, K.-L. (2007). Inactivation of YAP oncoprotein by the Hippo pathway is involved in cell contact inhibition and tissue growth control. *Genes & Development*, *21*(21), 2747–2761. https://doi.org/10.1101/gad.1602907

Zhao, B., Ye, X., Yu, J., Li, L., Li, W., Li, S., Yu, J., Lin, J. D., Wang, C.-Y., Chinnaiyan, A. M., Lai, Z.-C., & Guan, K.-L. (2008). TEAD mediates YAP-dependent gene induction and growth control. *Genes & Development*, *22*(14), 1962–1971. https://doi.org/10.1101/gad.1664408

Zibadi, S., Vazquez, R., Moore, D., Larson, D. F., & Watson, R. R. (2009). Myocardial lysyl oxidase regulation of cardiac remodeling in a murine model of diet-induced metabolic syndrome. *American Journal of Physiology-Heart and Circulatory Physiology*, *297*(3), H976–H982. https://doi.org/10.1152/ajpheart.00398.2009

Zinszner, H., Kuroda, M., Wang, X., Batchvarova, N., Lightfoot, R. T., Remotti, H., Stevens, J. L., & Ron, D. (1998). CHOP is implicated in programmed cell death in response to impaired function of the endoplasmic reticulum. *Genes & Development*, *12*(7), 982–995. https://doi.org/10.1101/gad.12.7.982